Title

Fast Beam Investigations of Two- and Three-Body Photodissociation by Time- and Position-Coincidence Imaging

Author

Crider, Paul

Publication Date

2010

Fast Beam Investigations of Two- and Three-Body Photodissociation by Time- and Position-Coincidence Imaging

by

Paul Edward Crider II

A dissertation submitted in partial satisfaction of the
requirements for the degree of
Doctor of Philosophy

in

Chemistry

in the

GRADUATE DIVISION

of the

UNIVERSITY OF CALIFORNIA, BERKELEY

Committee in charge:
Professor Daniel M. Neumark, Chair
Professor William H. Miller
Professor Robert W. Dibble

Fall 2010

Fast Beam Investigations of Two- and Three-Body Photodissociation by Time- and Position-Coincidence Imaging

by

Paul Edward Crider II

Abstract

Fast Beam Investigations of Two- and Three-Body Photodissociation by Time- and Position-Coincidence Imaging

by

Paul Edward Crider II

Doctor of Philosophy in Chemistry

University of California, Berkeley

Professor Daniel M. Neumark, Chair

Fast beam photofragment translational spectroscopy has been used to elucidate the photodissociation dynamics of small radicals and closed-shell anions. Imaging of photofragments in time- and position-coincidence allows the determination of mass distributions, translational energy distributions [*P(E_T)* distributions], and in the case of three-body fragmentation channels, ternary Dalitz plots depicting the momentum disposal among the fragments. These data yield information about the potential energy surfaces responsible for dissociation as well dynamic and kinematic information about the decay mechanism itself.

Chapter 1 presents a brief overview of photodissociation dynamics and photofragment translational spectroscopy and some recurring themes of the research presented in this Thesis are explored. The use of Dalitz plots in kinematic analysis of three-body dissociation is discussed in detail.

Chapters 2 and 3 present, respectively, experimental and theoretical findings on the photodissociation of perdeuterated C_3D_3 isotopologs, propargyl (D_2CCCD) and propynyl ($CCCD_3$) at 248 and 193 nm. Mass distributions reveal D_2 loss and three heavy mass channels: CD + C_2D_2, CD_2 + C_2D, and CD_3 + C_2. The D loss channel is present, but incompatible with our detection scheme and thus was not observed. *P(E_T)* distributions indicate each dissociation proceeds by internal conversion followed by statistical dissociation on the ground state surface. In Chapter 3, results of high level ab initio calculations are presented and RRKM rate constants are determined.

Chapter 4 presents results on two- and three-body photodissociation dynamics of I_2Br^- from 300 to 270 nm. Two- and three-body dissociation is observed throughout this wavelength range. Four distinct two-body channels are observed: Br^- + I_2, I^- + IBr, Br + I_2^-, and I + IBr^-. Dalitz plots indicate three-body dissociation

occurs primarily by a concerted decay mechanism. A sequential dissociation mechanism, where Br^- + $I_2(B)$ is followed by electronic predissociation of the metastable $I_2(B)$ fragment into ground state I atoms is reported.

Chapter 5 presents preliminary results of two- and three-body photodissociation of ozone at 193 and 157 nm. Ozone is prepared by photodetachment of ozonide at 386 nm (about 1.1 eV above the detachment energy). Greater than expected kinetic energy release is observed for both wavelengths in the $P(E_T)$ distributions. The additional energy is attributed to two sources: extra energy available by photodetaching far above the electron affinity of ozone, and extra internal energy in the ozonide precursor. Three-body dissociation occurs at 193 nm as a 3.6% channel and at 157 nm as a 19.2% channel. Three-body dissociation proceeds at both wavelengths by a synchronous, concerted decay mechanism.

Contents

List of figures

List of tables

Acknowledgments

It should go without saying that the completion of a PhD was something I could not have accomplished on my own. First I would like to thank Dan for the privilege of working in his lab. Despite my grumblings, I value the rigor he imparted on my contributions to the scientific literature. Of course, I should also thank Dan for introducing me to state-of-the-art of excimer laser technology (As the adage goes, "All lasers hate you, but excimers hate themselves."). After all, what doesn't kill me makes me stronger. And I must thank him for his recommendation letter writing skills, which have already borne fruit in the uncertainty-laden twilight of my graduate school experience.

I thank Beth Kautzman and Dave Szpunar for showing me the ropes of the Fast Radical Beam Machine. In addition to her patient explanations, Beth's unfailingly sunny disposition always made it a little easier to trudge my way up the hill to lab in the morning. I probably didn't deserve her unflinching resilience in the face of some of my more offensive mannerisms and quirks (okay sometimes she did flinch).

Luca Castiglioni, in the final analysis, was a beneficial addition to some of the darker days of FRBM. He was a great source of expertise on hydrocarbon radical chemistry, and was indispensible in dealing with rebellious imaging electronics and unhelpful Canadian camera suppliers. He was also a good friend, and a good outlet for my forays into trying to understand European politics. I bequeath FRBM to Aaron Harrison without hesitation as he ushers in the new era of the Roentdek detector. I will continue to envy his ability to get quality work done while remaining preternaturally laid back.

Outside of the lab, I would like to thank the many people who made my life at Berkeley worthwhile, from my fellow boozers and climbing buddies to my dialectical sparring partners and confidantes. And all the cross terms. A list of such people would invariably be incomplete, so I can only hope I have made clear to these individuals in other ways how much I value them.

I would like to thank my parents, who have always believed in me and supported me, even as I leave them geographically ever further behind. And finally I would like to thank Jeanine, who made the last two years not only bearable, but full of adventure. She is the best companion I could imagine, and I look forward to our journey together.

Chapter 1

Introduction

1. 1 Principles of photodissociation

Photodissociation results when the internal energy gained by the absorption of a photon exceeds the binding energy of some bond within the molecule, causing the bond to cleave. Upon bond cleavage, the molecule fragments into composite molecules or atoms and some of the internal energy of the molecule is converted into translational energy, impelling the fragments apart. The study of photodissociation dynamics is important on quite a practical level, as light interacts with molecules in us and around us. For instance, photodissociation of ozone in the stratosphere prevents that light from being harmfully absorbed by the DNA of living creatures.[1]

Over the last few decades, the study of photodissociation has grown in importance with the increasing sophistication of laser technology and the development of molecular beam methods.[2] The earliest photodissociation experiment using a molecular beam came from Wilson and coworkers, who studied the photodissociation of Cl_2 at 347 nm with the first photofragment translational spectrometer.[3,4] The first study of the angular distributions resulting from photodissociation was conducted prior to this by J. Solomon.[5] The theory of photofragment angular distributions was shortly thereafter laid out in detail by R. Zare.[6] Photofragment translational spectroscopy (PTS) was further modernized by Lee and coworkers, who introduced an improved, differentially pumped mass spectrometer detector, among other innovations.[7] Ion imaging[8] paved the way for velocity-map imaging,[9] where each recoil vector is mapped onto a single point on the detector, significantly improving the resolution of PTS to the level of vibrational state specificity.

The state of the art of PTS and photofragment imaging methods have been reviewed elsewhere.[10-12] A more general review of photodissociation dynamics is given by Butler and Neumark,[13] and includes discussions of laser-induced fluorescence (LIF),[14-16] resonance-enhanced multiphoton ionization (REMPI),[17] and other valuable techniques that are not necessarily coupled with molecular beam methods. An indispensible presentation of the theory of photodissociation dynamics has been written by R. Schinke.[18]

Photodissociation dynamics serves as a tool for understanding chemical reactions. Consider a simple bimolecular reaction of AB + C → ABC → A + BC, where A, B, and C may be either atoms or polyatomic molecules and ABC is a reactive intermediate species. By exciting ABC with a photon of sufficient energy to cleave one of the chemical bonds and detecting one or more of the resulting product fragments, one can quantitatively determine the energy required for either product pathway (AB + C or A + BC) to become accessible. By observing the product energy distribution, one can gain information about the potential energy surfaces relevant for the bimolecular reaction.

In a lab setting, photodissociation usually results from excitation of a molecule from its electronic ground state to a higher-lying electronic state. The fate of the molecule following photoexcitation depends on the shape of the potential energy surface (PES) of the excited state. Figure 1.1 shows cartoon representations of a few PES configurations relevant to the experiments described in this Thesis. The x-axis in Fig. 1.1 is the one-dimensional reaction coordinate along which the bond is cleaved (often a bond length). This is a simplification: for molecules larger than diatomics, the photodissociation dynamics are described by a multidimensional hypersurface of multiple degrees of freedom.

Figure 1.1a illustrates direct dissociation. Here, photoabsorption excites the molecule from its electronic ground state to a repulsive surface. Because there is no time for redistribution of the available energy, excitation to repulsive PESs is often characterized by a large translational energy release into products. As the example of I_2Br^- photodissociation in Chapter 4 shows, extensive vibrational and rotational excitation can nonetheless result from large differences in molecular geometry between the ground state molecule and the photoproducts, as can described by a Franck-Condon model.[19]

Figure 1.1b shows an example of electronic predissociation, where the photon promotes the molecule to a bound electronic excited state, which then couples to a repulsive surface. Similar dynamics are described in Chapter 4, where direct photodissociation of I_2Br^- produces I_2 in an electronic excited state, which subsequently predissociates after longer than at least one rotational period, allowing randomization of orientation.

In Figure 1.1c, absorption of a photon excites the molecule from its electronic ground state to a bound upper electronic state. The molecule subsequently transitions back to the ground electronic state by passing through a conical intersection[20-22] with the available energy from the photon deposited into rotational and vibrational quanta. This internal conversion (IC) to the electronic ground state is followed by a statistical redistribution of available energy into various modes until enough energy is deposited into the reaction coordinate for the bond to break. Because of the statistical redistribution of energy among multiple modes, little energy is deposited into translation.

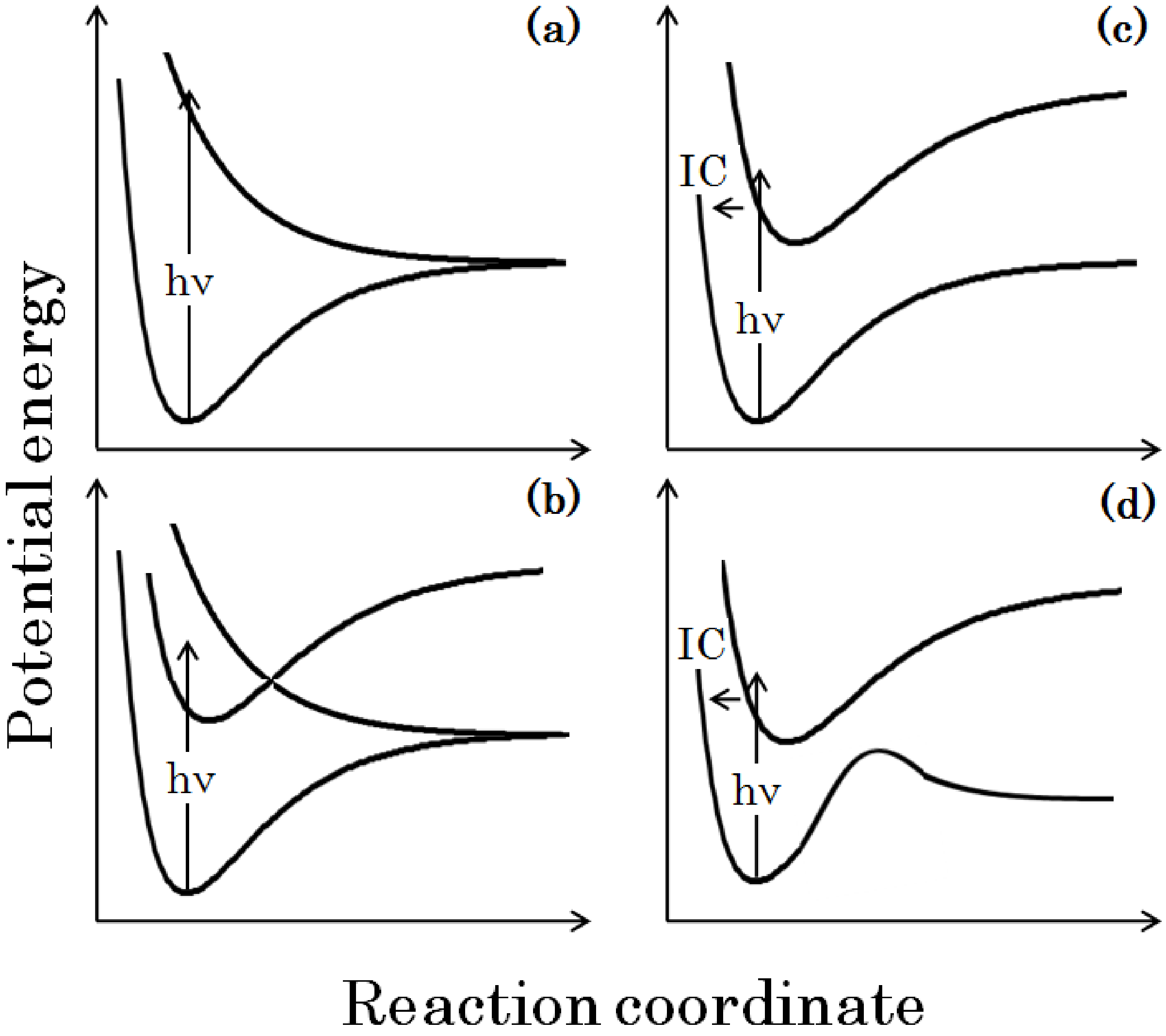

Figure 1.1 Four canonical dissociation schemes: (a) statistical dissociation on the ground state surface following internal conversion, (b) statistical dissociation on the ground state surface over a barrier following internal conversion, (c) direct excitation to a repulsive surface, and (d) electronic predissociation via coupling to a repulsive surface following excitation to a bound state.

Figure 1.1d presents a similar scenario, the difference being the presence of a barrier to dissociation along the reaction coordinate. The repulsive shape of the PES to the right of the barrier tends to result in a shift to higher translational energy release compared to the barrierless case. Photodissociation via PESs similar to Figs. 1.1a and b are explored in Chapters 2 and 3, as well the related published studies.[23,24]

In each case, the exciting photon prepares the molecule on a new PES which guides the evolution of the dissociating molecule into products and determines the final distribution of electronic, rotational, vibrational, and translational states. Measuring final state distributions then provides insight into the relevant potential energy surfaces of the system. The experimental technique described in this Thesis measures the distribution of translational energies [$P(E_T)$ distribution] imparted to photofragments following photodissociation. The energy balance for this process is given by

$$E_T = h\nu - E_{\mathrm{int}}^{frag} - D_0\,, \tag{1.1}$$

where E_T is the translational energy release, $h\nu$ is the energy of the photon, E_{int}^{frag} is the internal (electronic, rotational, and vibrational) energy of the photofragments, and D_0 is the energy required to break the bond.

1. 2 Fast beam photofragment translational spectroscopy

The experiments described in this Thesis were performed on the Fast Radical Beam Machine (FRBM), despite some experiments performed on closed-shell anions. Detailed descriptions of the FRBM in both its original[25,26] and its most recent[27] incarnations are available elsewhere. A schematic diagram of the instrument is shown in Figure 1.2. In Figure 1.3, we show an energetic diagram of the experiment, relating the photodetachment laser (red) and photodissociation laser (blue) to the relevant electronic surfaces.

In the classic FRBM experiment, a gas mix containing sample molecules is injected into a vacuum chamber (on the order of 10^{-5} Torr) via a pulsed piezoelectric

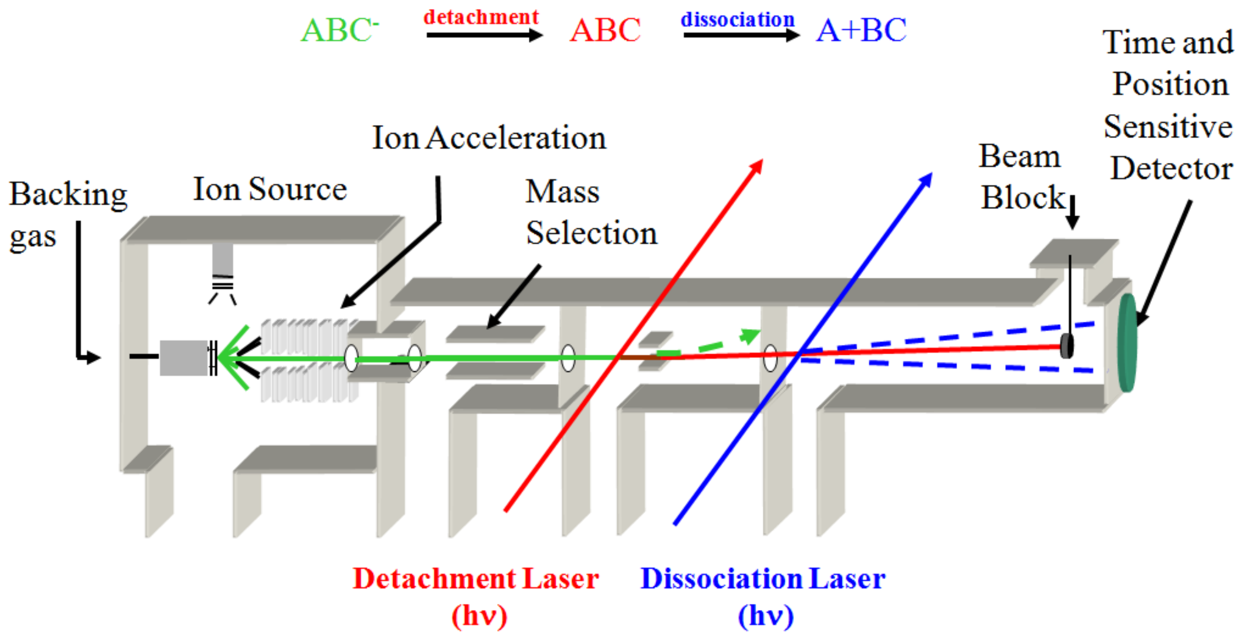

Figure 1.2 The fast beam photofragment translational spectrometer (FRBM).

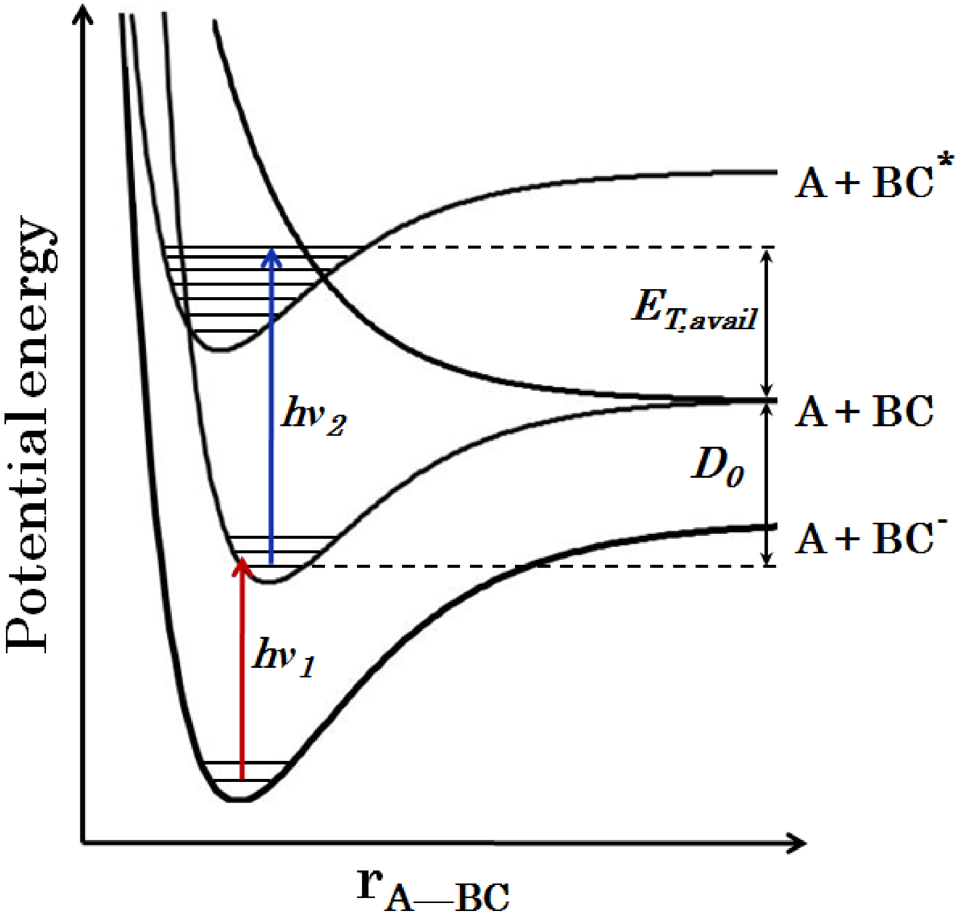

Figure 1.3 Potential energy surfaces involved in a two-photon (photodetachment and photodissociation) FRBM experiment.

valve. The gas pulse undergoes a supersonic expansion, during which the sample molecules are ionized either by a ~1kV discharge,[28] intersection with a ~1kV electron beam, or both. The ions are cooled in this step by collisions with the carrier gas. The resulting anion packet is collimated by a skimmer and accelerated to high laboratory-frame beam energies (5 – 9 keV). The ion packet is then mass-selected by a Bakker time-of-flight mass spectrometer.[29,30] The anion packet is intersected with a pulse from a tunable dye laser ($h\nu_1$) which detaches an electron, resulting in a packet of neutral radicals. The laser is typically tuned to an energy just above the electron affinity (EA) of the neutral in order to prepare it in an internally cold state. Undetached ions are deflected from the beam path by an electric field. The remaining neutral packet is intersected with a pulse from a second laser ($h\nu_2$), effecting photodissociation. Undissociated neutrals collide with a beam block about 4 mm wide. The recoiling photofragments proceed 2.15 m downstream to a time- and position-sensitive coincidence imaging detector based on the design of Zajfman and coworkers.[31]

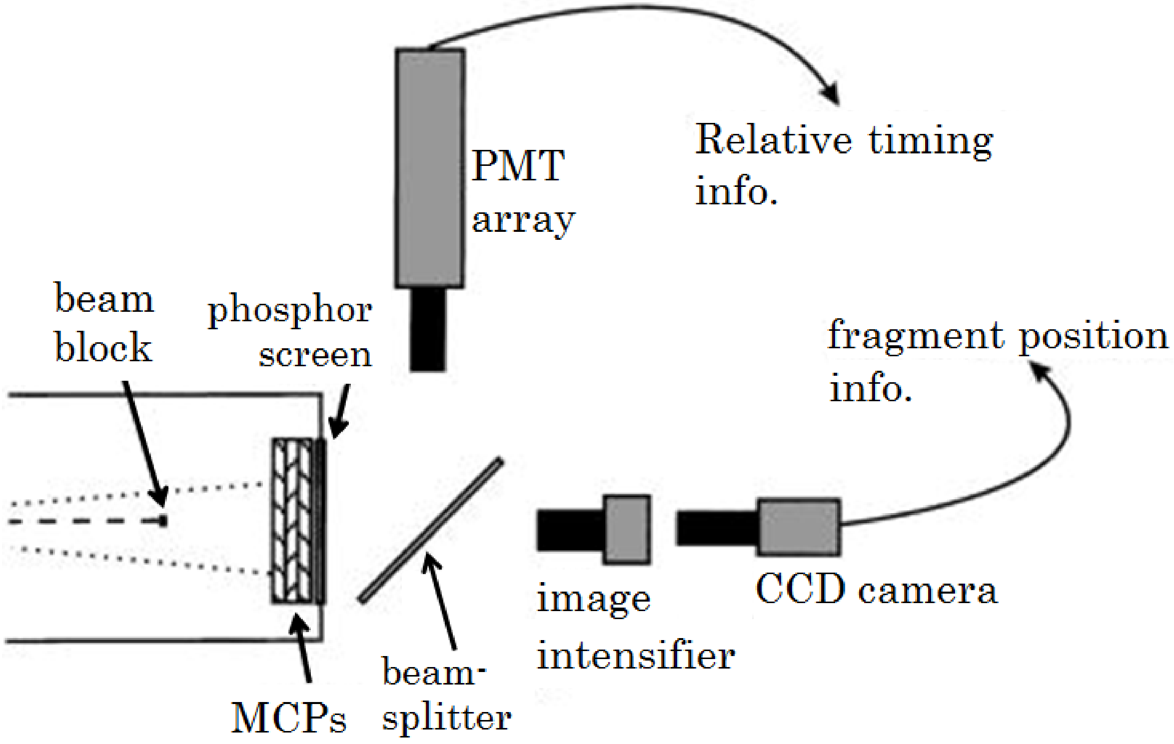

Figure 1.4 The time- and position-coincidence imaging detector set-up.

The detector set-up is shown in Figure 1.4 and consists of three microchannel plates (MCPs) in a Z-stack configuration coupled to a phosphor screen. The image from the phosphor screen is split by a dichroic beam splitter with the reflected image being detected by a 4x4 multianode photomultiplier tube (PMT) array and the transmitted image being detected by a charge-coupled device (CCD) camera by way of an image intensifier. Arrival times measured by the PMT array are correlated with fragment positions obtained by the CCD camera. Coincidence is ensured by accepting only events occurring in the same time window where the rough position data from the PMT array concurs with the accurate position data from the CCD camera. The coincidence arrival times and positions can be used to determine photofragment masses, center-of-mass (COM) translational energy release, and for two-body fragmentation, the angle of recoil for each photodissociation event. This procedure is discussed in detail in the Ph. D. Thesis of Alexandra Hoops.[32]

This detection method is in principle compatible with observing fragmentation into three or more particles, the analysis of which will be discussed in section 1.4. In addition, because the first MCP is held at ground, ions can be detected as well as neutrals. Both of these capabilities were exploited in the photodissociation of I_2Br^- (chapter 4), where three-body dissociation is examined in detail. In this experiment, the photodetachment step was skipped so that mass-selected anions proceeded directly to the photodissociation laser interaction region.

1. 3 Photodetachment by hν > EA: hot dissociation dynamics

As mentioned above, the photodetachment laser is typically tuned to an energy just above the detachment threshold. This has the advantage of preparing the neutral of interest in an internally cool state, thus reducing spectral congestion. In cases where mass-selection is insufficient to isolate the molecule of interest, such as when more than one bound structural isomer is present on the electronic ground state PES, photodetachment serves as a second method of selection, as the isomers will likely have different electron affinities. However, it is sometimes necessary to photodetach ions significantly above the EA, thus producing neutrals with some amount of internal excitation. As discussed in the Ph. D. Thesis of Ryan Bise,[33] the photodetachment laser may be tuned to selectively populate metastable states of the neutral that are inaccessible by standard optical spectroscopy. This is possible because of the different selection rules for photodetachment versus single photon optical excitation. The energy balance for photodissociation following photodetachment by hν > EA is given by

$$E_T = h\nu + E_{\text{int}}^{0} - E_{\text{int}}^{frag} - D_0 , \tag{1.2}$$

where E_{int}^{0} reflects the internal energy of the neutral which was assumed to be zero in Equation 1.1. The metastable neutral prepared in this manner can still be vibrationally and rotationally cool by tuning the laser frequency to just above the term energy of the desired excited state.

Two experiments presented in this Thesis employed above-threshold photodetachment for more practical reasons. The propynyl radical, discussed in chapters 2 and 3, has an EA[34] much higher than that of the lower-lying propargyl isomer,[35-37] so it was possible to distinguish the dissociation dynamics of the two C_3D_3 isomers by photodetaching above and below the propynyl EA, essentially switching the propynyl concentration on and off. The propargyl radical was photodetached well over 1 eV above threshold at both wavelengths, thus preparing the neutral in a distribution of vibrationally excited states, as reflected by the photoelectron spectrum of its corresponding anion.[36] This extra available energy was enough to observe a product channel inaccessible from the vibrational ground state.[23,24]

To study the photodissociation dynamics of ozone (chapter 5), it was necessary to photodetach ozonide more than 1 eV above the detachment threshold because of competition between anionic photodetachment and photodissociation.[38,39] As expected, the $P(E_T)$ distributions show evidence for additional available energy when compared with photodissociation from supersonically cooled ozone generated without a prior photodetachment step,[40] although some evidence from our preliminary results suggests much of the additional available energy comes from the ionization step.

1. 4 Three-body dissociation: Dalitz plot analysis and three-body $P(E_T)$ distributions

Three-body dissociation is often indirectly inferred from greater-than-unity fluorescence measurements[41,42] or forward convolution fitting of time-of-flight data.[40] This inference by itself yields little insight into the kinematics of three-body dissociation. By contrast, photofragment coincidence imaging as employed by FRBM provides a way to investigate three-body dissociation by directly detecting each photofragment. Dalitz plot analysis, especially in conjunction with $P(E_T)$ distributions, provides kinematic detail for this important class of reactions.

Dalitz plots were originally devised in 1953 to describe the decay of a τ-meson into three π-mesons.[43] Helpful discussions of the principles underlying Dalitz plots related to chemistry can be found in the works of Maul and Gericke[44] and Babikov *et al.*[45] In a ternary Dalitz plot, each event where three fragments are detected is plotted within three axes corresponding to the fractional square (f_i) of the vector momentum ($\vec{p}_i$) of each fragment i, given by equation 1.5:

$$f_i = \frac{\left|\vec{p}_i\right|^2}{\sum_i \left|\vec{p}_i\right|^2} \qquad (1.5)$$

Plotted in this way, each event is constrained by conservation of energy and linear momentum to fall within both the triangle formed by the axes as well as the circle inscribed within the triangle. In nonrelativistic systems, this is true for arbitrary fragment masses.[46]

Examples of Dalitz plots are presented in Figure 1.5. Fig. 1.5a illustrates that each event corresponds to a unique dissociation geometry, as represented by the momentum vector diagrams drawn within the circle. For example, the central point in the Dalitz plot always corresponds to symmetric dissociation events with $\left|\vec{p}_1\right| = \left|\vec{p}_2\right| = \left|\vec{p}_3\right|$. Events along the perimeter of the Dalitz circle correspond to linear dissociation events.

Fig. 1.5b shows the special case of equal fragment masses, $m_1 = m_2 = m_3$. Momentum partitioning exhibits six-fold symmetry in this situation, so events are equally likely to appear within any of six equal wedges of the Dalitz circle. The signal-to-noise ratio can be enhanced by ordering the momenta so that all events are assigned to one wedge. In Fig. 1.5b, for example, $f_3 > f_2 > f_1$. Points **A**, **B**, and **C** represent limiting cases. As already noted, point **A** corresponds to totally symmetric momenta, with the momentum vectors pointing to the vertices of an equilateral triangle. Points **B** and **C** correspond to collinear, symmetric and asymmetric

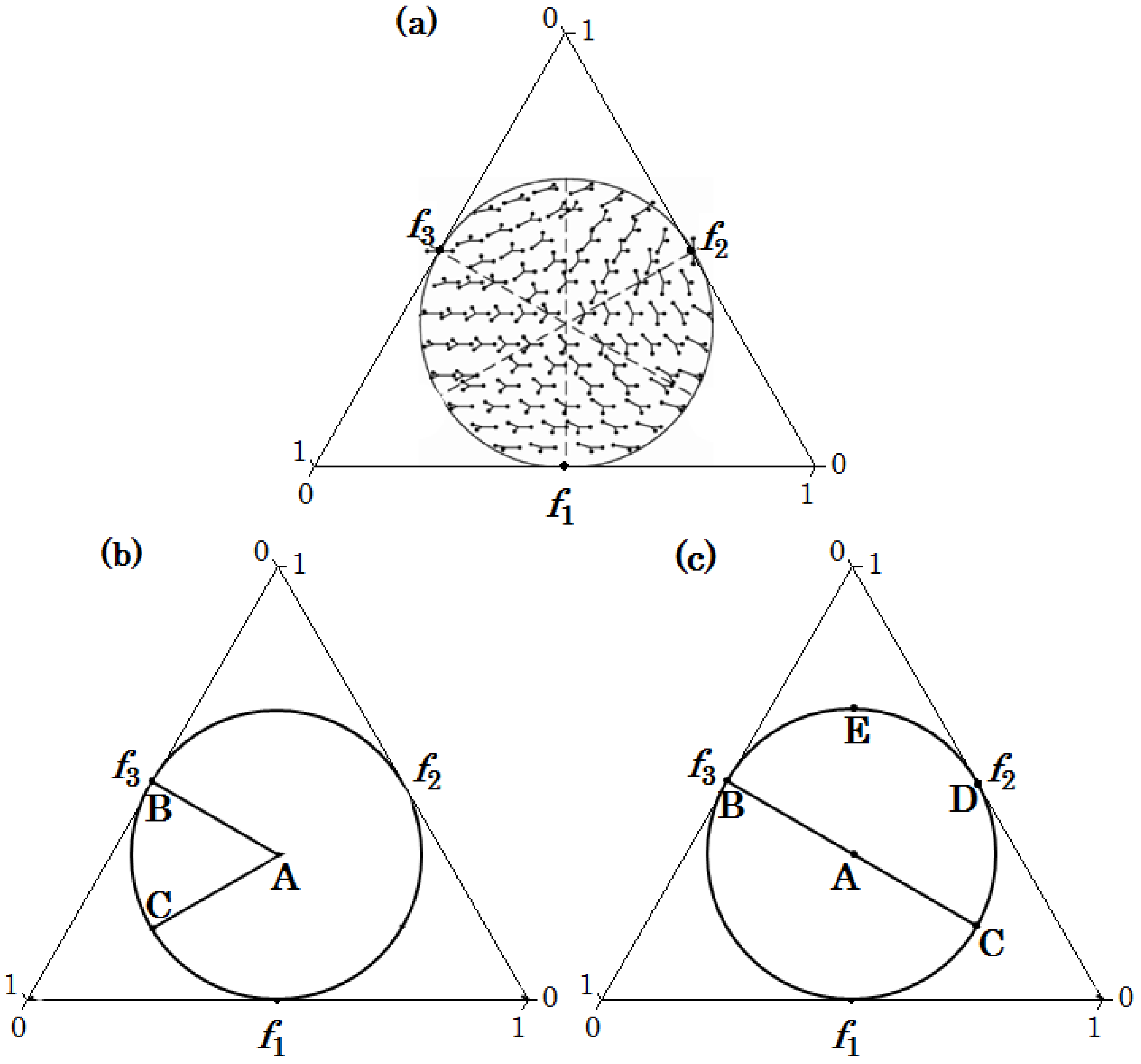

Figure 1.5 Dalitz plot outlines. (a) Shows momentum vector plots corresponding to location within the Dalitz plot. (b) An outline of the Dalitz plot for three equal mass fragments. (c) An outline of the Dalitz plot for two equal mass fragments and one odd mass fragment.

momentum partitioning, respectively. Points along **AB** correspond to symmetric momentum partitioning that is progressively more collinear, moving from **A** to **B**. Points along the **BC** arc are collinear and progressively asymmetric, moving from **B** to **C**. And points along **CA** are asymmetric and progressively less collinear, moving from **C** to **A**. Points within the interior of the circle correspond to momentum vectors defining triangles ranging from scalene (near **C**) to isosceles (near **B**).

Fig. 1.5c presents the two-fold-symmetric case of two equal mass fragments. The possible kinematics are defined by the extremes of points **B**, **C**, and the arc **BC**. Point **B** represents the case where the odd fragment receives zero momentum while point **C** represents the case of a fast odd fragment. Points along the arc correspond to collinear dissociation of various orientations, including **D**, where one of the twin mass fragments receives zero momentum, and **E**, where one of the twins receives the maximum possible momentum.

Dalitz plots are two-dimensional kinematic histograms that can elucidate the mechanism of fragmentation, as well as reveal whether multiple mechanisms are at work. For instance, if significant density of points is apparent in two independent regions of the Dalitz plot, then two dynamic mechanisms are likely responsible. Thus, the Dalitz plot is a powerful complement to $P(E_T)$ distributions obtained by photofragment translational spectroscopy, as features within either representation can be correlated with one another.

An example of this is presented in Figure 1.6, obtained from the photodissociation of I_2Br^- at 4.28 eV, discussed in chapter 4. The full $P(E_T)$ distribution and narrow cut-outs for the high E_T feature and the low E_T feature are shown in Figs. 1.6a-c, while the corresponding Dalitz plots, constructed from the same data, are shown in Figs. 1.6d-f. A detailed discussion is presented in chapter 4; for the nonce, it should be clear that the two spectroscopic features correspond to quite different features in the Dalitz plot, and thus involve distinct dissociation mechanisms. The feature in Fig. 1.6e is of particular interest. In it, f_{Br} is roughly constant while f_I and $f_{I'}$ are randomized, suggesting the momentum of the Br fragment is determined independently of the other two fragments. This is characteristic of a sequential, or step-wise dissociation, where a metastable molecular fragment is produced by the first bond fission and has enough time to rotate before it succumbs to the second bond rupture.

1. 5 Mass ratio analysis and photofragment discrimination

The competition between photodetachment and photodissociation in ozonide mentioned in Section 1.3 had a curious effect in the ozone experiments discussed in Chapter 5. In this experiment, we prepared ozonide in the ion source, photodetached ($h\nu_1$) more than 1 eV over the electron affinity of ozone, and photodissociated ($h\nu_2$) ozone further downstream. Due to competitive ozonide photodissociation, we observed O_2 contaminant in the beam after intersection with $h\nu_1$, produced either by dissociation or dissociative photodetachment of ozonide. Evidence for the presence of O_2 post-detachment came in the form of detecting photofragments with a 1:1 mass ratio. In the current incarnation of the data analysis software,[32] examining this phenomenon required positing a photoproduct mass channel corresponding to two equal mass fragments of 24 amu from the 48 amu O_3 parent mass, an artifactual quirk warranting an explanation for FRBM posterity.

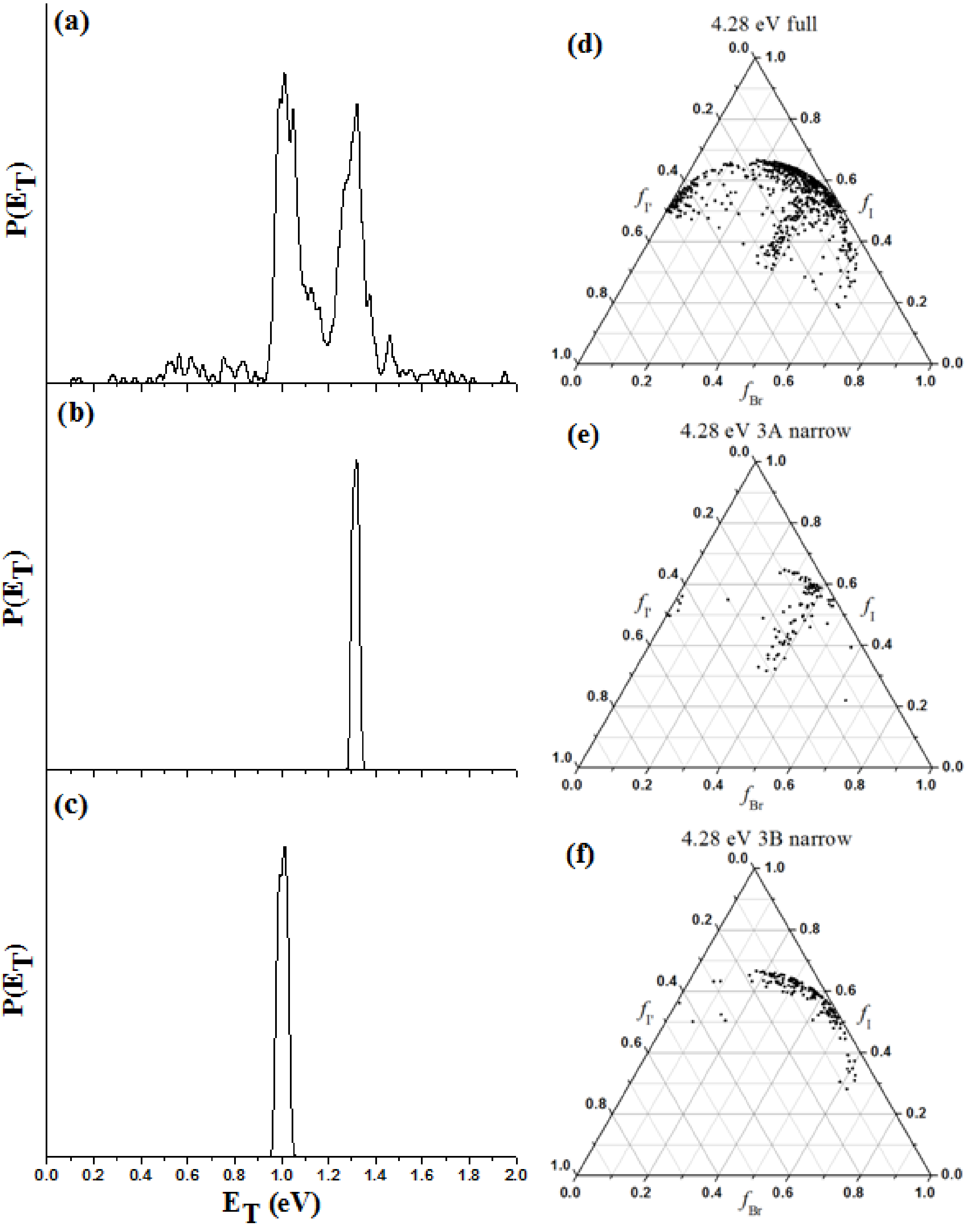

Figure 1.6 Comparison of $P(E_T)$ distributions (panels a-c) and corresponding Dalitz plots (panels d-f). (a) and (d), (b) and (e), and (c) and (f) are the full plots, plots of the fast peak, and plots of the slow peak, respectively.

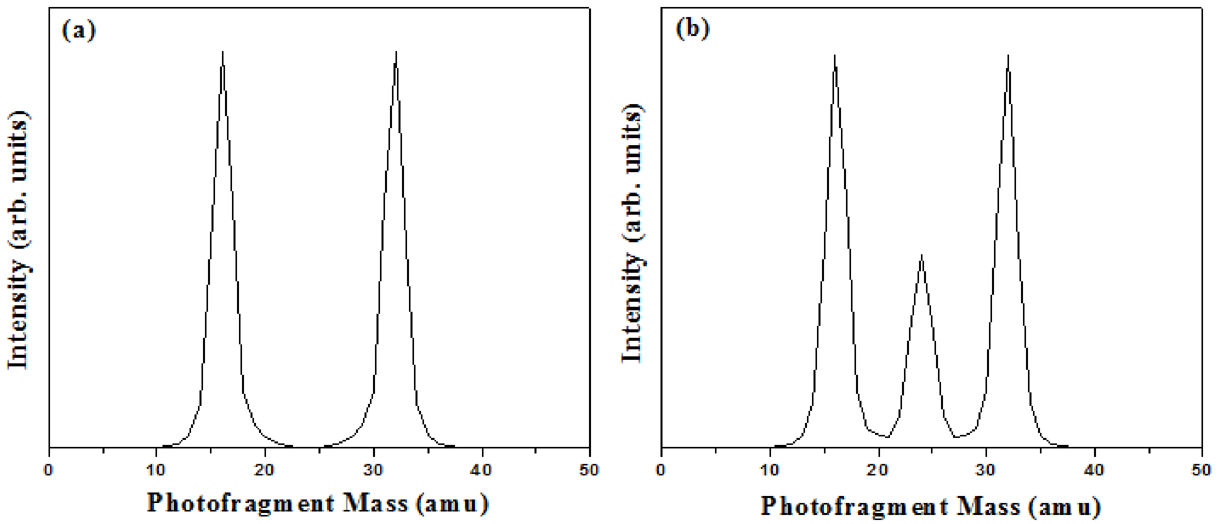

Figure 1.7 Two-body photofragment mass ratios generated from a single ozone dissociation data set. Panel (a) shows the mass distribution with one user input channel of 16 + 32. Panel (b) shows the mass distribution with two user input channels: 16 + 32 and 24 +24.

Photofragment masses are assigned by an iterative algorithm beginning with a user-defined parent mass and user-assumed mass channels. Final assignment depends on fragment mass ratios, rather than absolute masses, which are inferred from the defined parent mass. Thus, dissociation from O_2 contaminant in the ozone beam led to two equal mass fragments of "24 amu" because the O_2 parent was defined to be of mass 48 amu. Figure 1.7 shows two analyses of the same data set acquired from 157 nm photodissociation of ozone. For the mass distribution shown in panel (a), the parent mass was defined as 48 amu (the mass of ozone) and only one two-body mass channel was assumed, leading to 16 amu (O) + 32 amu (O_2) fragments. The mass distribution in panel (b) resulted from assuming a 48 amu parent, the 16 + 32 amu channel, and one additional channel, 24 amu (O) + 24 amu (O). Importantly, the total number of coincidence events accepted increased by the number assigned to the new 24 + 24 amu channel and the number of events assigned to the 16 + 32 amu channel did not appreciably decrease. This implies events in the new channel are real, and not merely reassigned from the first channel.

Similar analysis has been employed previously in our lab in order to understand three-body dissociation events where one fragment receives insufficient recoil to bypass the beam block immediately in front of the center of the MCPs. Hoops *et al.*[47] observed a coincident I + I channel in the photodissociation of linear I_3^-, and Kautzman *et al.*[48] also observed I + I upon dissociative photodetachment of van der Waals-bound $I_2^- \cdot Ar$. Coincident detection of I + Br from dissociation of linear I_2Br^- presented in chapter 4 demonstrates this phenomenon does not require the two detected fragments to have equal mass.

Despite failing to detect one of the fragments, a meaningful $P(E_T)$ distribution can be constructed for three-body events where only two fragments are detected. This is because these events are characterized by the disposal of little or zero kinetic energy into the undetected fragment, so the center-of-mass distribution of total E_T release is mostly unaffected by exclusion of the low E_T fragment's contribution. The $P(E_T)$ distribution does require adjustment for its mass dependence, however. Translational energy release is given by

$$E_T = \tfrac{1}{2}\mu v_{rel}^2 , \tag{1.3}$$

where $\mu = m_1 m_2/(m_1 + m_2)$ is the reduced mass, v_{rel} is the relative velocity of the recoiling fragments, and m_1 and m_2 are the masses of the two fragments. The corrected E_T for three fragments, E_T^3, is a fraction of the E_T computed for two fragments:

$$E_T^3 = \frac{\mu_2}{\mu_3} E_T^2 , \tag{1.4}$$

where E_T^2 is the initial E_T constructed with the two false masses and μ_2 and μ_3 are the reduced masses for the initially assumed and corrected masses, respectively.

The remainder of this Thesis presents specific investigations that have been discussed only generally in this Introduction chapter. In the next chapter, the details and conclusions of UV photodissociation experiments on C_3D_3 radicals is presented. Chapter 3 gives the C_3D_3 system high-level theoretical treatment, elucidating aspects of the photodissociation dynamics that remained unclear from the experiments. Chapter 4 discusses UV photodissociation experiments on the I_2Br^- anion, a model system for asymmetric three-body dissociation. Finally, in chapter 5, preliminary experiments on the 193 and 157 nm photodissociation of ozone are presented, with particular emphasis on the three-body dissociation pathway.

References

[1] N. J. Mason and S. K. Pathak, Contemp. Phys. **38**, 289 (1997).

[2] *Atomic and Molecular Beam Methods*, edited by G. Scoles (Oxford University Press, New York, 1988), Vol. 2.

[3] G. E. Busch, J. F. Cornelius, R. T. Mahoney, R. I. Morse, D. W. Schlosser, and K. R. Wilson, Rev. Sci. Instrum. **41**, (1970).

[4] G. E. Busch, R. T. Mahoney, R. I. Morse, and K. R. Wilson, J. Chem. Phys. **51**, (1969).

[5] J. Solomon, J. Chem. Phys. **47**, (1967).

[6] R. N. Zare, Mol. Photochem. **4**, (1972).

[7] A. Wodtke and Y. T. Lee, *Molecular Photodissociation Dynamics*. (Royal Society of Chemistry, London, 1987).

[8] P. L. Houston, J. Phys. Chem. **100**, 12757 (1996).

[9] A. Eppink and D. H. Parker, Rev. Sci. Instrum. **68**, 3477 (1997).

[10] M. Ashfold, I. Lambert, D. Mordaunt, G. Morley, and C. Western, J. Phys. Chem. **96**, (1992).

[11] M. N. R. Ashfold, N. H. Nahler, A. J. Orr-Ewing, O. P. J. Vieuxmaire, R. L. Toomes, T. N. Kitsopoulos, I. A. Garcia, D. A. Chestakov, S. M. Wu, and D. H. Parker, Phys. Chem. Chem. Phys. **8**, 26 (2006).

[12] R. E. Continetti, Annu. Rev. Phys. Chem. **52**, (2001).

[13] L. J. Butler and D. M. Neumark, J. Phys. Chem. **100**, (1996).

[14] R. J. Cody, M. J. Sabetydzvonik, and W. M. Jackson, J. Chem. Phys. **66**, 2145 (1977).

[15] J. R. McDonald, R. G. Miller, and A. P. Baronavski, Chem. Phys. Lett. **51**, 57 (1977).

[16] M. J. Sabetydzvonik and R. J. Cody, J. Chem. Phys. **66**, 125 (1977).

[17] G. Radhakrishnan, D. Ng, and R. C. Estler, Chem. Phys. Lett. **84**, 260 (1981).

[18] R. Schinke, *Photodissociation Dynamics*. (Cambridge University Press, Cambridge, 1993).

[19] Y. B. Band and K. F. Freed, J. Chem. Phys. **67**, 1462 (1977).

[20] W. Domcke, D. R. Yarkony, and H. Köppel, *Conical Intersections: Electronic Structure, Dynamics and Spectroscopy*. (World Scientific Publishing, 2004).

[21] D. R. Yarkony, Rev. Mod. Phys. **68**, (1996).

[22] D. R. Yarkony, Acc. Chem. Res. **31**, (1998).

[23] L. Castiglioni, S. Vukovic, P. E. Crider, W. A. Lester, and D. M. Neumark, Phys. Chem. Chem. Phys. **12**, 10714 (2010).

[24] P. E. Crider, L. Castiglioni, K. E. Kautzman, and D. M. Neumark, J. Chem. Phys. **130**, (2009).

[25] R. E. Continetti, D. R. Cyr, D. L. Osborn, D. J. Leahy, and D. M. Neumark, J. Chem. Phys. **99**, 2616 (1993).

[26] D. R. Cyr, Ph. D. Dissertation, University of California, Berkeley, 1993.

[27] A. A. Hoops, J. R. Gascooke, A. E. Faulhaber, K. E. Kautzman, and D. M. Neumark, Chem. Phys. Lett. **374**, 235 (2003).

[28] D. L. Osborn, D. J. Leahy, D. R. Cyr, and D. M. Neumark, J. Chem. Phys. **104**, 5026 (1996).

[29] J. M. B. Bakker, J. Phys. E **6**, 785 (1973).

[30] J. M. B. Bakker, J. Phys. E **7**, 364 (1974).

[31] Z. Amitay and D. Zajfman, Rev. Sci. Instrum. **68**, 1387 (1997).

[32] A. A. Hoops, Ph. D. Dissertation, University of California, Berkeley, 2003.

[33] R. T. Bise, Ph. D. Dissertation, University of California, Berkeley, 2000.

[34] J. Zhou, E. Garand, W. Eisfeld, and D. M. Neumark, J. Chem. Phys. **127**, (2007).

[35] J. M. Oakes and G. B. Ellison, J. Am. Chem. Soc. **105**, 2969 (1983).

[36] M. S. Robinson, M. L. Polak, V. M. Bierbaum, C. H. Depuy, and W. C. Lineberger, J. Am. Chem. Soc. **117**, 6766 (1995).

[37] R. K. Sreeruttun, P. Ramasami, G. Yan, C. S. Wannere, P. V. Schleyer, and H. F. Schaefer, Int. J. Mass Spec. **241**, 295 (2005).

[38] J. F. Hiller and M. L. Vestal, J. Chem. Phys. **74**, 6096 (1981).

[39] S. E. Novick, P. C. Engelking, P. L. Jones, J. H. Futrell, and W. C. Lineberger, J. Chem. Phys. **70**, 2652 (1979).

[40] D. Stranges, X. M. Yang, J. D. Chesko, and A. G. Suits, J. Chem. Phys. **102**, 6067 (1995).

[41] M. R. Taherian and T. G. Slanger, J. Chem. Phys. **83**, 6246 (1985).

[42] A. A. Turnipseed, G. L. Vaghjiani, T. Gierczak, J. E. Thompson, and A. R. Ravishankara, J. Chem. Phys. **95**, 3244 (1991).

[43] R. H. Dalitz, Philos. Mag. **44**, 1068 (1953).

[44] C. Maul and K. H. Gericke, J. Phys. Chem. A **104**, 2531 (2000).

[45] D. Babikov, E. A. Gislason, M. Sizun, F. Aguillon, V. Sidis, M. Barat, J. C. Brenot, J. A. Fayeton, and Y. J. Picard, J. Chem. Phys. **116**, 4871 (2002).

[46] L. M. Wiese, O. Yenen, B. Thaden, and D. H. Jaecks, Phys. Rev. Lett. **79**, 4982 (1997).

[47] A. A. Hoops, J. R. Gascooke, A. E. Faulhaber, K. E. Kautzman, and D. M. Neumark, J. Chem. Phys. **120**, 7901 (2004).

[48] K. E. Kautzman, P. E. Crider, D. E. Szpunar, and D. M. Neumark, J. Phys. Chem. A **111**, 12795 (2007).

Chapter 2

Photodissociation of the propargyl and propynyl (C_3D_3) radicals at 248 nm and 193 nm

The contents of this chapter have been published in J. Chem. Phys. **130**, 044310 (2009).

The photodissociation of perdeuterated propargyl (D_2CCCD) and propynyl (D_3CCC) radicals was investigated using fast beam photofragment translational spectroscopy. Radicals were produced from their respective anions by photodetachment at 540 nm and 450 nm (below and above the electron affinity of propynyl). The radicals were then photodissociated by 248 nm or 193 nm light. The recoiling photofragments were detected in coincidence with a time- and position-sensitive detector. Three channels were observed: D_2 loss, $CD + C_2D_2$, and $CD_3 + C_2$. Observation of the D loss channel was incompatible with this experiment and was not attempted. Our translational energy distributions for D_2 loss peaked at nonzero translational energy, consistent with ground state dissociation over small (<1 eV) exit barriers with respect to separated products. Translational energy distributions for the two heavy channels peaked near zero kinetic energy, indicating dissociation on the ground state in the absence of exit barriers.

2. 1 Introduction

C_3H_3 radicals have been of interest for decades owing to their importance in combustion and interstellar chemistry.[1-11] Of the various stable C_3H_3 isomers, propargyl (2-propynyl, H_2CCCH) has received the most attention. This is in part because propargyl lies over 30 kcal/mol below the other C_3H_3 isomers. The propargyl radical is resonance-stabilized, and is thus expected to accumulate in hydrocarbon flames.[12-15] It is now widely thought that the propargyl self-reaction forms the first benzene ring in combustion, as proposed by Wu and Kern.[1] Subsequent reactions with the benzene ring lead to the formation of polycyclic aromatic hydrocarbons (PAHs) and ultimately soot.[1-4,8-10,15,16] Due to its participation in atom-radical and radical-radical reactions without entrance barriers, the propargyl radical is also expected to be important in the chemistry of hydrocarbon-rich planetary atmospheres.[5,11] In this paper, we investigate the photodissociation dynamics of both the propargyl radical and the higher-lying 1-propynyl isomer, H_3CCC, at 248 nm and 193 nm using fast beam photofragment translational spectroscopy.

There have been numerous experimental and theoretical studies of the propargyl radical. Microwave[17] and infrared[18,19] spectroscopy have addressed the structure and vibrational frequencies of its ground electronic state. Its electron affinity (EA)[20-24] and ionization potential (IP)[23,25-28] have been determined. UV absorption studies[29-31] have probed the excited states of the radical, particularly an absorption band around 240 nm, assigned to the $\tilde{B}\,^2B_1 \leftarrow \tilde{X}\,^2B_1$ transition by Fahr *et al.*[30] Theoretical work has focused on the structure and thermochemistry of propargyl[13-15,28,32-34] as well as its role as an intermediate in small hydrocarbon reactions.[15,35-38]

The photodissociation of propargyl was first observed by Jackson *et al.* as secondary photodissociation from the photolysis of allene.[39] Jackson reported three dissociation channels: H loss, H_2 loss, and CH loss, with only minor contribution from the latter two channels. The H loss channel has subsequently been observed in radical photodissociation experiments by Deyerl *et al.*[40] and Goncher *et al.*[41] at 242 nm and 248 nm, respectively. McCunn *et al.*[42] observed this channel from the secondary photodissociation from propargyl chloride at 157 nm. The translational energy distributions obtained from studies suggested that H loss dissociation proceeds through a loose transition state following internal conversion to the ground state. Goncher *et al.*[41] and McCunn *et al.*[42] also observed H_2 loss; their results implied dissociation on the ground electronic state over an exit barrier of around 10 kcal/mol.

High-level calculations performed by Nguyen *et al.*[38] followed by a Rice-Ramsperger-Kassel-Marcus (RRKM) rate-constant analysis[43] identified the same three product channels at 193 nm and 242 nm and yielded branching ratios that agreed well with experimental values, though there was some disagreement as to whether the primary C_3H_2 fragment is cyclic. Eisfeld recently performed calculations[28,34] on the absorption spectrum of propargyl that questioned the assignment of 240 nm absorption to propargyl. Those calculations indicated that the absorption at 240 nm was dipole-forbidden and that the $\tilde{B}^2B_1 \leftarrow \tilde{X}^2B_1$ transition had a maximum around 220 nm, a value too high to be consistent with experiments. However, the recent photodissociation experiments by Goncher *et al.*[41] supported the original assignment of the 240 nm band.

Although it is also expected to be present in combustion, the propynyl radical, calculated to lie 41.9 kcal/mol above propargyl,[15] has been considerably more resistant to experimental characterization. Several experiments involving propynyl have sought to answer whether the primary product of the photodissociation of propyne at 193 nm is propynyl or propargyl. Early experiments in the 1960s[29,44] suggested propargyl was the major photoproduct, but later studies[36,45-47] indicated propynyl. The most recent studies[48-53] confirm the earlier finding that propargyl is the major photoproduct formed by a statistical dissociation on the ground electronic state following internal conversion. One method that has proved effective for studying propynyl is anion photoelectron spectroscopy. This is because the propargyl and propynyl anions are nearly isoenergetic[22] while the radicals have very different electron affinities (0.918 eV and 2.735 eV, respectively[22,23]), making discrimination between the two species possible. The EA of 2.718 eV for propynyl was originally determined by anion photoelectron spectroscopy[21] and recently improved to 2.735 eV by higher resolution slow-electron velocity map imaging.[54] Theoretical approaches have yielded similar values.[22,23]

Theoretical work with propynyl has been primarily concerned with its thermochemistry and isomerization pathways.[15,35-38] Vibronic interactions between the ground electronic state ($^2A_1$) and the extremely low-lying first excited state (^2E, 3260 cm^{-1})[28] of propynyl cause artificial symmetry breaking in single-reference methods, making investigation of the excited states difficult. The only study to investigate the higher electronic excited states of propynyl explicitly was carried out by Eisfeld,[28] who predicted an energy gap between the first and second excited electronic states of propynyl just shy of 7 eV. This value is unusually large for an open shell species and appears inconsistent with the results presented in this paper.

The present work examines the photodissociation dynamics of both propargyl and propynyl at 248 nm and 193 nm by fast beam photofragment translational spectroscopy. Figure 2.1 shows an energy level diagram of the propargyl and propynyl isomers, their respective anions, and the accessible photodissociation channels along with arrows representing the dissociation laser wavelengths. The values given in Figure 2.1 for H loss, H_2 loss, and the CH_3 loss channels were calculated from the heats of formation given by Nguyen *et al.*[38] and represent contributions from theory and experiment. The energy of the CH + C_2H_2 asymptote was taken from the ion-molecule thermochemical cycle reported by Robinson *et al.*[21] The change in enthalpy for the isomerization between the two neutral radicals was

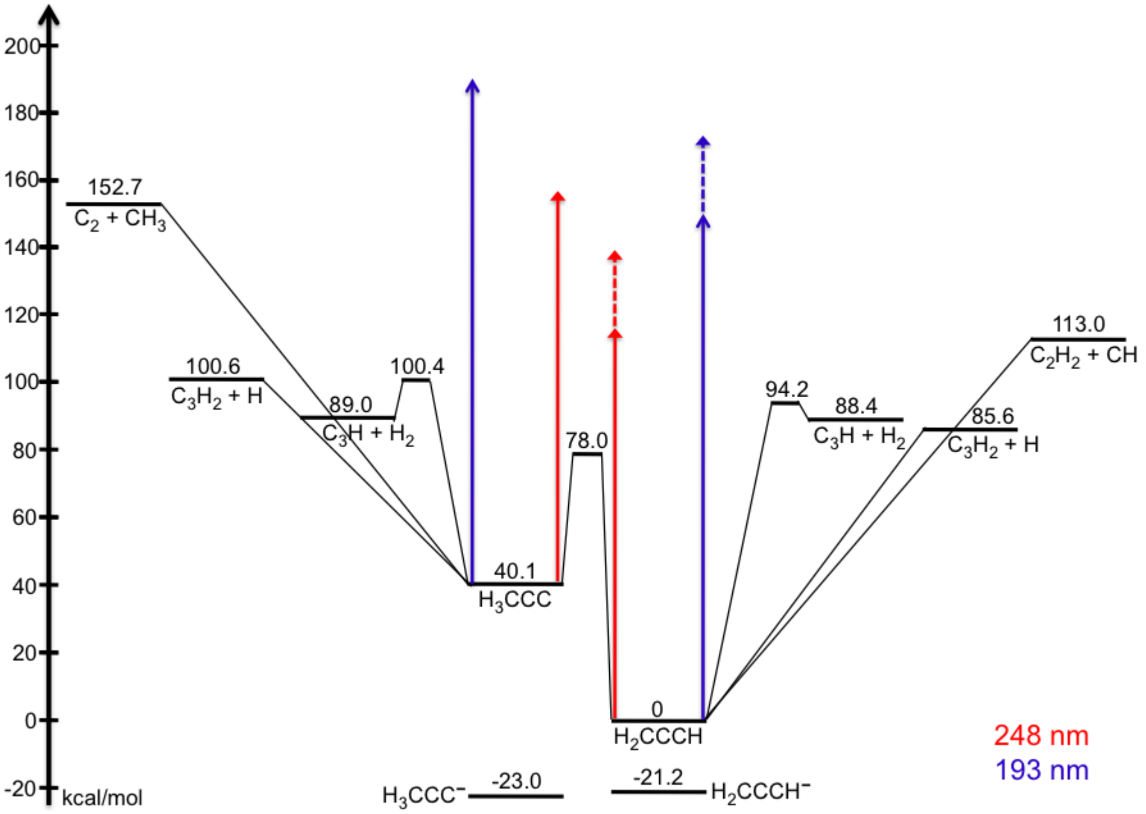

Figure 2.1. Energy level diagram of the propargyl (H_2CCCH) and propynyl (H_3CCC) radicals, their anions, and the accessible dissociation channels. The red (blue) arrows represent the energy available at 248 nm (193 nm). The dashed arrows represent the additional energy available for propargyl from photodetachment (see text).

provided by Nguyen[38] and the barrier height was calculated by Vereecken *et al.*[37] The anion energetics were calculated by Ikuta.[22]

The propargyl and propynyl radicals of this study are prepared by photodetachment of their respective anions. The near degeneracy of the anions allows us to obtain additional information about the dissociation of the propargyl radical while simultaneously observing propynyl photodissociation for the first time. The present study is complementary to previous photodissociation studies[39-42] in that we are better equipped to detect the heavy mass channels but unable to detect H loss because our experimental set-up requires product mass ratios less than about 10:1 as described below. For the same reason, all experiments described in this work were performed on the fully deuterated C_3D_3 species and ‘propargyl’ and ‘propynyl’ will henceforth refer to their respective perdeuterated isotopologs. We confirm the presence of CD loss and D_2 loss channels from the propargyl radical at 248 and 193 nm. We also find that propynyl undergoes D_2 loss at 248 nm and dissociation to CD_3 + C_2 at both wavelengths. At 193 nm, this channel is also seen for propargyl.

2. 2 Experiment

The fast beam photofragment translational spectrometer used in this study has been described in detail elsewhere.[55-57] Briefly, a pulsed, mass-selected beam of anions is photodetached by a laser pulse to produce a beam of the neutral radicals of interest. The neutrals are photodissociated by a second laser, and the recoiling photofragments are detected in coincidence by a time- and position-sensitive detector. The information collected here is used to determine photofragment translational energy distributions [$P(E_T)$ distributions].

$C_3D_3^-$ ions were produced by supersonically expanding a 50 psi gas mixture of 10% NF_3 in argon seeded with 1-trimethylsilylpropyne-d_3 into a vacuum chamber with a piezoelectric valve pulsed at 60 Hz. 1-trimethylsilylpropyne (Aldrich, 99%) was used as received and deuterated by standard methods.[58] The pulsed jet expansion passed through an electrical discharge and intersected an electron beam. Propynyl anions were preferentially produced over propargyl due to the strong silicon-fluorine bond.[59] Nonetheless, as shown below, some propargyl anions were produced by isomerization in the ionization region.

The ions were collimated by a skimmer, accelerated to a beam energy of 6 keV, and then separated by mass by a Bakker time-of-flight mass spectrometer.[60,61] The ion packet was intercepted by a pulse from a XeCl excimer-pumped dye laser (Lambda-Physik LPX-200, Lambda-Physik FL 3000). This laser pulse photodetached some of the ions, and the remaining ions were deflected from the beam path, leaving a fast beam of neutral C_3D_3 radicals. Two laser wavelengths were used for photodetachment: 540 nm (2.30 eV) and 450 nm (2.76 eV). These wavelengths correspond to energies well below and just above the EA of propynyl-d_3 (2.735 eV);[54] both wavelengths are far above the electron affinity of propargyl-d_3 (0.915 eV)[21] but not energetic enough to access the first excited state of propargyl.[28,32,34,38] The C_3D_3 neutrals were then intercepted by a pulse from a second excimer laser (GAM EX-50F) operating at either 248 nm or 193 nm. This second pulse dissociated the radicals and the recoiling photofragments collided with the time- and position-sensitive detector 2.15 m downstream while the undissociated parent beam impinged upon a 5 × 8 mm^2 beam block immediately in front of the detector.

The coincidence imaging detector consists of 75 mm diameter microchannel plates (MCPs) mounted in a Z-stack configuration and coupled to a phosphor screen.[56,57] The image from the phosphor screen was split by a dichroic beam splitter with the reflected image going to a 4 × 4 multianode photomultiplier tube (PMT) array and the transmitted fraction proceeding to an image intensifier in front of a charge-coupled device (CCD) camera. The arrival times of the photofragments were acquired by the PMT and were correlated with position information from the CCD camera. Only events where two photofragments struck within the same time window and the position information from the CCD matched the rough position information from the PMT were accepted. The coincident photofragment arrival time and position information was used to infer the photofragment masses and translational energy release for each dissociation event; from this data, the center-of-mass $P(E_T)$ distribution is constructed for each product channel.

2. 3 Results and analysis

2.3.1 Photofragment identification

Because our primary method of identifying and separating the molecule of interest in the beam is by mass-selection and propargyl and propynyl are isomeric, it was necessary to ensure that propynyl was actually being produced. Figure 2.2 shows a plot of MCP signal intensity for photodetachment laser energies above and below the EA of propynyl. This plot corresponds to a photodetachment efficiency curve and the sharp increase at the point of the propynyl EA indicates that propynyl was indeed produced. However, there is nonzero signal below the propynyl EA that must arise from photodetachment of the propargyl anion. Based on the photodetachment signal, the ratio of propynyl to propargyl above the propynyl EA is approximately 2 to 1.

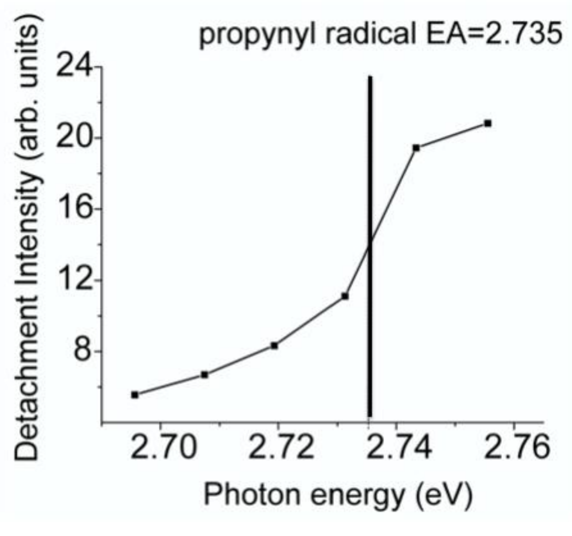

Figure 2.2 Photodetachment efficiency curve as a function of photon energy in eV. The bold vertical line marks the electron affinity of the propynyl radical.

Figure 2.3 shows the mass distributions for experiments performed at a dissociation laser wavelength of 248 nm. At a detachment laser wavelength of 540 nm (Fig. 2.3A), where only propargyl should be present, the observed photofragment masses correspond to D_2 loss and CD loss channels. The mass ratio of photofragments in the D loss channel is too large for both fragments to be detected simultaneously and that channel thus remains unobserved throughout this study. At 450 nm detachment (Fig. 2.3B), where propynyl is the major contributor, D_2 loss and CD loss are still observed, and a third channel corresponding to CD_3 + C_2 becomes evident, which must arise from propynyl photodissociation. The contribution from the CD_3 loss channel relative to CD loss is 0.7:1, despite the greater population of propynyl in the beam.

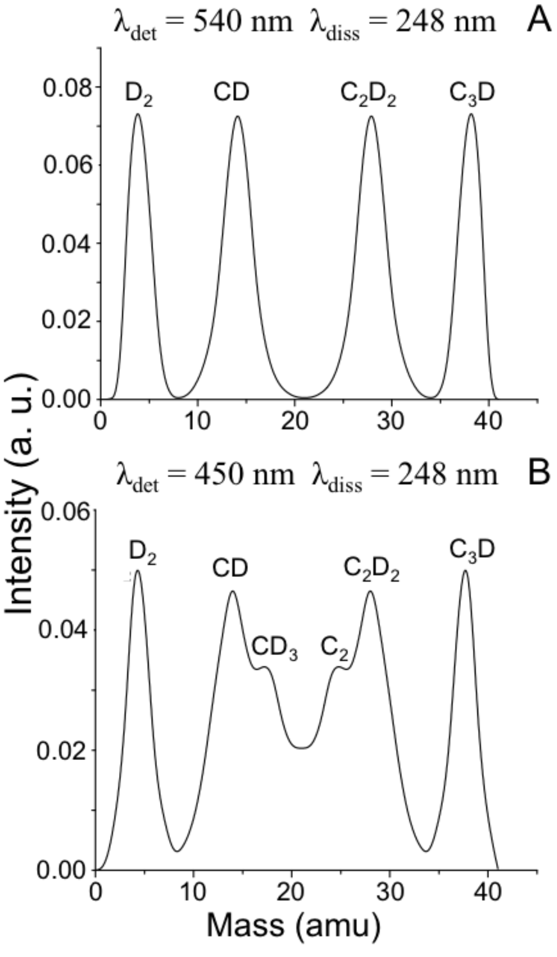

Figure 2.3 Mass distributions for photodissociation of C_3D_3 radicals at 248 nm. The top figure (A) features the photofragment masses after photodetachment of C_3D_3 anions at 540 nm, below the EA of propynyl. The bottom figure (B) features photofragment masses at 450 nm, above the propynyl EA.

The mass distributions presented in Figure 2.4 are from experiments performed at a dissociation laser wavelength of 193 nm. At 540 nm detachment (Fig. 2.4A), D_2 loss and CD loss are again apparent, though the contribution from D_2 loss is diminished in comparison. There is also evidence for CD_3 loss. Photodetachment at 450 nm produces the same mass channels, but the relative contribution of CD_3 loss to CD loss increases from 0.7:1 to 1.8:1. Hence, at 193 nm, propargyl dissociates mainly by CD loss with a small contribution from CD_3 loss, while CD_3 loss is the main channel for propynyl.

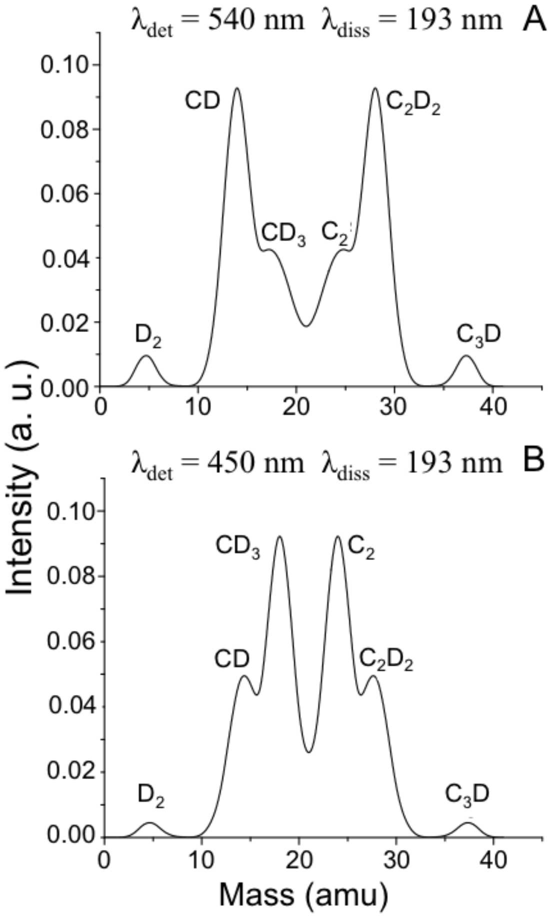

Figure 2.4 Mass distributions for photodissociation of C_3D_3 radicals at 193 nm. The top figure (A) features the photofragment masses after photodetachment of C_3D_3 anions at 540 nm, below the EA of propynyl. The bottom figure (B) features photofragment masses at 450 nm, above the propynyl EA.

2.3.2 Photofragment translational energy distributions

After the photofragment masses have been determined, the center-of-mass photofragment translational energy distributions (*P(E_T)*) are constructed from the coincidence data for each product channel. Because of the presence of the beam block in the center of the detector and the finite radius of the MCPs, certain photodissociation events are detected with less efficiency than others and some events will not be detected at all. In order to correct for this, a detector acceptance function (DAF)[62] constructed from geometric parameters of the experiment is used to normalize the raw $P(E_T)$ distributions. With the exception of the D_2 loss channels, every product channel in every data set produced a $P(E_T)$ distribution sharply peaked at exactly zero E_T when normalized by the DAF. We suspect this peak at zero is an artifact of false coincidence events detected from the highly populated D loss channel. C_3D_2 fragments clustering around the beam block could be incorrectly assigned as momentum-matched fragments from the CD loss or CD_3 loss channels. This problematic effect is somewhat mitigated by discriminating fragments falling near the calculated center of dissociation, but normalization by the DAF still leads to $P(E_T)$ distributions that blow up at $E_T = 0$.

Figure 2.5 shows a sample comparison of the normalized and raw $P(E_T)$ distributions calculated from identical data. Because DAF normalization only changes the shape of the $P(E_T)$ distributions at low E_T and leaves higher E_T events essentially unaltered, we have chosen to present the raw $P(E_T)$ distributions throughout the study. With the exception of the D_2 loss channels, which remain DAF normalized and un-discriminated, all $P(E_T)$ distributions were constructed from events where photofragments struck the detector within 6 mm of the

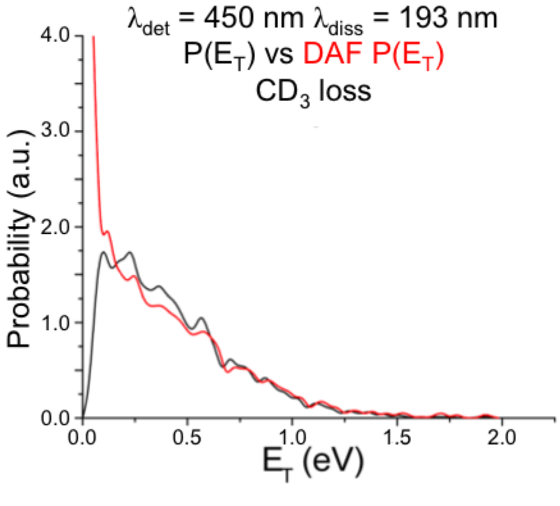

Figure 2.5 Comparison of the $P(E_T)$ distribution produced by the raw data with the 6 mm radius center discriminated (black) and the $P(E_T)$ distribution produced by normalizing the same data with the detector acceptance function (red).

calculated center of dissociation. This procedure discriminates against low kinetic energy events, especially those below about 150 meV, so our reported *P(E_T)* distributions should be treated as speculative in that energy range.

Figure 2.6A shows the *P(E_T)* distributions for D_2 loss at a dissociation laser wavelength of 248 nm. The red *P(E_T)* distribution results from 540 nm detachment and thus represents only propargyl radicals while the black distribution results from 450 nm detachment, where propynyl contributes. The propargyl *P(E_T)* distribution peaks between 0.6 and 0.8 eV (14-18.5 kcal/mol). The 450 nm *P(E_T)* distribution has a shoulder around 0.4 to 0.7 eV (9-16 kcal/mol) and a sharper peak around 0.8 eV (18.5 kcal/mol). The peak beginning around 0.7 eV is shifted to slightly higher E_T than the peak in the propargyl distribution and thus must be due to the presence of propynyl. Though D_2 loss was evident at 193 nm, there was not enough signal to construct a meaningful *P(E_T)* distribution.

Figure 2.6B presents a comparison of the 248 nm propargyl photodissociation results from this study (in red) with the work of Goncher *et al,* shown in black.[41] Note that the *P(E_T)* distributions from Goncher's study are constructed by a forward convolution fit to experimental time-of-flight distributions. The results from the two different methods are in reasonable agreement.

Figure 2.7 presents the *P(E_T)* distributions for the CD + C_2D_2 channel and compares them holding either the photodetachment wavelength or the photodissociation wavelength constant. All of the *P(E_T)* distributions peak close to zero kinetic energy release and extend to approximately 1.25 eV. Figures 2.7A and 2.7B show that at either dissociation wavelength, the *P(E_T)* distributions are similar for 540 nm and 450 nm detachment. The energy level diagram in Figure 2.1 indicates that the CD + C_2D_2 channel is accessible by both isomers in each of these experiments. Figures 2.7C and 2.7D show that at both detachment wavelengths, the 193 nm *P(E_T)* distribution shifts slightly further away from zero E_T compared to the 248 nm distribution. However, no dependence on photodissociation laser wavelength is evident for $E_T > 1.0$ eV.

The *P(E_T)* distributions for the $CD_3 + C_2$ channel at 193 nm are presented in Figure 2.8. In contrast to the situation for the CD + C_2D_2 channel, these distributions depend on the photodetachment wavelength. Both *P(E_T)* distributions for the CD_3 loss channel peak close to $E_T = 0$. CD_3 and C_2 products were observed in the 540 nm/193 nm experiment, where only propargyl radicals should be present in the beam. In the experiment with 450 nm detachment, where propynyl is dominant, the *P(E_T)* distribution (Fig. 2.6, black) also peaks near zero E_T, but is more heavily weighted to higher translational energy than the propargyl distribution.

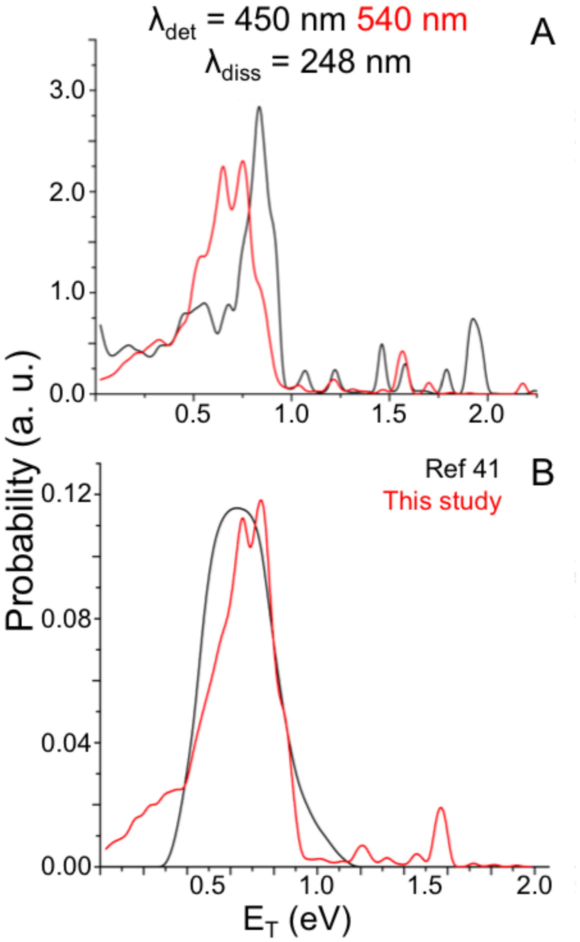

Figure 6 (A) *P(E$_T$)* distributions for the D_2 loss channel at 248 nm. The 540 nm (450 nm) detachment distribution is in red (black). (B) Comparison of 540 nm detachment distribution (red) with the distribution constructed from forward convolution (Ref. 41).

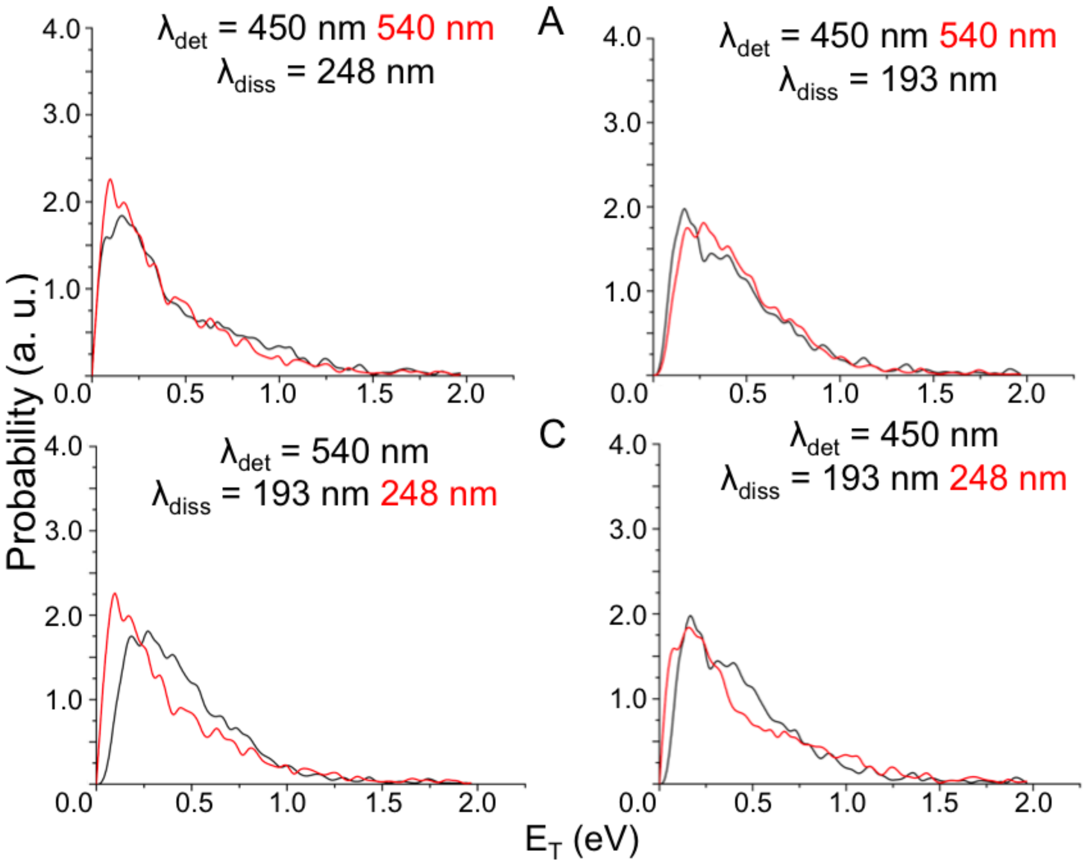

Figure 2.7 *$P(E_T)$* distributions for the CD loss channel. The distributions are pairwise compared holding photodetachment laser wavelength or photodissociation laser wavelength constant.

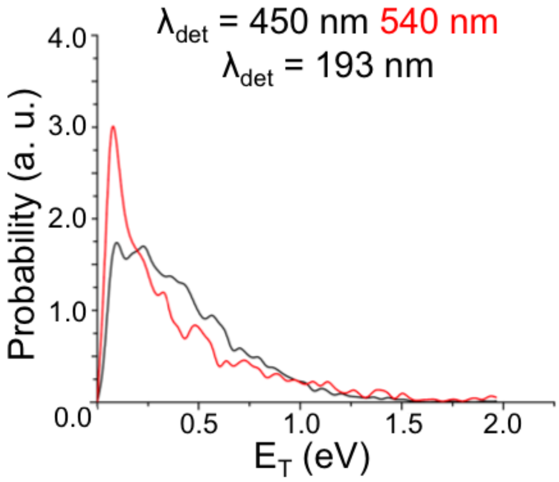

Figure 2.8 $P(E_T)$ distributions for the CD_3 loss channel at 193 nm. In red (black) is the distribution resulting from 540 nm (450 nm) photodetachment.

2. 4 Discussion

In the $P(E_T)$ distributions discussed in this report, the translational energy is given by

$$E_T = h\nu + E_{int} - E_{frag} - D_0 , \tag{2.1}$$

where $h\nu$ is the dissociation photon, E_{int} is the internal energy of the parent radical, E_{frag} is the internal energy of the photofragments, and D_0 is the dissociation energy. The internal energy of the anions is assumed to be zero in these experiments. Note that, while neutral propynyl is produced in its vibrational ground state upon photodetachment, neutral propargyl is vibrationally excited. At either detachment wavelength, a significant portion of the Franck-Condon profile of the propargyl anion photoelectron spectrum is accessible, covering electron binding energies from 0.919 to 1.9 eV,[21] so the propargyl radicals can have up to 1 eV of internal energy. The maximum energy available for translation ($E_{T,\ max}$) is then given by

$$E_{T,max} = h\nu + E_{int} - D_0 , \tag{2.2}$$

where E_{int} is 1 eV in the case of propargyl and 0 for propynyl and no available energy is deposited into internal degrees of freedom of the recoiling photofragments. The arrows in Figure 2.1 illustrate the channels that can be accessed by 248 nm (red) and 193 nm (blue) dissociation laser wavelengths, with the dashed continuations representing the additional energy from photodetachment available for propargyl. Table 2.1 lists the values of $E_{T,\ max}$ in eV, calculated from the values given in Figure 2.1.

Table 2.1 Table of maximum energy available for translation for each product channel from each isomer at each dissociation laser wavelength.

$E_{T,\,max}$ (eV)	$D_2 + C_3D$		$CD + C_2D_2$		$CD_3 + C_2$	
	D_2CCCD	D_3CCC	D_2CCCD	D_3CCC	D_2CCCD	D_3CCC
λ_{diss} = 248 nm	2.2	2.9	1.1	1.8	0.0	0.1
λ_{diss} = 193 nm	3.6	4.3	2.5	3.3	0.8	1.5

Figure 2.1 thus shows that with the additional internal energy gained from photodetachment, propargyl can dissociate to CH + C_2H_2 at 248 nm and, at 193 nm, to CH_3 + C_2 as well. Cold propynyl radicals can dissociate to both channels at both wavelengths, but the CH_3 + C_2 channel is barely accessible at 248 nm, with only 0.1 eV of energy available.

The remainder of the discussion is separated into three sections, according to product channel. Sections 1, 2, and 3 will respectively discuss D_2 loss, CD + C_2D_2, and CD_3 + C_2. Each section will discuss that product channel in terms of both photodetachment and photodissociation laser wavelengths and the possible pathways to dissociation for each isomer.

2.4.1 $D_2 + C_3D$

The major motivation for this work was to investigate the dynamics of the heavy product channels of propargyl and propynyl photodissociation. Though the mass ratio of photofragments for D_2 loss (9.5:1) is at the very edge of the geometric limitations of our experiment, we were able to detect this channel and construct limited $P(E_T)$ distributions. Figure 2.6A shows $P(E_T)$ distributions for D_2 loss from propargyl (red) and propynyl (black) at 248 nm. In the propargyl distribution, the onset of the peak around 0.4 eV is close to the calculated barrier height[38] of 0.44 kcal/mol. The onset of the peak in the $P(E_T)$ distribution for propynyl near 0.7 eV (14 to 16 kcal/mol) also agrees with the 16.4 kcal/mol barrier height for that channel calculated by Nguyen. Both $P(E_T)$ distributions for D_2 loss thus peak near the exit barrier height, which is consistent with statistical dissociation over a late barrier.[38] Figure 2.6B compares the $P(E_T)$ distribution for D_2 loss with that reported by Goncher and shows reasonable agreement in the region of most intensity from 0.4 to 0.9 eV (9 to 21 kcal/mol).

2.4.2 $CD + C_2D_2$

The CD + C_2D_2 channel was observed in every experiment performed (Figures 2.3 and 2.4). $P(E_T)$ distributions are compared by photodetachment wavelength in Figures 2.7A and 2.7B. The similarity of the distributions at either photodissociation wavelength with photodetachment energies above and below the EA of propynyl suggests that propargyl is the major contributor to this dissociation pathway. When propynyl is present, there is enough available energy to access this channel via isomerization to propargyl, but our experiment offers no compelling evidence that this occurs.

Each $P(E_T)$ distribution extends to around 1.4 eV, lower than the $E_{T,\ max}$ values expected from Table 2.1, indicating the available energy is retained in internal modes. Figures 2.7C and 2.7D compare the $P(E_T)$ distributions by dissociation wavelength at either detachment wavelength. At either detachment wavelength, the average E_T increased as the dissociation laser energy increased. At 540 nm detachment, the average E_T increases from 0.30 ± 0.02 eV to 0.40 ± 0.02 eV going from 248 nm to 193 nm. For 450 nm detachment, the average E_T increases from 0.33 ± 0.02 eV to 0.40 ± 0.02 eV going from 248 nm to 193 nm. There is no apparent dependence of the maximum observed translational energy on dissociation wavelength. The general shape of all the $P(E_T)$ distributions peaking near zero E_T suggests the photodissociation occurs by a statistical dissociation following internal conversion to the ground electronic state in the absence of a barrier.

No theoretical studies have explicitly discussed the photodissociation dynamics of the CH/CD loss channel, but our results are generally consistent with calculations[15,35-37,63] performed on the CH ($^2\Pi$) + acetylene reaction that all predict a barrierless initial addition. These studies predict that dissociation to CH and acetylene proceeds indirectly, either by isomerization to cycloprop-2-enyl ($C_S\ ^2A'$) or HC-CH-CH ($C_1\ ^2A$) followed by CH loss or by dissociation to CH and vinylidene, which then isomerizes to acetylene. Vereecken suggests[37] direct dissociation to CH and acetylene is possible, but does not elaborate on the reaction pathway. The $P(E_T)$ distributions we report are consistent with any of these pathways, and it should be noted that our detector cannot distinguish between acetylene and vinylidene.

2.4.3 $CD_3 + C_2$

The $CD_3 + C_2$ channel is the highest-lying channel investigated in this study. This channel does not appear in the mass distribution for 540 nm detachment and 248 nm dissociation as seen in Figure 2.3A, in agreement with the energetics illustrated in Figure 1. Some CD_3 loss is evident at 450 nm/248 nm in Figure 2.3B, and this must come from propynyl. However, no $P(E_T)$ distribution could be constructed owing to the very low value of $E_{T,\ max}$ (see Table 2.1) and the associated problems discussed in Section 2.3. CD_3 loss is evident at both detachment energies in the 193 nm dissociation experiments. This channel is expected for the propynyl radicals present after 450 nm photodetachment. After 540 nm detachment, where only propargyl is present, this channel most likely occurs by isomerization from propargyl to propynyl over the easily accessible barrier shown in Figure 2.1.

Figure 2.8 (black) shows the $P(E_T)$ distribution for CD_3 loss from propynyl and similarly suggests a barrierless, statistical dissociation from a vibrationally excited ground state following internal conversion. This mechanism agrees well with the calculated heats of reaction and formation,[15,36-38] but further experiments and calculations on the electronically excited states of propynyl are needed to determine what excited states are responsible for the absorption. The red curve in Figure 2.8 shows the $P(E_T)$ distribution resulting from 193 nm photodissociation of propargyl. The average E_T for propargyl and propynyl is 0.27 ± 0.02 eV and 0.37 ± 0.02 eV, respectively. The difference presumably reflects the greater amount of energy available from the higher lying propynyl isomer (see Figure 2.1 and Table 2.1).

To our knowledge, the results presented here represent the first experimental account of propynyl absorption in the UV region and the first observation of its dissociation products. These results suggest Eisfeld's calculations[28] overestimate the energy of the second electronic excited state by over 1 eV.

2. 5 Conclusions

The photodissociation of the propargyl-d_3 and propynyl-d_3 radicals at 248 nm and 193 nm was studied using fast beam photofragment translational spectroscopy. In this experiment, the radicals were prepared by photodetachment of the corresponding anions, the resulting radicals were photodissociated, and the photofragments were collected and analyzed using a coincidence imaging detector. In the ion source, a mixture of propargyl and propynyl anions was produced; we were able to distinguish between them by photodetaching at 540 nm, where only propargyl was energetically accessible, and at 450 nm, where both radicals were accessible. At each dissociation wavelength, the primary photoproducts were identified and translational energy ($P(E_T)$) distributions were measured.

The observed dissociation channels were $D_2 + C_3D$, $CD + C_2D_2$, and $CD_3 + C_2$. The D atom loss channel, previously shown to be the dominant channel in propargyl photodissociation,[41] could not be seen in this experiment owing to the large disparity in product masses. D_2 loss was observed at 248 nm from both radicals. For this channel, the $P(E_T)$ distributions from propargyl and propynyl peaked at 0.4 eV and 0.7 eV, respectively, consistent with small exit barriers that were calculated previously.[38] At 193 nm, D_2 loss was also seen but the signal was too low to develop a $P(E_T)$ distribution. The propargyl radical underwent CD loss at both dissociation wavelengths and some CD_3 loss at 193 nm. CD_3 loss was seen from propynyl at both wavelengths. All $P(E_T)$ distributions for CD and CD_3 loss peaked very close to zero translational energy, consistent with dissociation on the ground state surface with no exit barrier relative to the separated products.

Our results represent the first study of propynyl photodissociation, and the first characterization of the CD and CD_3 loss channels from the primary photodissociation of propargyl. They offer further evidence that propargyl dissociates when excited at 248 nm, and show that propynyl has accessible electronic states at 248 and 193 nm. These conclusions are at variance with a recent theoretical study[28] of the propargyl and propynyl excited states, suggesting that additional calculations are warranted.

Acknowledgments

This work was supported by the Director, Office of Basic Energy Sciences, Chemical Sciences Division of the U.S. Department of Energy under Contract No. DE-AC02-05CH11231. L.C. acknowledges the Swiss National Science Foundation. P.E.C. gratefully acknowledges Paul Armstrong for his help with the deuteration of the sample precursor.

References

1 C. H. Wu and R. D. Kern, J. Phys. Chem. **91**, 6291 (1987).

2 I. Cherchneff and J. R. Barker, Astrophys. J. **394**, 703 (1992).

3 I. Cherchneff, J. R. Barker, and A. Tielens, Astrophys. J. **401**, 269 (1992).

4 C. L. Morter, S. K. Farhat, J. D. Adamson, G. P. Glass, and R. F. Curl, J. Phys. Chem. **98**, 7029 (1994).

5 C. Ochsenfeld, R. I. Kaiser, Y. T. Lee, A. G. Suits, and M. HeadGordon, J. Chem. Phys. **106**, 4141 (1997).

6 R. I. Kaiser, Chem. Rev. **102**, 1309 (2002).

7 R. I. Kaiser and A. M. Mebel, Int. Rev. Phys. Chem. **21**, 307 (2002).

8 B. R. Giri, H. Hippler, M. Olzmann, and A. N. Unterreiner, Phys. Chem. Chem. Phys. **5**, 4641 (2003).

9 J. A. Miller and S. J. Klippenstein, J. Phys. Chem. A **107**, 7783 (2003).

10 Y. Georgievskii, J. A. Miller, and S. J. Klippenstein, Phys. Chem. Chem. Phys. **9**, 4259 (2007).

11 E. H. Wilson, S. K. Atreya, and A. Coustenis, Journal of Geophysical Research-Planets **108** (2003).

12 P. Botschwina, R. Oswald, J. Flugge, and M. Horn, Zeitschrift Fur Physikalische Chemie-International Journal of Research in Physical Chemistry & Chemical Physics **188**, 29 (1995).

13 X. Krokidis, N. W. Moriarty, W. A. Lester, and M. Frenklach, Chem. Phys. Lett. **314**, 534 (1999).

14 J. A. W. Harkless and W. A. Lester, J. Chem. Phys. **113**, 2680 (2000).

15 S. E. Wheeler, K. A. Robertson, W. D. Allen, H. F. Schaefer, Y. J. Bomble, and J. F. Stanton, J. Phys. Chem. A **111**, 3819 (2007).

16 J. D. DeSain and C. A. Taatjes, J. Phys. Chem. A **107**, 4843 (2003).

17 K. Tanaka, Y. Sumiyoshi, Y. Ohshima, Y. Endo, and K. Kawaguchi, J. Chem. Phys. **107**, 2728 (1997).

18 K. Tanaka, T. Harada, K. Sakaguchi, K. Harada, and T. Tanaka, J. Chem. Phys. **103**, 6450 (1995).

19 L. Yuan, J. DeSain, and R. F. Curl, J. Mol. Spectrosc. **187**, 102 (1998).

20 J. M. Oakes and G. B. Ellison, J. Am. Chem. Soc. **105**, 2969 (1983).

21 M. S. Robinson, M. L. Polak, V. M. Bierbaum, C. H. Depuy, and W. C. Lineberger, J. Am. Chem. Soc. **117**, 6766 (1995).

22 S. Ikuta, J. Mol. Struct. (Theochem) **434**, 121 (1998).

23 B. S. Jursic, J. Mol. Struct. (Theochem) **505**, 233 (2000).

24 R. K. Sreeruttun, P. Ramasami, G. Yan, C. S. Wannere, P. V. Schleyer, and H. F. Schaefer, Int. J. Mass. Spectrom. **241**, 295 (2005).

25 F. P. Lossing, Can. J. Chem. **50**, 3973 (1972).

26 D. W. Minsek and P. Chen, J. Phys. Chem. **94**, 8399 (1990).

27 T. Gilbert, R. Pfab, I. Fischer, and P. Chen, J. Chem. Phys. **112**, 2575 (2000).

28 W. Eisfeld, Phys. Chem. Chem. Phys. **7**, 3924 (2005).

29 D. A. Ramsay and Thistlet.P, Can. J. Phys. **44**, 1381 (1966).

[30] A. Fahr, P. Hassanzadeh, B. Laszlo, and R. E. Huie, Chem. Phys. **215**, 59 (1997).
[31] A. Fahr and A. H. Laufer, J. Phys. Chem. A **109**, 2534 (2005).
[32] H. Honjou, M. Yoshimine, and J. Pacansky, J. Phys. Chem. **91**, 4455 (1987).
[33] P. Botschwina, R. Oswald, J. Flugge, and M. Horn, Z. Phys. Chem. **188**, 29 (1995).
[34] W. Eisfeld, J. Phys. Chem. A **110**, 3903 (2006).
[35] R. Guadagnini, G. C. Schatz, and S. P. Walch, J. Phys. Chem. A **102**, 5857 (1998).
[36] A. M. Mebel, W. M. Jackson, A. H. H. Chang, and S. H. Lin, J. Am. Chem. Soc. **120**, 5751 (1998).
[37] L. Vereecken, K. Pierloot, and J. Peeters, J. Chem. Phys. **108**, 1068 (1998).
[38] T. L. Nguyen, A. M. Mebel, and R. I. Kaiser, J. Phys. Chem. A **105**, 3284 (2001).
[39] W. M. Jackson, D. S. Anex, R. E. Continetti, B. A. Balko, and Y. T. Lee, J. Chem. Phys. **95**, 7327 (1991).
[40] H. J. Deyerl, I. Fischer, and P. Chen, J. Chem. Phys. **111**, 3441 (1999).
[41] S. J. Goncher, D. T. Moore, N. E. Sveum, and D. M. Neumark, J. Chem. Phys. **128** (2008).
[42] L. R. McCunn, B. L. FitzPatrick, M. J. Krisch, L. J. Butler, C. W. Liang, and J. J. Lin, J. Chem. Phys. **125** (2006).
[43] T. L. Nguyen, A. M. Mebel, S. H. Lin, and R. I. Kaiser, J. Phys. Chem. A **105**, 11549 (2001).
[44] P. Kebarle, J. Chem. Phys. **39**, 2218 (1963).
[45] S. Satyapal and R. Bersohn, J. Phys. Chem. **95**, 8004 (1991).
[46] K. Seki and H. Okabe, J. Phys. Chem. **96**, 3345 (1992).
[47] W. Z. Sun, K. Yokoyama, J. C. Robinson, A. G. Suits, and D. M. Neumark, J. Chem. Phys. **110**, 4363 (1999).
[48] X. Chen, Y. Ganot, I. Bar, and S. Rosenwaks, J. Chem. Phys. **113**, 5134 (2000).
[49] S. Harich, J. J. Lin, Y. T. Lee, and X. Yang, J. Chem. Phys. **112**, 6656 (2000).
[50] R. H. Qadiri, E. J. Feltham, E. E. H. Cottrill, N. Taniguchi, and M. N. R. Ashfold, J. Chem. Phys. **116**, 906 (2002).
[51] R. H. Qadiri, E. J. Feltham, N. H. Nahler, R. P. Garcia, and M. N. R. Ashfold, J. Chem. Phys. **119**, 12842 (2003).
[52] Y. Ganot, S. Rosenwaks, and I. Bar, J. Chem. Phys. **120**, 8600 (2004).
[53] J. C. Robinson, N. E. Sveum, S. J. Goncher, and D. M. Neumark, Mol. Phys. **103**, 1765 (2005).
[54] J. Zhou, E. Garand, W. Eisfeld, and D. M. Neumark, J. Chem. Phys. **127** (2007).
[55] R. E. Continetti, D. R. Cyr, R. B. Metz, and D. M. Neumark, Chem. Phys. Lett. **182**, 406 (1991).
[56] A. A. Hoops, J. R. Gascooke, A. E. Faulhaber, K. E. Kautzman, and D. M. Neumark, Chem. Phys. Lett. **374**, 235 (2003).

57 A. A. Hoops, J. R. Gascooke, K. E. Kautzman, A. E. Faulhaber, and D. M. Neumark, J. Chem. Phys. **120**, 8494 (2004).

58 K. S. Feldman and D. A. Mareska, Journal of Organic Chemistry **64**, 5650 (1999).

59 C. H. Depuy, V. M. Bierbaum, L. A. Flippin, J. J. Grabowski, G. K. King, and R. J. Schmitt, J. Am. Chem. Soc. **101**, 6443 (1979).

60 J. M. B. Bakker, J. Phys. E **6**, 785 (1973).

61 J. M. B. Bakker, J. Phys. E **7**, 364 (1974).

62 R. E. Continetti, D. R. Cyr, D. L. Osborn, D. J. Leahy, and D. M. Neumark, J. Chem. Phys. **99**, 2616 (1993).

63 S. P. Walch, J. Chem. Phys. **103**, 7064 (1995).

Chapter 3

Intramolecular Competition in the Photodissociation of C_3D_3 Radicals at 248 and 193 nm

The contents of this chapter have been published in Phys. Chem. Chem. Phys. **12**, 10714 (2010).

Motivated by recent experimental work, a theoretical study of the photodissociation of perdeuterated propargyl (D_2CCD) and propynyl (D_3CCC) radicals has been carried out, focusing on the C-C bond cleavage and D_2 loss channels. High-level *ab initio* calculations were carried out, and RRKM rate constants were calculated for isomerization and dissociation pathways. The resulting reaction barriers, microcanonical rate constants and product branching ratios are consistent with the experimental findings, supporting the overall mechanism of internal conversion followed by statistical dissociation on the ground state surface. We found loose transition states and very low exit barriers for two of the C-C bond cleavage channels and an additional CD_2 + CCD channel, which had not been reported previously. Our results probe the extent of propargyl and propynyl isomerization prior to dissociation at 248 and 193 nm and deliver a comprehensive picture of all ongoing molecular dynamics.

3. 1 Introduction

The reaction dynamics of small hydrocarbon radicals are of great interest owing to their important role in combustion, planetary atmospheres and interstellar clouds.[1-12] The chemistry of these systems is often governed by the dynamics of a few key radical species, one of which is the propargyl (H_2CCCH) radical. This species is the most stable of all C_3H_3 isomers and its self-reaction is believed to form the first benzene ring in the combustion of hydrocarbons.[1, 13-15] Subsequent reactions of propargyl radicals with benzene lead to polycyclic aromatic hydrocarbons (PAH) and ultimately soot.[1, 4, 8-10, 12, 16-20] The energetics and dissociation dynamics of propargyl on its ground electronic state have been investigated in numerous experimental and theoretical studies. In this work, motivated by a recent experimental study,[21] we present a theoretical study of the photodissociation dynamics of the propargyl radical and its isomer, the propynyl radical (H_3CCC), at high energies with emphasis on the H_2 loss and C-C bond cleavage channels.

The ground state structure and vibrational frequencies of the propargyl radical have been determined using microwave[22] and infrared[23, 24] spectroscopy. Its electron affinity[25-27] is 0.918 eV and its ionization potential[28, 29] is 8.67 eV. Ramsay *et al.*[30] were the first to probe the excited states of propargyl radical. Fahr *et al.*[31] assigned an absorption band around 240 nm to the $\tilde{B}\,^2B_1 \leftarrow \tilde{X}\,^2B_1$ transition. They also observed a strong absorption band around 240 nm upon photodissociation of allene, propyne and 2-butyne, which they attributed to contributions from both propargyl and propynyl radicals.[32]

Much less information is available about the propynyl radical, as it lies about 42 kcal/mol higher in energy than propargyl.[20] Thus, while propargyl can be produced by the photodissociation of allene, no photolytic pathways to propynyl have been found.[33, 34] However, propynyl can be generated by anion photodetachment. The resulting photoelectron spectrum has been reported in two experiments[26, 35] yielding an electron affinity of 2.735 eV

Several laboratories have investigated the ultraviolet photolysis of propargyl. Jackson *et al.*[36] reported secondary photodissociation of propargyl in the photolysis of allene. They observed mainly H loss and a small amount of H_2 and CH production. The H loss channel was further investigated by direct photodissociation of propargyl around 240 nm by Deyerl *et al.*[37] and Goncher *et al.*[38] It was also detected in the secondary photodissociation of propargyl at 157 nm by McCunn *et al.*[39] H_2 loss was detected in the latter two experiments and found to be a relatively minor channel (~3% at 248 nm[38]). Derived product translational energy distributions suggested a loose transition state for H loss and an exit barrier of about 10 kcal/mol for H_2 loss. These results were consistent with internal conversion followed by statistical dissociation on the electronic ground state. A recent high-*n* Rydberg atom time-of-flight study of the UV photodissociation of propargyl by Zhen *et al.*[40] found a fully isotropic angular distribution of the H-atom photoproduct, which is another indication of statistical ground state dissociation.

On the theoretical side, the ground state of propargyl radical has been studied with several different *ab initio* methods[41-43] and Harkless *et al.*[44] calculated the heat of formation and atomization energy using the Quantum Monte Carlo method. The structure of relevant ions and associated quantities such as electron affinities and ionization potentials have been calculated by Botschwina *et al,*[45] Ikuta,[46] and Jursic.[47] Eisfeld calculated the excited states of both propynyl and propargyl radicals and their respective absorption spectra.[48, 49] These calculations, however, predicted no significant absorption around 240 nm for either radical, which is in disagreement with several experimental assignments.[21, 31, 32, 37, 38, 40] Yarkony and coworkers report several conical intersections in propynyl[50, 51] and were able to simulate the high-resolution anion photoelectron spectrum.[35] Finally, several studies have addressed the thermochemistry of various C_3H_3 species relevant to soot formation,[20] in the photodissociation of propyne and allene[52] and in the C + C_2H_3 reaction.[53] Nguyen *et al.*[54] presented an *ab initio*/RRKM study of the C + C_2H_3 and CH + C_2H_2 reactions as well as the photodissociation of propargyl at 242 and 193 nm. Their microcanonical rate constants showed that H atom loss was by far the dominant photodissociation channel, with branching ratios of only 3% and 5.5% for H_2 loss at 242 and 193 nm, respectively.

We recently used fast radical beam photofragment translational spectroscopy[55] to look at the heavy product channels from propargyl photodissociation in more detail, and to perform the first investigation of propynyl photodissociation.[21] In this experiment, perdeuterated (C_3D_3) propargyl and propynyl radicals were prepared by photodetachment from their respective anions. The propargyl and propynyl anions are nearly isoenergetic, enabling both to be formed from the reaction of F^- with $CD_3C\equiv C$-TMS,[26] while the electron affinity of propargyl is 1.8 eV lower than that of propynyl. Hence, at a photodetachment wavelength of 540 nm, only the propargyl radical is accessible, whereas photodetachment at 450 nm (just above the electron affinity of propynyl) produces a mixture of ~20% propargyl and ~80% propynyl.

The mass distributions from propargyl and propynyl + propargyl photodissociation at 248 and 193 nm from this experiment are shown in Figs. 3.1 and 3.2, respectively. Both photofragments from $C_3D + D_2$, $C_2D_2 + CD$, $C_2D + CD_2$, and $C_2 + CD_3$ channels were detected in coincidence and we derived the respective mass distributions and translational energy distributions. Note that the contribution from $C_2D + CD_2$ is based on the work presented here and was not identified previously. The $P(E_T)$ distributions peaked close to zero kinetic energy for the C-C bond cleavage channels, suggesting a loose transition state, while the distribution for D_2 loss peaked well away from zero, indicative of an exit channel barrier. The fast beam experiment was insensitive to the dominant D loss channel owing to the large mass ratio between the photofragments. Figs. 3.1 and 3.2 show

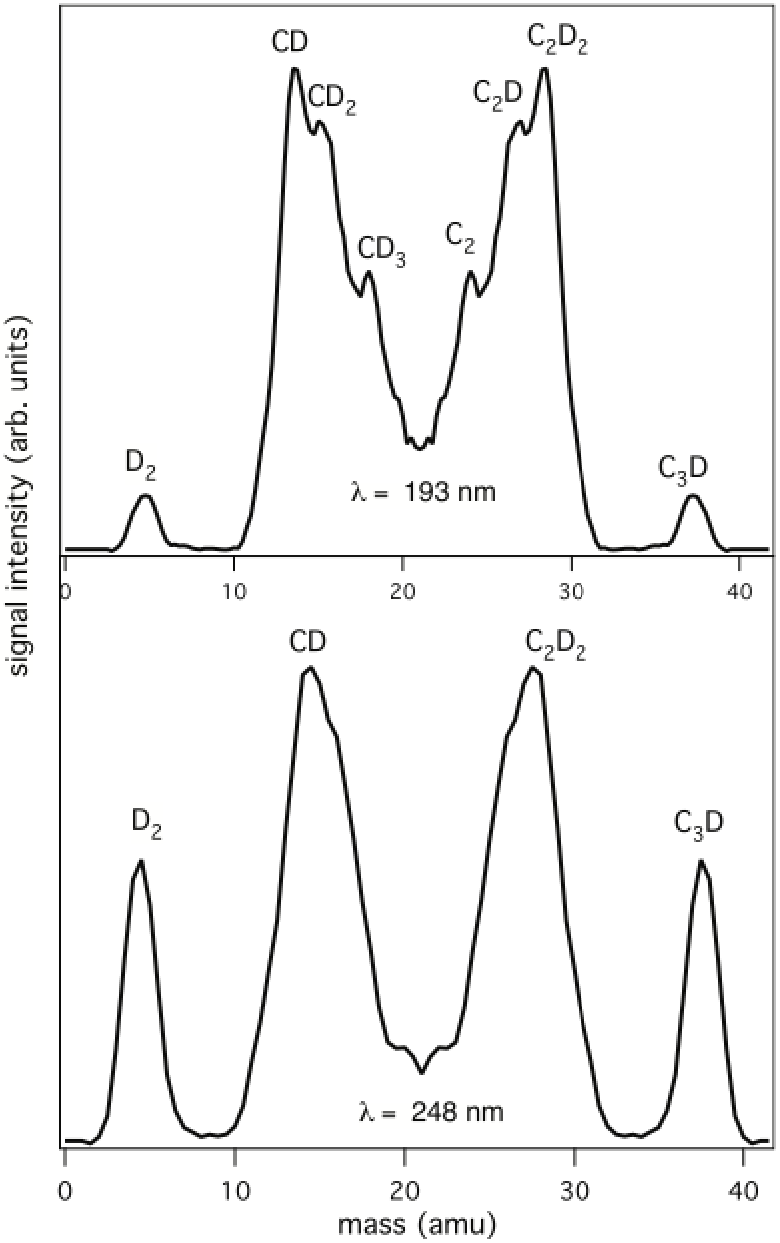

Figure 3.1 Mass distribution for photodissociation of propargyl radicals at 248 nm (lower trace) and 193 nm (upper trace) after photodetachment at 540 nm.

that whereas D_2 loss prevails over the higher-lying C-C bond cleavage channels at 248 nm, this situation is reversed at 193 nm. The observation of the C_2 + CD_3 channel from the 193 nm photodissociation of propargyl implies that some isomerization to propynyl occurred prior to dissociation. On the other hand, the mass distributions at 193 nm show that far more C_2 + CD_3 is produced from propynyl than propargyl, indicating that isomeric scrambling is far from complete.

These results motivate the work presented here, in which we map out a comprehensive C_3D_3 potential energy surface with all key species and reaction pathways relevant to the photodissociation of propargyl and propynyl radicals at 248 and 193 nm. Our study is limited to the C-C bond cleavage and D_2 loss channels that were studied in the fast beam experiment[21] since direct H-loss has already been investigated in earlier theoretical[53, 54] and experimental[37-39] studies. We also report RRKM rate constants and, from these, determine time-dependent concentrations and branching ratios for the various species produced by photoexcitation of the two radicals. The interplay between isomerization and dissociation is of particular interest. We find that isomerization from propynyl to propargyl plays a significant role in the dynamics at 248 nm, resulting in similar

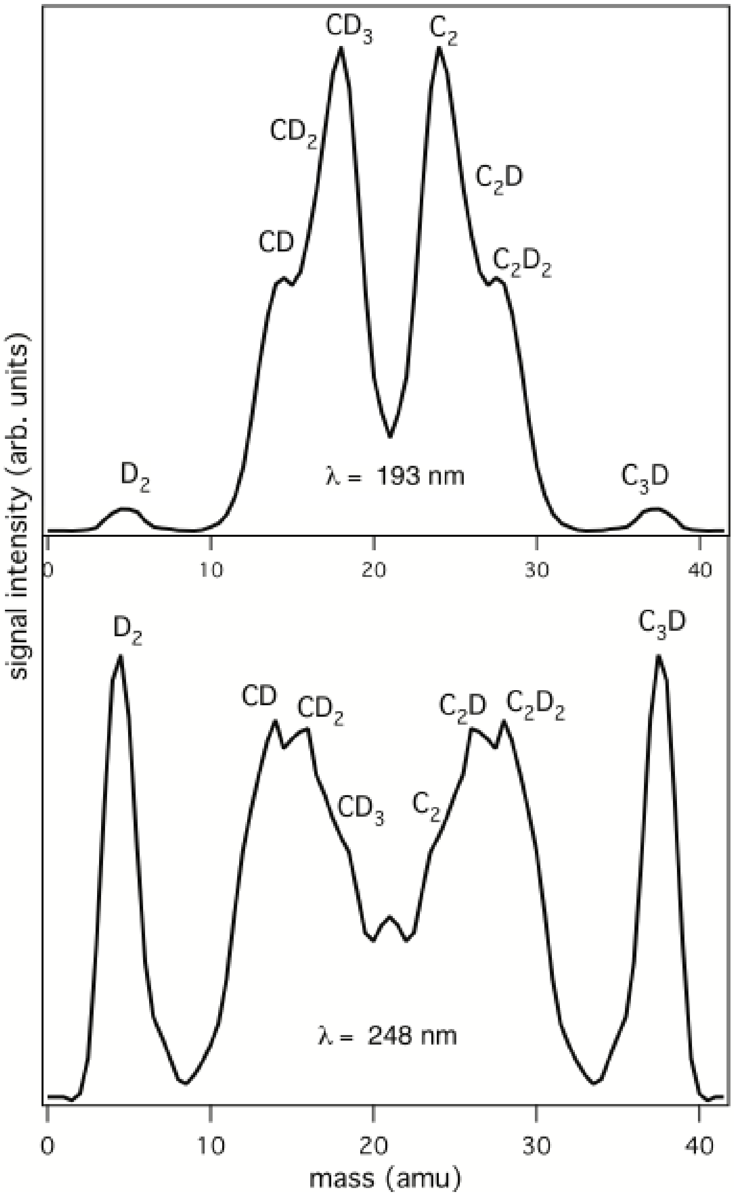

Figure 3.2 Mass distribution for photodissociation of propynyl radicals (with ~20% propargyl contribution) at 248 nm (lower trace) and 193 nm (upper trace) after photodetachment at 450 nm.

product branching from both radicals, whereas direct dissociation is much more important at 193 nm. Moreover, the theoretical results show evidence for a new channel, C_2D + CD_2, that was not considered in our experimental work.

3. 2 Theoretical Methods

3.2.1 *Ab initio* calculations. The large number of structures to be characterized to completely map out the C_3D_3 potential energy surface limited the range of available theoretical methods. Earlier studies[53, 56, 57] on similar systems were performed using Density Functional Theory (DFT) at the UBHandHLYP/cc-pVQZ[58-62] level of theory. The DFT results were compared to data obtained by Complete Active Space (CASSCF), Coupled Cluster[20, 48, 56] and Diffusion Monte Carlo methods[44] and showed very good agreement.

We performed a systematic survey of the potential energy surface to find all possible rearrangements and fragmentation pathways of the C_3H_3/C_3D_3 radicals at a given upper energy limit of about 150 kcal/mol. Fully optimized geometries and vibrational frequencies for each isomer and all connecting transition states were obtained. Transition state locations were confirmed by frequency analysis and by following the intrinsic reaction coordinates (IRC). Stationary points relevant for the calculation of the RRKM rate constants were reevaluated at the ROCCSD(T)/cc-pVXZ(X = D,T,Q) level of theory and the resulting energies were extrapolated to the complete basis set limit.[59, 63, 64] Scaled vibrational frequencies calculated at UBHandHLYP/cc-pVQZ level were used for zero-point energy corrections. All results were checked for spin contamination, which never exceeded 5%. Critical structures were checked using the CASSCF method to make sure that a single reference approach was justified.

Calculations were performed at the National Energy Resource Supercomputing Center at Lawrence Berkeley National Laboratory using Molpro,[65] Gamess[66] and Gaussian 03[67] suites of quantum chemistry programs.

3.2.2 RRKM calculations. RRKM theory[68] was used to calculate microcanonical rate constants, *k(E),* for the unimolecular reactions

$$R \xrightarrow{h\nu} R^* \longrightarrow P$$

where $h\nu$ is the photon energy, R* the critical configuration, and P the product or products. The RRKM rate constant is given by

$$k(E) = \sigma \frac{W^*(E - E_0)}{h\rho(E)} \ , \tag{3.1}$$

where W^* is the total number of states of the critical configuration with E_0 being the activation energy and $\rho(E)$ denotes the density of states of the reactant at total energy E. The reaction path degeneracy[69] σ corresponds to the number of equivalent paths leading from the reactant to the transition state. It can normally be expressed as the ratio of the symmetry numbers[70] of the transition state, σ^*, and of the reactant, σ_r, *i.e.,*

$$\sigma = \frac{\sigma_r}{\sigma^*}. \tag{3.2}$$

The densities and sum of states were calculated by the direct state-count method using the Beyer-Swinehart algorithm,[71] which was implemented in both the RRKM program of Zhu and Hase[72] and our own FORTRAN code for the calculation of rate constants. In the case of loose transition states, *i.e.,* C-C bond cleavage reactions, we calculated the intrinsic reaction coordinate (IRC) by reoptimizing the geometry at a defined fragment separation up to 4.0 Å. The harmonic frequencies obtained at each point along the IRC were used in the variational transition state theory (VTST) calculations.

Under the collision-free conditions of a molecular beam, the microcanonical kinetics can be described by a set of coupled differential equations,

$$\frac{\mathrm{d}[C]_i}{\mathrm{d}t} = \sum_n \sum_j k_n [C]_j - \sum_m k_m [C]_i, \tag{3.3}$$

where $[C]_i$ and $[C]_j$ are concentrations of various intermediates and products and k_n and k_m are microcanonical rate constants. We obtained time-dependent concentrations of the various products, intermediates and reactants using the fourth- and fifth-order Runge-Kutta method[73] to solve the system in Eq. 3.3. Product concentrations at reaction times where they have fully converged were used to calculate the branching ratios.

3. 3 Results

Fig. 3.3 shows a map of the potential energy surface, indicating the reaction channels that are relevant to the fast beam photodissociation of propynyl and propargyl radicals at 248 and 193 nm. It includes all the reactants, products, intermediate structures and transition states that were used to calculate the RRKM rate constants. An overview of all structures that were found in our survey scans of the C_3H_3 ground state potential energy surface calculated at the UBHandHLYP/cc-pVQZ level of theory is provided in the Supplementary Information. Many of these structures were discarded because they were too high in energy or had a different spin multiplicity. We used an upper energy limit of about 150 kcal/mol, which roughly corresponds to the energy of a 193 nm photon. The geometries of the tight transition states are depicted in Fig. 3.4. The critical structures shown in Fig. 3.3 were calculated at the higher ROCCSD(T)/cc-pVXZ(X = D,T,Q,V) level of theory because several transition states and fragmentation products are close in energy.

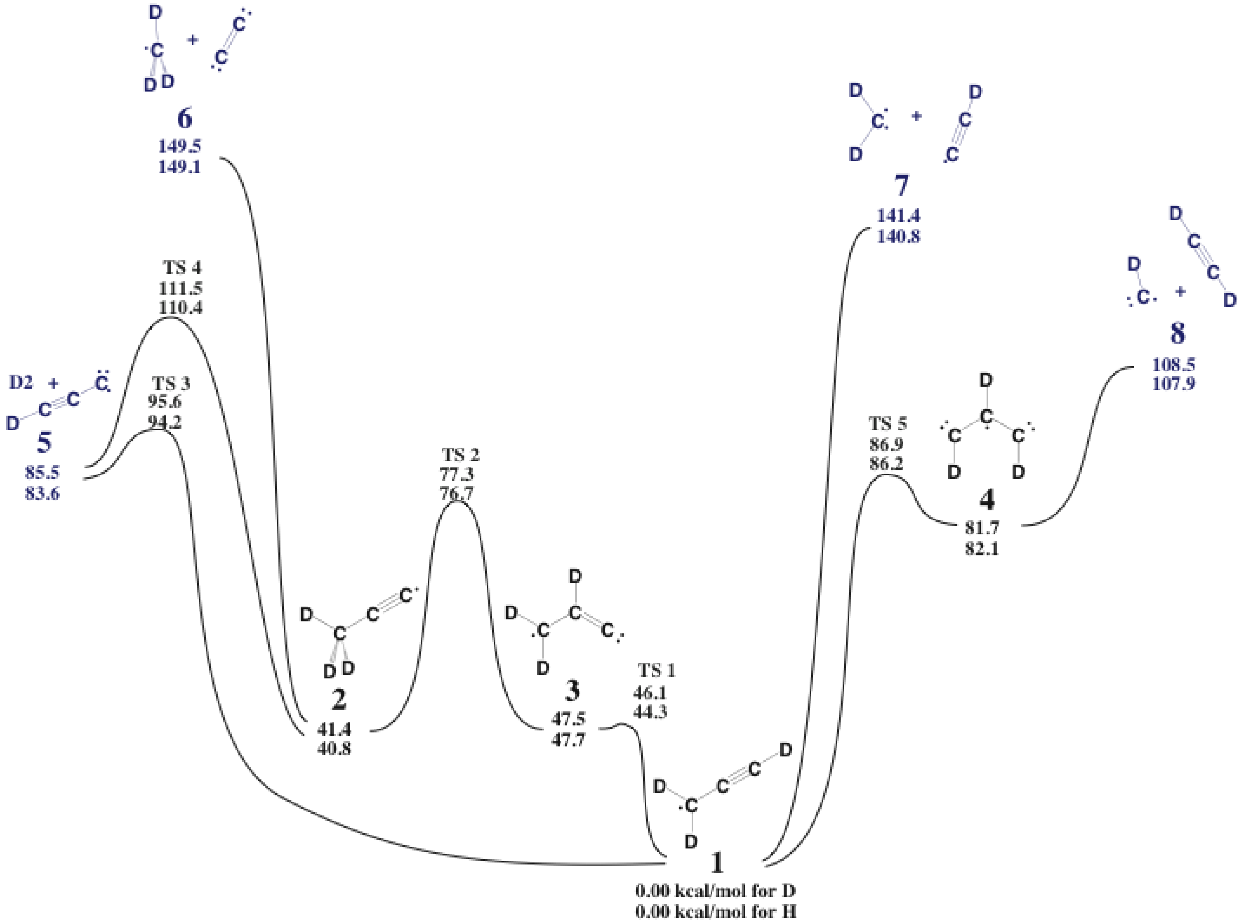

Figure 3.3 Potential energy diagram for the fragmentation channels observed in the photodissociation of propynyl and propargyl at 248 and 193 nm. Given energies are relative to propargyl ground state and calculated at the ROCCSD(T)/cc-pV*X*Z (*X*=D,T,Q)//UBHandHLYP/cc-pVQZ + ZPE(UBHandHLYP/cc-pVQZ) level of theory.

Table 3.1 compares our results with earlier calculations[53] and available experimental[74] values. Our calculated energies in Table 3.1 compare favorably to earlier calculations. The small differences between C_3H_3 and C_3D_3 result from different zero-point energies. The calculations yield somewhat lower energies for the C-C bond cleavage channels compared to experiment but agree better than previous calculations.

The RRKM rate constants at photoexcitation energies of 115 and 148 kcal/mol, corresponding to 248 and 193 nm, are given in Table 3.2 and 3.3 for propargyl and propynyl dissociation respectively. The available energy for each reaction, E_{avail}, is given as well; this value represents the sum of the photon energy minus the energy of the local minimum relative to the propargyl ground state in Table 3.2 and the propynyl ground state in Table 3.3. In Table 3.2, 1 eV of internal energy from the vertical electron detachment is added to E_{avail}, because photodetachment of the propargyl anion at 540 nm accesses the entire Franck-

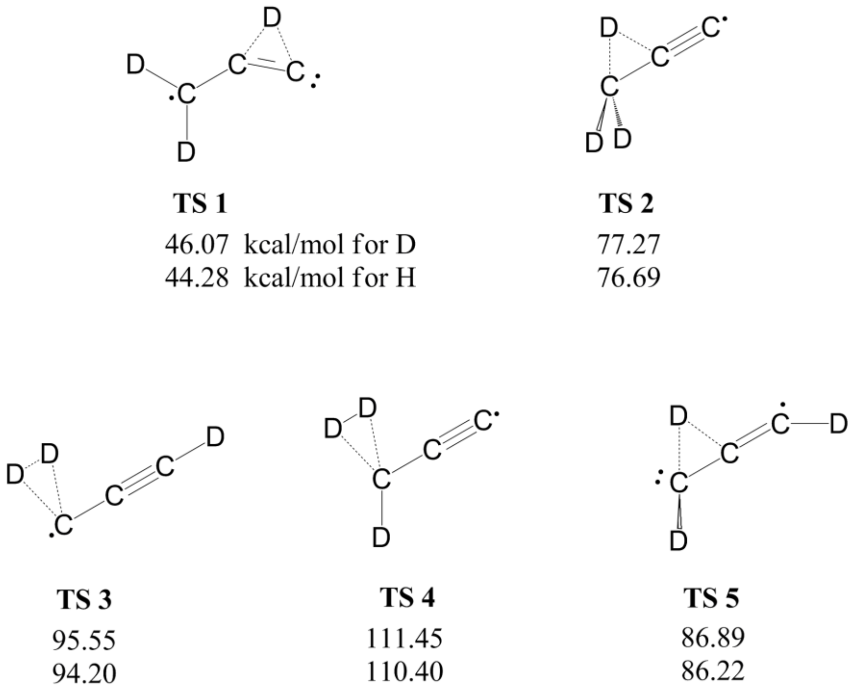

TS 1
46.07 kcal/mol for D
44.28 kcal/mol for H

TS 2
77.27
76.69

TS 3
95.55
94.20

TS 4
111.45
110.40

TS 5
86.89
86.22

Figure 3.4 Transition state geometries.

Condon profile of neutral propargyl vibrational states, which spans ~1 eV.[26] In contrast, photodetachment of the propynyl anion at 450 nm produces the propynyl radical in its ground vibrational state.[21, 35]

Sums and densities of states were calculated using the direct count method without corrections for anharmonicity since we were interested in the relative rate constants of the respective photodissociation channels. Thus, our calculated reaction rates must be considered as upper limits since the vibrational density of states of the reactant is underestimated at the high energies of the photodissociation experiment. No transition state could be located in the variational transition state theory calculations for the C-C cleavage reactions with loose transition states. However, the rate constants were converging with increasing distance between the fragments, so we used the minimum rate constant obtained at the largest calculated fragment separation.

The rate constants in Tables 3.2 and 3.3 were used in Eq. 3.3 to calculate time-dependent concentrations of each reactant, intermediate, and product shown in Fig. 3.3. The resulting time-dependent concentrations are presented in Figs 3.5 and 3.6 for photoexcitation at 248 nm and 193 nm, respectively. Table 3.4 shows the product branching ratios for the fragments observed in the photodissociation of propargyl and propynyl at 248 and 193 nm.

Table 3.1 Calculated absolute and relative energies of species relevant in C_3H_3 photodissociation. Available experimental values are shown for comparison.

structure	**total energy** (hartrees)	**relative energy** (kcal/mol)			
	CCSD(T)/CBS$^{(a)}$	$C_3D_3^{(b)}$	$C_3H_3^{(b)}$	CCSD(T)$^{(c)}$	experiment
1	-115.82201	0.00	0.00	0.0	0.0
2	-115.75924	41.4	40.8	40.1	-
3	-115.74500	47.5	47.7	46.9	-
4	-115.69068	81.7	82.1	76.3	-
5	-115.67081	85.5	83.6	84.0	
6	-115.57143	149.5	149.1	142.9	154.0
7	-115.58314	141.5	140.8	-	144.4
8	-115.63807	108.5	107.9	108.9	115.2
TS 1	-115.74596	46.1	44.3	46.6	-
TS 2	-115.69488	77.3	76.7	76.5	-
TS 3	-115.66164	95.6	94.2	94.2	-
TS 4	-115.63745	111.5	110.4	110.4	-
TS 5	-115.67919	86.9	86.2	86.8	-

(a) CCSD(T)/cc-pVXZ (X=D,T,Q, extrapolated to basis set limit)
(b) ΔG(100 K) with zero-point energy correction based on CCSD(T)/CBS energies.
(c) RCCSD(T)/6-311+G(3df,2p) energies for C_3H_3 from Ref 53.

Table 3.2 Calculated microcanonical rate constants for the photodissociation of propargyl radical at 248 and 193 nm.

Reaction				**248 nm**		**193 nm**	
react.	transition state	prod.	σ	E_{avail} (kcal/mol)	$k(E, J)$ (s^{-1})	E_{avail} (kcal/mol)	$k(E, J)$ (s^{-1})
1	TS 1	3	2	138.4	5.3×10^{11}	171.3	1.2×10^{12}
3	TS 1	1	1	90.9	9.8×10^{12}	123.8	1.1×10^{13}
3	TS 2	2	1	90.9	1.0×10^{12}	123.8	2.7×10^{12}
2	TS 2	3	3	97.0	5.6×10^{12}	129.9	1.8×10^{13}
1	TS 3	5	2	138.4	1.4×10^{10}	171.3	2.7×10^{10}
2	TS 4	5	3	97.0	2.2×10^{10}	129.9	9.8×10^{11}
2	-	6	3	97.0	-	129.9	4.2×10^{12}
1	-	7	2	138.4	-	171.3	8.0×10^{10}
4	-	8	2	56.7	5.1×10^{12}	89.58	3.4×10^{13}
1	TS 5	4	2	138.4	9.8×10^{9}	171.3	2.6×10^{11}
4	TS 5	1	2	56.7	1.2×10^{13}	89.6	3.9×10^{13}

Table 3.3 Calculated microcanonical rate constants for the photodissociation of propynyl radical at 248 and 193 nm.

Reaction				**248 nm**		**193 nm**	
react.	transition state	prod.	σ	E_{avail} (kcal/mol)	k(E, J) (s^{-1})	E_{avail} (kcal/mol)	k(E, J) (s^{-1})
1	TS 1	**3**	2	156.8	8.7×10^{11}	189.7	1.6×10^{12}
3	TS 1	**1**	1	109.3	1.0×10^{13}	142.2	1.1×10^{13}
3	TS 2	**2**	1	109.3	1.9×10^{12}	142.2	3.8×10^{12}
2	TS 2	**3**	3	115.4	1.2×10^{13}	148.3	2.7×10^{13}
1	TS 3	**5**	2	156.8	9.3×10^{10}	189.7	7.6×10^{11}
2	TS 4	**5**	3	115.4	2.7×10^{11}	148.3	3.1×10^{12}
2	-	**6**	3	115.4	3.9×10^{11}	148.3	3.2×10^{13}
1	-	**7**	2	156.8	2.4×10^{10}	189.7	4.5×10^{11}
4	-	**8**	2	75.0	1.5×10^{13}	107.9	5.6×10^{13}
1	TS 5	**4**	2	156.8	3.9×10^{10}	189.7	9.5×10^{11}
4	TS 5	**1**	2	75.0	5.6×10^{12}	107.9	4.1×10^{13}

3. 4 Discussion

In this section, key features of the C_3D_3 potential energy surface are discussed. We then consider the various dissociation channels accessed from propargyl and propynyl upon photodissociation at 248 and 193 nm. Finally, the overall ground state dynamics are considered in detail, particularly the competition between propargyl-propynyl isomerization and dissociation.

3.4.1 The C_3D_3 potential energy surface. Our survey scan revealed an abundance of possible isomerization and fragmentation pathways for both propargyl and propynyl radicals that are in principle accessible at the total energy of the experiment. As indicated in the Supplementary Information, there are many nearly isoenergetic isomers connected by relatively loose transition states. Only those isomers and transition states relevant to the photodissociation experiments are

Table 3.4 Calculated product branching ratios for the photodissociation of propargyl and propynyl radicals at 248 and 193 nm. (excluding H-atom loss)

product	**propargyl**		**propynyl**	
	248 nm	193 nm	248 nm	193 nm
5	82.9%	13.4%	61.4%	19.7%
6	0	17.4%	6.7%	62.3%
7	0	27.5%	14.6%	8.1%
8	17.1%	41.7%	17.3%	9.8%

shown in Fig. 3.3. In particular, we find that isomerization of propargyl (**1**) to propynyl (**2**) radical involves two transition states, **TS 1** and **TS 2**. **TS 2** lies 77.3 kcal/mol above propargyl and 35.9 kcal/mol above propynyl, in the other direction. TS 1 lies 1.4 kcal/mol below intermediate 3, which is an artifact of CCSD(T) energy calculations at the DFT-optimized geometries. This will, however, not affect the RRKM calculations at the photon energies used here. In either direction, the isomerization barrier is much lower than the available energy in the photodissociation experiments. This barrier also lies well below the various observed dissociation channels, particularly the C-C cleavage channels. Hence, at first glance, one might expect significant isomeric scrambling between propargyl and propynyl prior to dissociation, a hypothesis that is tested by means of the RRKM results discussed below.

3.4.2 D_2 loss. D_2 elimination from propargyl and propynyl radical leads to formation of the linear C_3D radical, which is nearly isoenergetic with cyclic C_3D.[75] D_2 loss from both radicals occurs through a three-center transition state with a substantial exit barrier. The activation energy is 95.6 kcal/mol from propargyl radical via **TS 3** and 70.0 kcal/mol from propynyl radical via **TS 4**. The barrier height for the reverse association reaction is 10.0 kcal/mol for **TS 3** and 25.9 kcal/mol for **TS 4**. The higher exit barrier for propynyl is consistent with the translational energy distributions for D_2 loss at 248 nm, which peaks at 14 kcal/mol from propargyl and 18 kcal/mol from propynyl.[21, 38] However, this difference in the experimental distributions may arise from another source, as discussed below.

3.4.3 C_2D_2 + CD. This is the lowest lying C-C bond cleavage channel. The rate limiting step is the formation of isomer **4** via **TS 5**. There are three nearly isoenergetic isomers of structure **4**, which readily interconvert and were omitted in Fig. 3.3 for the sake of simplicity. We also located a transition state connecting isomer **3** and **4**, which provides a shortcut for propynyl radical dissociation. No

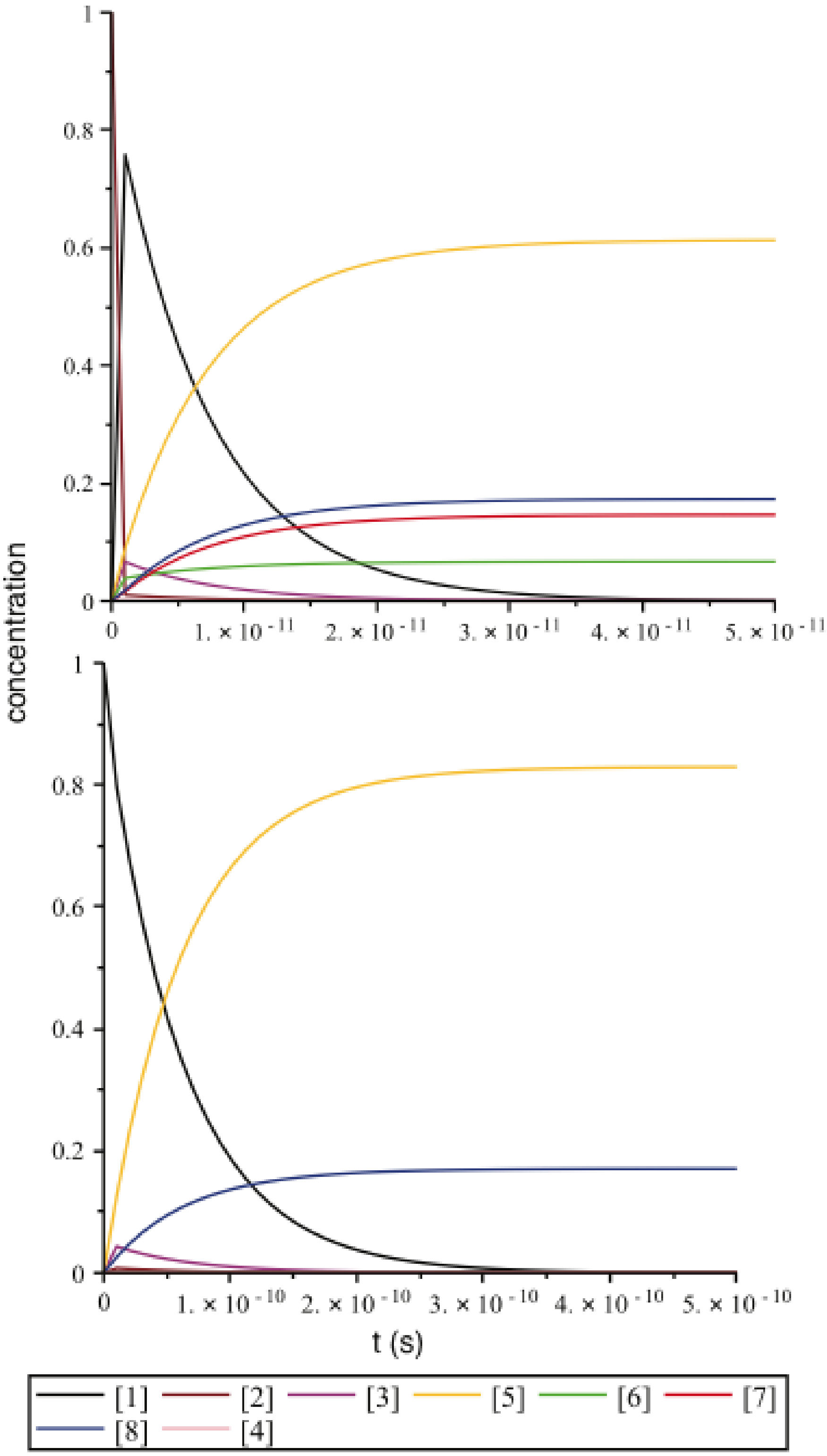

Figure 3.5 Time-dependent concentrations for propynyl (top) and propargyl (bottom) dissociation at 248 nm. See Fig. 3.3 for numbering scheme.

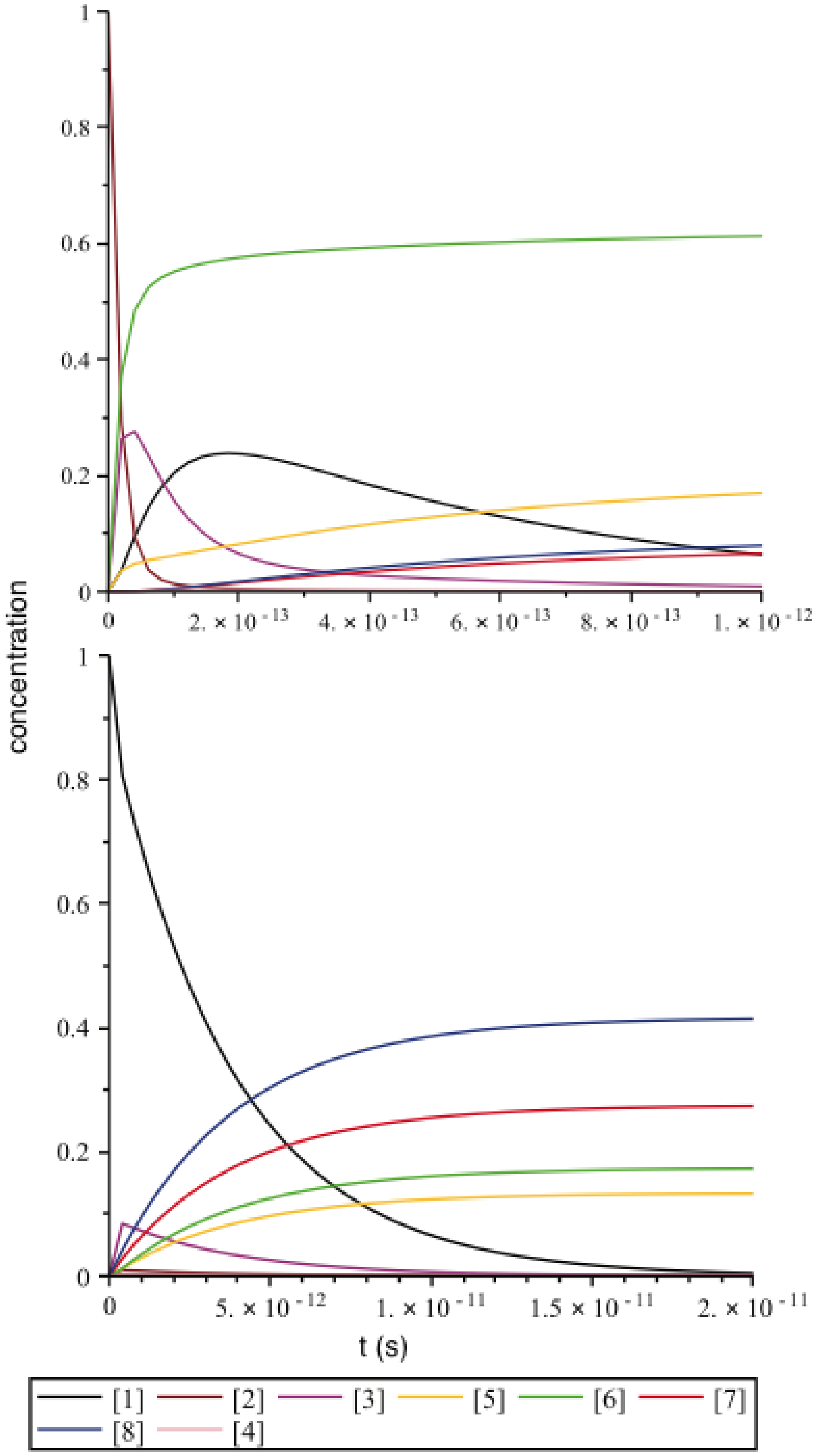

Figure 3.6 Time-dependent concentrations for propynyl (top) and propargyl (bottom) dissociation at 193 nm. See Fig. 3.3 for numbering scheme.

transition state could be found for the actual fragmentation from **4** to C_2D_2 + CD and the calculated rate constant is comparable to that for the reverse reaction of **4** back to propargyl radical. The experimental $P(E_T)$ distributions peak close to zero, as expected for statistical dissociation with no exit barrier.

3.4.4 C_2D + CD_2. This channel has not been considered in previous theoretical and experimental work. Scans along the D_2C-CCD bond revealed a smooth potential without an exit barrier leading to CD_2 and C_2D. In light of this result, we reanalyzed our experimental data including this channel, resulting in the photofragment mass distributions in Figs 3.1 and 3.2. The new channel appears as a partially resolved feature in the 193 nm photodissociation of propargyl (Fig. 3.1, upper panel). This channel is not energetically accessible in the 248 nm photodissociation of propargyl (Fig. 3.1, bottom), so in the bottom panel of Fig. 3.2 it must arise from propynyl. We also obtained translational energy distributions for this channel, all of which peaked near zero and resembled the previously reported $P(E_T)$ distributions for the other C-C bond cleavage channels,[21] consistent with dissociation through a loose transition state with no reverse barrier.

3.4.5 C_2 + CD_3. This is the highest-lying channel that was investigated in the photodissociation experiment. Scanning the presumed reaction coordinate led to a smooth potential without an exit barrier. It is a minor channel for propargyl radical dissociation at 193 nm and does not appear at all at 248 nm as seen in the mass distributions in Fig. 3.1. The soft shoulders at *m/z=18* and *m/z=24* in the mass distribution of propynyl dissociation at 248 nm in Fig. 3.2, however, indicate a small contribution of this channel, which becomes much more important at 193 nm. As previously reported, the $P(E_T)$ distributions peak near zero, as expected based on the nature of the reaction coordinate for this channel as seen in Fig. 3.3.

3.4.6 Product branching ratios. The RRKM rate constants in Tables 3.2 and 3.3 and the calculated branching ratios in Table 3.4 provide new insights into several aspects of the dissociation dynamics of propargyl and propynyl. At 248 nm, the product branching ratios for propargyl and propynyl (excluding D-atom loss) are similar, in that D_2 loss is the dominant channel, followed by channel **8**. Propynyl dissociation at 248 nm yields a small amount of channels **6** and **7**, whereas these channels are not energetically accessible from propargyl. The similarity of the branching ratios for the two radicals suggests that propynyl→propargyl isomerization is rapid, and that the main differences between the branching ratios arises from the higher available energy for propynyl photodissociation.

The time-dependent concentrations in Fig. 3.5 obtained from solving Eq. 3.3 clarify the origin of these trends. They show that at 248 nm, propargyl dissociation is dominated by D_2 loss via **TS 3**, with some production of channel **8** through **TS 5** and the intermediate **4**. Propynyl, on the other hand, isomerizes very rapidly to form energized propargyl. The dominant channel from propynyl, D_2 loss, occurs primarily from the dissociation of energized propargyl over **TS 3**; only about 7% of D_2 loss occurs via **TS4**. Overall, at 248 nm, propargyl dissociates with little or no isomerization, whereas the propynyl dynamics are driven by rapid isomerization to propargyl.

Comparison of these results to experiment is of interest, because the experiment shows that D_2 loss from propynyl at 248 nm results in slightly faster photofragments than from propargyl. Our original interpretation was that this result reflected a higher exit barrier for channel **5** from propynyl, as discussed in Section 3.4.2 and shown in earlier theoretical work.[52, 53] However, the analysis presented here suggests an alternative explanation, namely that the faster photofragments from propynyl reflect the higher E_{avail} for propargyl following isomerization. More sophisticated treatments of the dynamics are needed to determine which of these mechanisms is at play.

The situation is quite different at 193 nm. Table 3.4 indicates that at this wavelength, channel **5** is much less important for both radicals. Moreover, for propargyl, channel **8** dominates, whereas channel **6** dominates for propynyl. All of these results are consistent with the experimental mass distributions in Figs. 3.1 and 3.2. The calculations and experiment show that some isomerization clearly occurs, otherwise no C_2 + CD_3 would be produced from propargyl, for example. However, it is also clear that the identity of the starting radical plays a more important role at 193 nm than at 248 nm.

Again, one can understand these results with reference to the concentration plots in Fig. 3.6 and the rate constants in Tables 3.2 and 3.3. For example, while $k_{2\rightarrow3}$, the propynyl isomerization rate constant, is much greater than $k_{2\rightarrow6}$ at 248 nm, $k_{2\rightarrow6}$ is larger at 193 nm. This result exemplifies the well-known dependence of RRKM rates via loose and tight transition state on the available energy; at low energy, only the tight **TS 2** is energetically accessible, but at higher energy, dissociation over the loose **TS 6** wins out owing to the larger number of available states at the TS. Similar considerations explain why D_2 loss is less prevalent than C-C bond cleavage at 193 nm.

A more detailed picture of the dynamics at 193 nm is given in Fig. 3.6, which shows that propynyl undergoes some isomerization to propargyl, thereby producing some channel **7** and **8**, but that direct C-C bond cleavage to channel **6** is considerably faster than isomerization. In contrast, propargyl undergoes relatively little isomerization at 193 nm, and this is reflected in the branching ratios for the C-C bond cleavage channels. As a result, the overall dynamics at 193 nm depend strongly on whether propynyl or propargyl is photoexcited, in sharp contrast to the results at 248 nm.

3. 5 Conclusions

We have investigated the minima, transition states, and isomerization/dissociation pathways for the C_3D_3 radical using electronic structure calculations. These calculations were complemented by calculations of RRKM rate constants and branching ratios in order to investigate the interplay between dissociation and isomerization of photoexcited propargyl and propynyl radicals. Previous experimental and theoretical results have indicated that the dissociation of both radicals occurs on this ground state surface, rather than an electronically excited surface.

Our comprehensive survey of the C_3D_3 potential energy surface enabled us to map out all reaction channels observed in the fast beam photodissociation experiment[21] at 248 and 193 nm. We found a direct cleavage channel leading to CD_2+C_2D, which had not been mentioned in earlier theoretical studies,[52-54] and re-analysis of our experimental results indicated that this channel was present in several data sets.

The calculated kinetics and branching ratios show that propargyl and propynyl represent a classic system in which a low-energy channel involving a rearrangement, namely the isomerization of propynyl to **3** and propargyl radical, competes with higher energy bond cleavage channels. At the lower excitation energy used in this experiment, 248 nm, our analysis indicates that propynyl rapidly isomerizes to the more stable propargyl isomer. As result, the overall dissociation dynamics for propargyl and propynyl are similar, with D_2 loss dominating over the higher energy C-C bond cleavage channels. On the other hand, at 193 nm, there are significant differences seen in the experimental branching ratios, with CD + C_2D_2 and C_2+CD_3 being the prevalent C-C bond cleavage channels for propargyl and propynyl, respectively, while considerably less D_2 loss occurs from both radicals. These differences are reproduced in our analysis and arise because high-energy C-C bond cleavage channels involving loose transition states compete much more effectively with isomerization at the higher excitation energy. Hence, while both propynyl and, to a lesser extent, propargyl, undergo some isomerization at 193 nm, direct dissociation is far more important.

Acknowledgments

This work was supported by the Director, Office of Basic Energy Sciences, Chemical Sciences Division of the U.S. Department of Energy under Contract No. DE-AC02-05CH11231. L. C. gratefully acknowledges the Swiss National Science Foundation for a postdoctoral fellowship.

Supporting Information Available. PES map, coordinates, electronic energies and vibrational frequencies of all stationary points on the C_3H_3 potential energy surface.

References

1 C. H. Wu and R. D. Kern, *J. Phys. Chem.*, 1987, **91**, 6291.

2 I. Cherchneff and J. R. Barker, *Astrophys. J.*, 1992, **394**, 703.

3 I. Cherchneff, J. R. Barker and A. Tielens, *Astrophys. J.*, 1992, **401**, 269.

4 C. L. Morter, S. K. Farhat, J. D. Adamson, G. P. Glass and R. F. Curl, *J. Phys. Chem.*, 1994, **98**, 7029.

5 C. Ochsenfeld, R. I. Kaiser, Y. T. Lee, A. G. Suits and M. HeadGordon, *J. Chem. Phys.*, 1997, **106**, 4141.

6 R. I. Kaiser, *Chem. Rev.*, 2002, **102**, 1309.

7 R. I. Kaiser and A. M. Mebel, *Int. Rev. Phys. Chem.*, 2002, **21**, 307.

8 J. A. Miller and S. J. Klippenstein, *J. Phys. Chem. A*, 2003, **107**, 7783.

9 B. R. Giri, H. Hippler, M. Olzmann and A. N. Unterreiner, *Phys. Chem. Chem. Phys.*, 2003, **5**, 4641.

10 E. H. Wilson, S. K. Atreya and A. Coustenis, *Journal of Geophysical Research-Planets*, 2003, **108**.

11 S. K. Atreya, *Science*, 2007, **316**, 843.

12 Y. Georgievskii, J. A. Miller and S. J. Klippenstein, *Phys. Chem. Chem. Phys.*, 2007, **9**, 4259.

13 J. A. Miller and C. F. Melius, *Combust. Flame*, 1992, **91**, 21.

14 J. A. Miller, 26th Symp. (Int.) Combust., 1996.

15 P. Howe and A. Fahr, *J. Phys. Chem. A*, 2003, **107**, 9603.

16 J. A. Miller, R. J. Kee and C. K. Westbrook, *Annu. Rev. Phys. Chem.*, 1990, **41**, 345.

17 K. M. Leung and R. P. Lindstedt, *Combust. Flame*, 1995, **102**, 129.

18 N. M. Marinov, M. J. Castaldi, C. F. Melius and W. Tsang, *Combust. Sci. Technol.*, 1997, **128**, 295.

19 J. D. DeSain and C. A. Taatjes, *J. Phys. Chem. A*, 2003, **107**, 4843.

20 S. E. Wheeler, K. A. Robertson, W. D. Allen, H. F. Schaefer, Y. J. Bomble and J. F. Stanton, *J. Phys. Chem. A*, 2007, **111**, 3819.

21 P. E. Crider, L. Castiglioni, K. E. Kautzman and D. M. Neumark, *J. Chem. Phys.*, 2009, **130**, 044310.

22 K. Tanaka, Y. Sumiyoshi, Y. Ohshima, Y. Endo and K. Kawaguchi, *J. Chem. Phys.*, 1997, **107**, 2728.

23 K. Tanaka, T. Harada, K. Sakaguchi, K. Harada and T. Tanaka, *J. Chem. Phys.*, 1995, **103**, 6450.

24 L. Yuan, J. DeSain and R. F. Curl, *J. Mol. Spectrosc.*, 1998, **187**, 102.

25 J. M. Oakes and G. B. Ellison, *J. Am. Chem. Soc.*, 1983, **105**, 2969.

26 M. S. Robinson, M. L. Polak, V. M. Bierbaum, C. H. Depuy and W. C. Lineberger, *J. Am. Chem. Soc.*, 1995, **117**, 6766.

27 R. K. Sreeruttun, P. Ramasami, G. Yan, C. S. Wannere, P. V. Schleyer and H. F. Schaefer, *Int. J. Mass. Spectrom.*, 2005, **241**, 295.

28 F. P. Lossing, *Can. J. Chem.*, 1972, **50**, 3973.

29 D. W. Minsek and P. Chen, *J. Phys. Chem.*, 1990, **94**, 8399.

30 D. A. Ramsay and Thistlet.P, *Can. J. Phys.*, 1966, **44**, 1381.

[31] A. Fahr, P. Hassanzadeh, B. Laszlo and R. E. Huie, *Chem. Phys.*, 1997, **215**, 59.
[32] A. Fahr and A. H. Laufer, *J. Phys. Chem. A*, 2005, **109**, 2534.
[33] R. H. Qadiri, E. J. Feltham, N. H. Nahler, R. P. Garcia and M. N. R. Ashfold, *J. Chem. Phys.*, 2003, **119**, 12842.
[34] J. C. Robinson, N. E. Sveum, S. J. Goncher and D. M. Neumark, *Mol. Phys.*, 2005, **103**, 1765.
[35] J. Zhou, E. Garand, W. Eisfeld and D. M. Neumark, *J. Chem. Phys.*, 2007, **127**.
[36] W. M. Jackson, D. S. Anex, R. E. Continetti, B. A. Balko and Y. T. Lee, *J. Chem. Phys.*, 1991, **95**, 7327.
[37] H. J. Deyerl, I. Fischer and P. Chen, *J. Chem. Phys.*, 1999, **111**, 3441.
[38] S. J. Goncher, D. T. Moore, N. E. Sveum and D. M. Neumark, *J. Chem. Phys.*, 2008, **128**.
[39] L. R. McCunn, B. L. FitzPatrick, M. J. Krisch, L. J. Butler, C. W. Liang and J. J. Lin, *J. Chem. Phys.*, 2006, **125**.
[40] X. Zheng, Y. Song and J. Zhang, *J. Phys. Chem. A*, 2009, **113**, 4604.
[41] H. Honjou, M. Yoshimine and J. Pacansky, *J. Phys. Chem.*, 1987, **91**, 4455.
[42] X. Krokidis, N. W. Moriarty, W. A. Lester and M. Frenklach, *Chem. Phys. Lett.*, 1999, **314**, 534.
[43] J. Vazquez, E. M. Harding, J. Gauss and J. F. Stanton, *J. Phys. Chem. A*, 2009, **113**, 12447.
[44] J. A. W. Harkless and W. A. Lester, *J. Chem. Phys.*, 2000, **113**, 2680.
[45] P. Botschwina, R. Oswald, J. Flugge and M. Horn, *Z. Phys. Chem.*, 1995, **188**, 29.
[46] S. Ikuta, *J. Mol. Struct. (Theochem)*, 1998, **434**, 121.
[47] B. S. Jursic, *J. Mol .Struct. (Theochem)*, 2000, **505**, 233.
[48] W. Eisfeld, *Phys. Chem. Chem. Phys.*, 2005, **7**, 3924.
[49] W. Eisfeld, *J. Phys. Chem. A*, 2006, **110**, 3903.
[50] B. N. Papas, M. S. Schuurman and D. R. Yarkony, *J. Chem. Phys.*, 2008, **129**, 124104.
[51] B. N. Papas, M. S. Schuurman and D. R. Yarkony, *J. Chem. Phys.*, 2009, **130**, 064306.
[52] A. M. Mebel, W. M. Jackson, A. H. H. Chang and S. H. Lin, *J. Am. Chem. Soc.*, 1998, **120**, 5751.
[53] T. L. Nguyen, A. M. Mebel and R. I. Kaiser, *J. Phys. Chem. A*, 2001, **105**, 3284.
[54] T. L. Nguyen, A. M. Mebel, S. H. Lin and R. I. Kaiser, *J. Phys. Chem. A*, 2001, **105**, 11549.
[55] R. E. Continetti, D. R. Cyr, D. L. Osborn, D. J. Leahy and D. M. Neumark, *J. Chem. Phys.*, 1993, **99**, 2616.
[56] E. F. C. Byrd, D. Sherrill and M. Head-Gordon, *J. Phys. Chem. A*, 2001, **105**, 9736.
[57] S. H. Kyne, C. H. Schiesser and H. Matsubara, *J. Org. Chem.*, 2008, **73**, 427.

58 D. Becke, *Phys. Rev. A*, 1988, **38**, 3098.
59 T. H. Dunning Jr, *J. Chem. Phys.*, 1989, **90**, 1007.
60 C. Lee, W. Yang and R. G. Parr, *Phys. Rev. B*, 1988, **37**, 785.
61 B. Miehlich, A. Savin, H. Stoll and H. Preuss, *Chem. Phys. Lett.*, 1989, **157**, 200.
62 K. A. Peterson, D. E. Woon and D. H. Dunning Jr, *J. Chem. Phys.*, 1994, **100**, 7410.
63 D. Feller, *J. Chem. Phys.*, 1992, **96**, 6104.
64 D. Feller and K. A. Peterson, *J. Chem. Phys.*, 1998, **108**, 154.
65 H.-J. Werner, P. J. Knowles, R. Lindh, et al., MOLPRO, a package of ab initio programs, 2003.
66 M. S. Gordon and M. W. Schmidt, in *Theory and Applications of Computational Chemistry: the first forty years*, ed. C. E. Dykstra, G. Frenking, K. S. Kim and G. S. Scuseria, Elsevier, Amsterdam, 2005.
67 M. J. Frisch, G. W. Trucks, H. B. Schlegel, et al., Gaussian 03, Revision C.02, 2004.
68 R. A. Marcus and O. K. Rice, *J. Phys. Colloid Chem.*, 1951, **55**, 894.
69 K. J. Laidler, *Chemical Kinetics*, Harper & Row, New York, 1987.
70 E. Pollak and P. Pechukas, *J. Am. Chem. Soc.*, 1978, **100**.
71 T. Beyer and D. F. Swinehart, *Communications of the ACM*, 1973, **16**, 379.
72 W. L. Hase and L. Zhu, A General RRKM Program, in *Quantum Chemistry Program Exchange*, 1994, vol. 14.
73 J. I. Steinfeld, J. S. Francisco and W. L. Hase, *Chemical Kinetics and Dynamics*, Prentice-Hall, Upper Saddle River, NJ, 1999.
74 M. E. Jacox, in *NIST Chemistry WebBook, Standard Reference Database Number 69*, ed. P. J. Linstrom and W. G. Mallard, National Institute of Standards and Technology, Gaithersburg, MD, 2005.
75 S. M. Sheehan, B. F. Parsons, J. Zhou, E. Garand, T. A. Yen, D. T. Moore and D. M. Neumark, *J. Chem. Phys.*, 2008, **128**, 034301.

Chapter 4

Two- and three-body photodissociation dynamics of diiodobromide (I_2Br^-) anion

The contents of this chapter have been submitted for publication in J. Chem Phys. (in press).

The photodissociation of gas-phase I_2Br^- was investigated using fast beam photofragment translational spectroscopy. Anions were photodissociated from 300 to 270 nm (4.13 - 4.59 eV) and the recoiling photofragments were detected in coincidence by a time- and position-sensitive detector. Both two- and three-body channels were observed throughout the energy range probed. Analysis of the two-body dissociation showed evidence for four distinct channels: $Br^- + I_2$, $I^- + IBr$, $Br + I_2^-$, and $I + IBr^-$. In three-body dissociation, $Br(^2P_{3/2}) + I(^2P_{3/2}) + I^-$ and $Br^- + I(^2P_{3/2}) + I(^2P_{3/2})$ are produced primarily from a concerted decay mechanism. A sequential decay mechanism was also observed and attributed to $Br^-(^1S) + I_2(B^3\Pi_{0u}^+)$ followed by predissociation of $I_2(B)$.

4. 1 Introduction

Over the last two decades, trihalide anions have attracted interest as model systems for studying fundamental physical processes in chemical reaction dynamics. The trihalides are important model systems for understanding chemical bond formation.[1] I_3^-, the most well-known trihalide, has received special interest as it readily produces the I_2^- ion upon photolysis in solution-phase chemistry.[2-4] Trihalide ion formation by the freezing of sea salt components has been proposed as a possible source of ozone depletion in polar atmospheres.[5,6] I_3^- is also well-known as a redox mediator in dye-sensitized solar cells.[7] The ultraviolet photodissociation dynamics of I_3^- have been investigated in solution and in the gas phase. Time-resolved experiments in both media showed vibrational coherences in the I_2^- product, but with considerably higher excitation in the gas phase.[8-10] Gas phase experiments have also sought to describe the energetics[11,12] and primary photochemistry of I_3^- with emphasis on elucidating the branching ratios among the available two- and three-body product channels.[13-16] In this paper, the photodissociation dynamics of I_2Br^-, which is isovalent to I_3^- but non-centrosymmetric, are investigated with the goal of understanding how the two- and three-body dissociation dynamics change as the symmetry is broken.

In contrast to I_3^-, heteronuclear trihalides are relatively unexplored. These species are linear, and exemplify the important trend that the least electronegative atom occupies the center position in the triatomic molecule.[17,18] In early theoretical work, Wiebenga *et al.*[19] calculated bond orders and heats of formation for various trihalides. Landrum *et al.*[20] performed DFT calculations on I_2X^- species and found, as expected, that linear structures with the least electronegative atom (i.e., an I atom) in the center were more stable than other arrangements, because there is more negative charge on the outer atoms. Ogawa *et al.*[21] carried out electronic structure calculations to determine structure and dissociation energies of heteronuclear trihalides in the gas phase and in solution. Sanov *et al.*[22] performed DFT calculations at the *m*PW1PW level to determine the structure and dissociation energies of $BrICl^-$ and IBr_2^-, finding that linear structures with the I atom in the center were more stable by around 0.5 eV.

Solution-phase absorption spectra for various trihalides have been analyzed,[23,24] as well as Raman and infrared spectra.[25] Popov *et al.*[24] found two broad absorption maxima for I_2Br^- in acetonitrile at 351 and 280 nm, analogous to the two bands in the I_3^- absorption spectrum at 360 and 290 nm.[3] Later, Eyal *et al.*[26] found the maximum of the upper band of I_2Br^- to be 270 nm. Gershgoren *et al.*[9] determined that breaking centrosymmetry in the trihalide enhanced vibrational coherence in the I_2^- product by analyzing the transient absorption spectra of I_2Br^- compared to that of I_3^-.

In the gas phase, Sanov *et al.*[22] performed femtosecond pump-probe experiments to study the time-resolved photodissociation dynamics of $BrICl^-$ and IBr_2^- around 400 nm (3.0 - 3.5 eV). For $BrICl^-$, only IBr^- and ICl^- fragments were detected, while only IBr^- fragments were detected for IBr_2^-, suggesting that their ion source produced only the most stable isomer in which the I atom occupies the center position. They detected vibrational coherence in IBr^- and ICl^- photofragments, with higher average vibrational excitation than in I_3^-, consistent with Gershgoren's condensed phase results for I_2Br^-. Mabbs *et al.*[27] used femtosecond anion photoelectron spectroscopy to investigate the I^- channel in the 388 nm (3.2 eV) photodissociation of I_2Br^-, observing the time-resolved evolution of the excess-electron wave function from the I_2Br^- molecular orbital to the atomic orbital of I^-. In addition, they established a lower bound of 4.0 eV for the electron affinity (EA) of neutral I_2Br. Crawford *et al.*[28] have investigated the collision-induced dissociation of I_2Br^-, finding approximately equal yields of I^- and Br^- over a collision energy range of 20-50 eV.

In this paper, we report results from experiments on I_2Br^- photodissociation from the upper absorption band using fast beam photofragment translational spectroscopy. Our experiments characterize both two-body and three-body dissociation channels. These experiments provide a basis for comparison of the photodissociation dynamics of the extensively studied triiodide anion and a non-centrosymmetric analog. Our two-body photofragment translational energy distributions [$P(E_T)$ distributions] suggest that I_2, I_2^-, IBr, and IBr^- are formed in highly vibrationally excited states, in accordance with other trihalides.[8-10,13-16,22,29-34] We obtain bond dissociation energies and the heat of formation of I_2Br^- from our three-body $P(E_T)$ distributions, and extract detailed information on the three-body dissociation mechanism by means of Dalitz plots.[35]

4. 2 Experiment

The photodissociation experiments were performed on our fast beam photofragment translational spectrometer. This apparatus has been described in detail previously.[36-38] I_2Br^- ions were produced by flowing 5% methyl bromide (Sigma, 95%) in Ar (~20 psi) over IBr crystals (Sigma, 98%) at room temperature. The carrier gas with precursor was supersonically expanded through a piezoelectric valve pulsed at 60 Hz. The gas expansion occurred across a pulsed discharge (~0.5 kV) and was intersected with a 1 keV electron beam generated by an electron gun.[28] The resulting anions were accelerated to a laboratory-frame beam energy of 8 keV and mass-selected using a Bakker time-of-flight mass spectrometer.[39,40] The two isotopes of bromine occur in approximately equal abundance and the $I_2{}^{79}Br^-$ (333 amu) isotopolog was chosen for the experiments reported here.

After exiting the source region, the ion packet intersected a laser pulse from a XeCl excimer-pumped (Lambda Physik LPX 210, 308 nm) tunable dye laser (Lambda Physik FL 3002). The wavelengths used in this experiment ranged from 300 – 270 nm (4.13 – 4.59 eV) Recoiling photofragments were detected 2.15 m downstream of the dissociation region by a time- and position-sensitive (TPS) coincidence imaging detector based on the design by Zajfman *et al.*[41] Undissociated parent ions and intact photodetached neutrals were blocked by a 5 mm diameter beam block positioned before the detector. The current set-up is capable of detecting both anions and neutral photofragments that have cleared the beam block.

The TPS detector consisted of three 75 mm diameter imaging quality microchannel plates (MCPs) arranged in a Z-stack configuration and coupled to a phosphor screen. Spots appearing on the phosphor screen corresponded to the impinging photofragments; the resulting image was split by a dichroic beam splitter with a 4x4 multianode PMT array detecting the reflected fraction and a charge-coupled device (CCD) camera detecting the transmitted fraction via an image intensifier. Arrival times measured by the PMT array were correlated with fragment positions acquired by the CCD camera. Coincidence was ensured by accepting only events occurring in the same time window where the rough position information obtained from the PMT array concurred with the accurate position information obtained from the CCD camera.

The coincidence arrival times and positions were used to infer the masses and the center-of-mass (COM) translational energy release of the photofragments for each photodissociation event. In two-body dissociation events, the angle of recoil θ was also obtained. In three-body events, the COM momenta of all three fragments were determined. This information was used to construct COM $P(E_T)$ distributions and, for three-body events, Dalitz plots[35] describing the momentum partitioning among the fragments. Owing to the presence of the beam block and the finite diameter of the detector, detection efficiency was limited for events of certain recoil geometry. These considerations were accounted for by normalizing the raw $P(E_T)$ distributions with a detector acceptance function (DAF).[42] In the work presented here, only two-body events were DAF-corrected; three-body events are presented as raw $P(E_T)$ distributions. In the absence of a DAF, the three-body $P(E_T)$ distributions are expected to be biased toward high E_T events.

4. 3 Theoretical methods

Ab initio calculations of dissociation energies of $IIBr^-$ and $IBrI^-$ were performed using coupled-cluster theory with single and double excitations and treating triple excitations perturbatively [CCSD(T)]. The aug-cc-PVnZ-PP bases[43] were used for n =4, 5. In addition to including diffuse and polarization functions, these basis sets employ a pseudopotential to account for the relativistic core electrons of these heavy atoms and treat only the valence and semi-core electrons explicitly. The small core includes the 1s, 2s, and 2p electrons ([Ne] core) for bromine and the [Ar] core + 3d electrons for iodine, leaving 25 electrons (26 for I^- and Br^-) for the SCF calculation. Using these correlation-consistent basis sets provides an avenue for extrapolation to the complete basis set (CBS) limit given by[43]

$$E(n) = E_{CBS} + a/n^3 \quad (n = 4,5) \tag{4.1}$$

where n represents the cardinal number of the basis set. For each CBS extrapolation, the optimized geometry from the n=4 basis set was used for the calculation of the energetics at n=5. Lastly, the strong spin-orbit interaction in systems containing heavy atoms must be properly accounted for to obtain reliable results. Here, this problem was largely avoided as all the calculations performed corresponded to closed shell atoms and molecules. A summary of the results of these calculations is presented in Table 4.1.

As a benchmark system, calculations were initially performed on the well-characterized I_3^- anion. To determine the dissociation energy, the total electronic energy of I_3^- was subtracted from the sum of the energies of the I^- and I_2 fragments. This computed dissociation energy of 1.349 eV is in remarkable agreement with the experimental value of 1.31 eV.[11] Some of the discrepancy is certainly due to the neglect of the zero point energy corrections in all of the calculations. However, this correction is expected to be small (~100 cm^{-1}) in all the molecules because of the relatively weak bonds and large masses of the constituent atoms.

This methodology was then applied to the two isomers of I_2Br^-. For isomer 1 ($IIBr^-$), these calculations predict nearly identical values of 1.42 and 1.43 eV for dissociation into $Br^- + I_2$ and $I^- + IBr$, respectively. Isomer 2, $IBrI^-$, was found to lie 0.35 eV above $IIBr^-$, in accordance with the general rule for trihalide structures. This energy difference was reflected in the lower dissociation energy of isomer 2 of approximately 1.08 eV. All calculations were carried out using the Molpro 2009 suite of programs.[44]

From either $D_0(I_2\text{-}Br^-)$ or $D_0(BrI\text{-}I^-)$, one can derive the energetics of all possible two- and three-body dissociation channels from I_2Br^-. These are listed in Table 4.2. Note that the values for channel 1A, $Br^-(^1S) + I_2(X\,^1\Sigma_g^+)$, and channel 2A, $I^-(^1S) + IBr(X\,^1\Sigma^+)$, upon which all the other energies are based, are very close to the calculated values of D_e in Table 4.1 but were actually determined from this experiment, as discussed in Section 4.5. The other dissociation energies were then determined by combining these energies with previously established experimental

Table 1 Calculated bond dissociation energies and equilibrium bond lengths for I_3^-, $IIBr^-$, and $IBrI^-$. The energy difference between $IIBr^-$ and $IBrI^-$ is also included. Energies are given in eV and bond lengths are given in Å.

Basis Set	$D_e(I_2\text{-}I^-)$	$r(I_3^-)$	$D_e(I_2\text{-}Br^-)$	$D_e(BrI\text{-}I^-)$	$r(I\text{-}IBr^-)$	$r(II\text{-}Br^-)$	$D_e(IBr\text{-}I^-)$	$r(IBrI^-)$	ΔE
aug-cc-pVQZ-PP	1.331	2.953	1.449	1.457	2.936	2.748	1.079	2.780	0.378
aug-cc-pV5Z-PP	1.339	2.953	1.435	1.443	2.936	2.748	1.081	2.780	0.362
CBS	1.349		1.420	1.429			1.083		0.346

Table 4.2 List of product channels organized by fragment masses in amu. Dissociation energies for each channel are given in eV.

	Mass channel (amu)	Product channel	D_0 (eV)	Equation label
$I_2Br^- \rightarrow$	79 + 254	$Br^-(^1S) + I_2(X^1\Sigma_g^+)$	1.44	**1A**
		$Br(^2P_{3/2}) + I_2^-(X^2\Sigma_u^+)$	2.28	**1B**
		$Br^*(^2P_{1/2}) + I_2^-(X^2\Sigma_u^+)$	2.74	**1C**
		$Br^-(^1S) + I_2(A^3\Pi_{1u})$	2.79	**1D**
		$Br^-(^1S) + I_2(B^3\Pi_{0u}^+)$	3.39	**1E**
	127 + 206	$I^-(^1S) + IBr(X^1\Sigma^+)$	1.47	**2A**
		$I(^2P_{3/2}) + IBr^-(X^2\Sigma_{1/2}^+)$	2.02	**2B**
		$I^-(^1S) + IBr(A'^3\Pi_2)$	2.88	**2C**
		$I^*(^2P_{1/2}) + IBr^-(X^2\Sigma_{1/2}^+)$	2.96	**2D**
		$I^-(^1S) + IBr(A^3\Pi_1)$	2.99	**2E**
		$I^-(^1S) + IBr(B^3\Pi_0^+)$	3.47	**2F**
	79 + 127 + 127	$Br^-(^1S) + I(^2P_{3/2}) + I(^2P_{3/2})$	2.98	**3A**
		$Br(^2P_{3/2}) + I^-(^1S) + I(^2P_{3/2})$	3.29	**3B**
		$Br^*(^2P_{1/2}) + I^-(^1S) + I(^2P_{3/2})$	3.74	**3C**
		$Br^-(^1S) + I^*(^2P_{1/2}) + I(^2P_{3/2})$	3.92	**3D**

values for the spin-orbit coupling constants for iodine and bromine, the dissociation energies of I_2,[45] I_2^-,[46] IBr,[47] and IBr^-,[48] the electron affinities of Br, I, and I_2,[49] and the term energies of the A and B states of I_2 [50,51] and IBr.[52-55]

4. 4 Experimental results

The photodissociation of I_2Br^- was investigated at photon energies between 4.13 and 4.59 eV (300 – 270 nm), all of which lie within its upper absorption band.[24] Photofragment mass ratios were determined to identify the product channels. Figure 4.1a plots photofragment mass ratio distributions as a function of photon energy and normalized by area. Three mass ratios were observed in the two-body data, corresponding to three distinct two-body mass channels; these were 0.31:1, 0.62:1, and 1:1. One three-body mass channel was also observed. Figure 4.1b is a sample plot (hν = 4.28 eV) of the photofragment mass distribution for this channel,

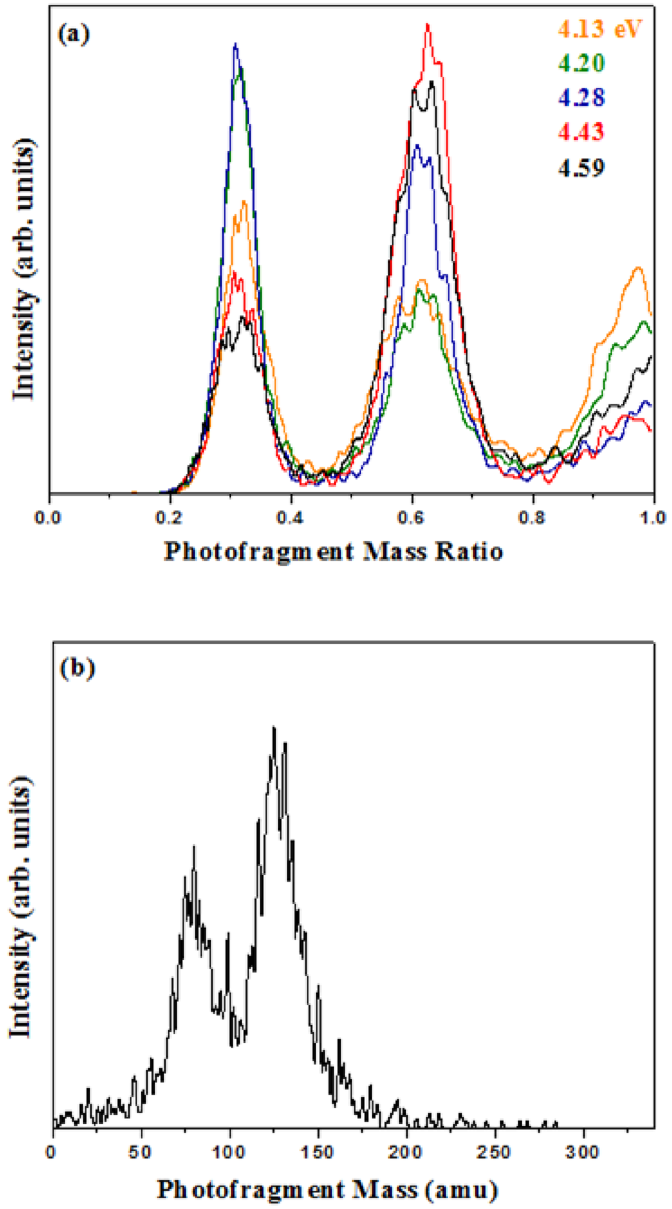

Figure 4.1 (a) Photofragment mass ratio of two-fragment valid events following excitation of I_2Br^- at photon energies of 4.13 - 4.59 eV and (b) three-body photofragment mass distribution following excitation at hv = 4.28 eV.

with a feature at 79 amu and one at 127 amu with about twice the intensity, corresponding to one bromine and two iodine fragments, respectively.

Figure 4.1 shows that four product mass channels result from the dissociation of I_2Br^-: channel 1, with mass ratio 0.31:1, corresponding to $Br^- + I_2$ or $Br + I_2^-$, channel 2, with mass ratio 0.62:1, corresponding to $I^- + IBr$ or $I + IBr^-$, channel 3, corresponding to three-body dissociation as determined by the coincident detection of three fragments, and channel 4, corresponding to three-body dissociation where two fragments with a 1:1 mass ratio are detected, suggesting events in which the bromine fragment is blocked and two iodine fragments strike the detector. A fifth possibility, where an iodine fragment is blocked and a bromine fragment and iodine fragment are detected, is indistinguishable from channel 2 because the mass ratios are equivalent in the resolution of the experiment, although there is evidence for this process from the $P(E_T)$ distributions as discussed in Section 4.5. Note that "fragment" refers universally to charged and neutral species; for example, "iodine fragment" indicates only a fragment of mass 127 amu, regardless of charge.

Figures 4.2 and 4.3 show two-body photofragment $P(E_T)$ distributions for mass channels 1 and 2, respectively. In each of these figures, the $P(E_T)$ distributions observed from all five photon energies are presented. Each $P(E_T)$ distribution has been shifted to higher kinetic energy by $\Delta E_{h\nu}$, defined as the difference in energy between the dissociation photon and a 4.59 eV photon (the highest energy photon used). In this scheme, features corresponding to the same fragment internal energy line up vertically, thereby facilitating peak assignments. The scaled energy axis in Figure 4.3b is discussed in Section 4.5. Figures 4.2 and 4.3 also show brackets labeled with possible product channels that indicate the range of E_T possible for each channel, from $E_T^{\min}$ to $E_T^{\max}$. $E_T^{\max}$ values are determined from the dissociation

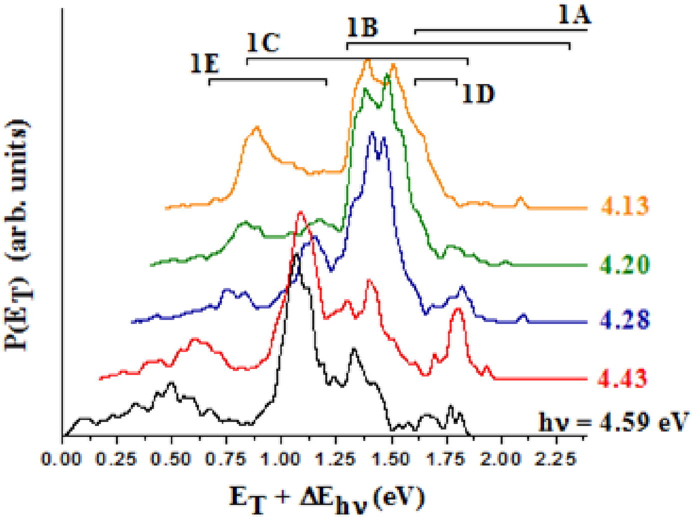

Figure 4.2 Photofragment translational energy distributions for two-body dissociation of I_2Br^- into 79 and 254 amu fragments. $P(E_T)$ distributions are shifted to higher E_T by 4.59 eV - hv. The allowed translational energies for channels 1A - 1E are bracketed.

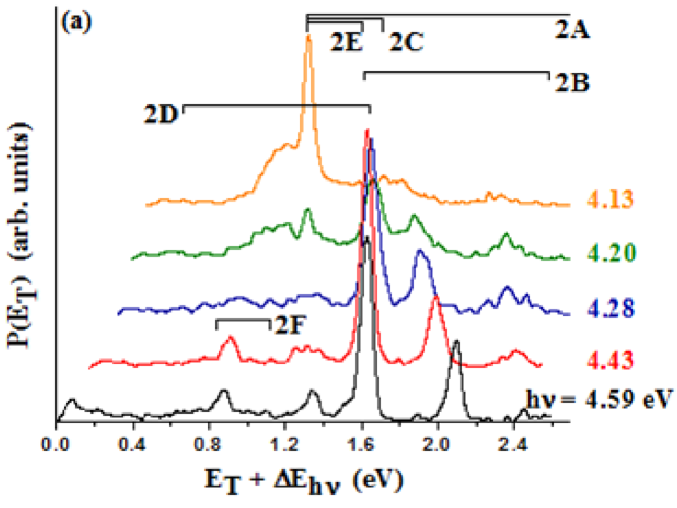

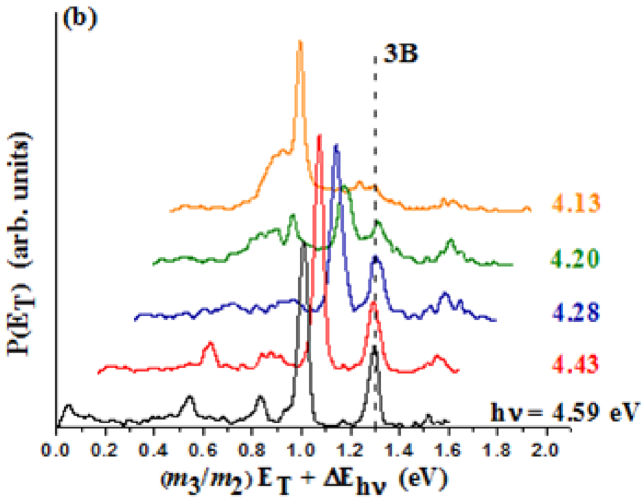

Figure 4.3 (a) Photofragment translational energy distributions for two-body dissociation of I_2Br^- into 127 and 206 amu fragments. $P(E_T)$ distributions are shifted to higher E_T by 4.59 eV - hν. The allowed translational energies for channels 2A - 2F are bracketed. (b) $P(E_T)$ distributions scaled by mass ratio of IBr to IIBr (see text) and shifted by 4.59 eV - hν. The dotted line is drawn at the expected E_T for channel 3B.

values given in Table 4.2. $E_T^{\min}$ values are determined from the well depth of the diatomic product, corresponding to the maximum possible internal excitation, beyond which three-body dissociation occurs. In both figures, qualitative changes are evident in the features of the $P(E_T)$ distributions as photon energy increases, indicating different pathways become populated.

We also determine anisotropy parameters,[56] [$\beta(E_T)$], for each two-body mass channel. These distributions are determined by fitting the DAF-corrected $P(E_T,\theta)$ distribution to the equation:

$$P(E_T,\theta) = P(E_T)[1+\beta(E_T)P_2(\cos\theta)] \tag{4.2}$$

where θ is the angle between the electric field vector of the laser pulse and the recoil vector of the photofragments and $P_2(\cos\theta)$ is the second Legendre polynomial. $\beta(E_T)$ ranges from -1, indicating a $\sin^2\theta$ distribution, to 2 for a $\cos^2\theta$ distribution. Values of $\beta(E_T)$ vary significantly with translational energy and are discussed in more detail below. In most cases, $\beta(E_T)$ is nonzero, indicating an anisotropic angular distribution.

In Figure 4.4, the raw (not DAF-corrected) $P(E_T)$ distributions for three-body dissociation are presented. Because I_2Br^- is a triatomic molecule, all available energy must be deposited in translation or electronic excitation. The dashed vertical lines indicate where each product channel should fall based on the experimentally derived values listed in Table 4.2, assuming no internal energy in the anion and no other broadening. Features in common appear at successively higher E_T as the photon energy is increased, reflecting the additional energy available for translation.

Dalitz plots[35,57,58] showing momentum partitioning among fragments for three-body dissociation are presented in Figures 4.5 and 4.6, for peaks 3A and 3B, respectively. Each point in the plot corresponds to a three-body event and is constrained by conservation of energy to fall within the equilateral triangle and by conservation of momentum to fall within an inscribed circle. Each side of the triangle is an axis corresponding to the fraction of the square of the momentum, $f_i = p_i^2/\Sigma p_j^2$, of one fragment. In each plot in Figures 4.5 and 4.6, the lower axis corresponds to the squared-momentum contribution of the bromine fragment, and the other two axes correspond to the iodine fragments. Because the two iodine fragments are indistinguishable in our detection scheme, the momentum partitioning exhibits two-fold symmetry and can thus be plotted in half the area of the Dalitz circle. As the events are plotted here, I and I' correspond to the faster and slower iodine fragments, respectively.

4. 5 Analysis

At every wavelength studied, both two-body mass channels are in evidence. The accessible energy ranges for the various product channels overlap as indicated by the brackets in Figures 4.2 and 4.3. As a result, assignments of features in the $P(E_T)$ distributions to specific channels can be ambiguous. We generally favor assignments in which the feature in question falls off sharply near either $E_T^{\max}$ or $E_T^{\min}$ for a particular channel, especially if this falloff is observed at multiple photon energies. In cases where a two-body channel falls off at $E_T^{\min}$, one expects to observe the corresponding three-body channel from dissociation of the diatomic fragment, so the presence or absence of a three-body channel can help assign the two-body feature.

4.5.1 Two-body dissociation: Br + I_2 fragments

In Figure 4.2, the *P(E* distributions for mass channel 1 ($\mathrm{Br}^- + \mathrm{I}_2$ or $\mathrm{Br} + \mathrm{I}_2^-$) are plotted against $E_T + \Delta E_{h\nu}$. Beginning at 4.13 eV, two broad features are apparent. The most prominent feature extends from ~1.25 to ~1.60 eV. This feature lies within the energetic limits of channels 1B, $\mathrm{Br}(^2P_{3/2}) + \mathrm{I}_2^-(X\,^2\Sigma_u^+)$, and 1C, $\mathrm{Br}^*(^2P_{1/2}) + \mathrm{I}_2^-(X\,^2\Sigma_u^+)$. However, since it drops off abruptly below $E_T^{\min}$ for channel 1B, $\mathrm{Br}(^2P_{3/2}) + \mathrm{I}_2^-(X\,^2\Sigma_u^+)$, we favor its assignment to this channel. This feature peaks near $E_T^{\min}$ of channel 1B, indicating the I_2^- fragment is produced in a vibrationally excited state near the dissociation asymptote. The anisotropy parameter was measured to be $\beta(E_T) = 0.78 \pm 0.1$ indicating a mostly parallel transition. A similar feature is observed at each photon energy, though it is diminished at 4.43 and 4.59 eV. $\beta(E_T)$ does not change with photon energy, suggesting the same transition is responsible at all wavelengths.

The second feature observed at 4.13 eV peaks near $E_T + \Delta E_{h\nu} \approx 0.85$ eV. This feature falls within the range of channel 1E, $\mathrm{Br}^-(^1S) + \mathrm{I}_2(B\,^3\Pi_{0u}^+)$, although the high E_T portion of the feature also falls within the range of channel 1C. The anisotropy parameter was measured to be $\beta(E_T) = 0.00 \pm 0.1$ averaged over the feature, but an abrupt decrease in the anisotropy parameter to about -0.5 is observed near $E_T^{\min}$ for channel 1C, so dissociation may occur via both channels. On the other hand, intensity at $E_T^{\min}$ for channel 1C should correlate with channel 3C, but there is no evidence for this channel at this wavelength. We assign the feature to channel 1E on account of intensity below $E_T^{\min}$ for channel 1C, but some signal at higher E_T may be from channel 1C. For either channel, the diatomic fragment must be highly excited since the intensity is greatest near $E_T^{\min}$ for the two channels. A similar feature is observed at 4.20 and 4.28 eV, with a similar, though less clear, change in $\beta(E_T)$.

Moving to the $P(E_T)$ distribution at 4.28 eV, a feature is evident between 1.00 and 1.25 eV. A similar feature is observed with greater intensity at 4.43 and 4.59 eV. This feature falls within the energy ranges of channels 1C and 1E, and occurs just below $E_T^{\max}$ of channel 1E. While both pathways may contribute, the sharp decrease in intensity above $E_T^{\max}$ for channel 1E suggests assignment to that channel. This assignment is corroborated by evidence for predissociation of

$I_2(B^3\Pi_{0u}^+)$ presented below in our discussion of three-body dynamics. Peaking near $E_T^{\max}$ indicates the electronically excited $I_2(B)$ fragments are produced with little internal excitation, in contrast to the vibrationally excited diatomic fragments associated with the other features. The anisotropy parameter was observed to be $\beta(E_T) = 0.55 \pm 0.12$, indicating a mostly parallel transition.

Another feature appears in the 4.28 eV $P(E_T)$ distribution near $E_T + \Delta E_{h\nu} \approx$ 1.8 eV and becomes more intense at 4.43 eV. This feature falls well within the energy limits of channels 1A and 1B; given its falloff near $E_T^{\min}$ for channel 1A, we assign it to this pathway, leading once again to vibrationally excited diatomic fragments. The anisotropy parameter obtained at 4.43 eV is 1.58 ± 0.51, an anisotropic distribution reflecting prompt dissociation following a parallel transition.

The final feature to consider in Figure 4.2 is the broad, low energy feature evident at low E_T in the $P(E_T)$ distributions for 4.43 and 4.59 eV. We were unable to unambiguously assign this feature. Some signal in this range can be ascribed to the formation of Br and $I_2^-(^2\Pi_{u,1/2})$, which should fall around $E_T + \Delta E_{h\nu} > 0.36$ eV. This state of I_2^- is calculated to be very weakly bound (0.08 - 0.19 eV).[59-61] Very low E_T events observed at 4.59 eV may be due to dissociative photodetachment (DPD), $I_2 + \mathrm{Br} + e^-$. While the adiabatic EA of IIBr is not precisely known, a lower bound of 4.0 eV was inferred from the photoelectron spectrum presented by Mabbs *et al.*[27] $D_0(I_2 - \mathrm{Br})$ was calculated by Sims *et al.* to be about 0.62 eV,[62] and Lee *et al.*[63] estimated $D_0(I_2 - \mathrm{Br}) \geq 0.43$ eV based on Br + I_2 cross beam experiments. The energy available for translation, $E_{T,avail}$, in DPD is given by

$$E_{T,avail} = h\nu + E_{\mathrm{int}}^- - EA - D_0\,, \tag{4.3}$$

where E_{int}^- is the internal energy of the anion. Assuming $E_{\mathrm{int}}^- = 0$, $D_0 \geq 0.43$ eV, and EA = 4.0 eV, then $E_{T,avail} \leq 0.16$ eV at 4.59 eV, which is consistent with some of the intensity observed at low E_T at that energy.

4.5.2 Two-body dissociation: I + IBr fragments

$P(E_T)$ distributions for mass channel 2, I + IBr fragments, are presented in Figure 4.3a. The distributions are plotted against $E_T + \Delta E_{h\nu}$ as in Figure 4.2. At 4.13 eV, there is a sharp feature near 1.3 eV. This feature occurs near $E_T^{\min}$ for channels 2A, 2C, and 2E, corresponding to $I^-(^1S)$ and neutral IBr in its ground electronic state $(X\,^1\Sigma^+)$ or its first two excited states. This feature diminishes significantly at higher photon energies. The sharp decrease in signal intensity below $E_T^{\min}$ implies the feature is due to dissociation via one or more of these three channels, and that the IBr fragment is highly vibrationally excited regardless of its electronic state. The anisotropy parameter was measured to be $\beta(E_T)$ = -0.20 ± 0.03, indicating a slightly perpendicular transition.

Also at 4.13 eV, a feature appears around $E_T + \Delta E_{h\nu} \approx 1.15$ eV, overlapping the other feature. This feature falls within the limits of channel 2D, $\mathrm{I}^*(^2P_{1/2}) + \mathrm{IBr}^-(X\,^2\Sigma^+_{1/2})$. It peaks near 50% of $E_T^{\min}$, indicating IBr^- fragments are produced in a range of vibrational levels. A similar feature is also apparent at $E_{h\nu}$ = 4.20 eV, though diminished, and no evidence for this channel is observed at higher photon energies. The anisotropy parameter was measured as $\beta(E_T)$ = -0.70 ± 0.06, indicating a perpendicular transition.

At all photon energies ≥ 4.20 eV, the most intense feature in the $P(E_T)$ distributions is a sharp peak near $E_T + \Delta E_{h\nu} \approx 1.65$ eV; this peak is not seen at all at 4.13 eV. While it appears within the energetic limits of channel 2A and arguably 2C, this feature drops to nearly zero intensity where $E_T < E_T^{\min}$ of channel 2B, $\mathrm{I}(^2P_{3/2}) + \mathrm{IBr}^-(X\,^2\Sigma^+_{1/2})$, leading us to assign it to this channel. The close alignment with $E_T^{\min}$ once again indicates the diatomic fragment is produced near its dissociation asymptote. An anisotropy parameter of $\beta(E_T)$ = 0.22 ± 0.07 was measured, indicating a slightly parallel transition.

At 4.43 and 4.59 eV, a small feature is evident at $E_T + \Delta E_{h\nu} \approx 0.85$ eV. This feature falls within the relatively small energy range corresponding to channel 2F, $\mathrm{I}^-(^1S) + \mathrm{IBr}(B\,^3\Pi^+_0)$. There is a low intensity feature observed at each dissociation wavelength around $E_T + \Delta E_{h\nu} \approx 2.35$ eV, which appears to be low internal energy photoproducts from either channel 2A or 2B. Due to low signal intensity, the anisotropy parameter for this peak could not be unambiguously determined. Finally, a low E_T feature is observed in the $P(E_T)$ distribution obtained by photodissociation at 4.59 eV. We tentatively assign this to dissociative photodetachment.

Figure 4.3a also shows a feature that shifts smoothly from $E_T + \Delta E_{h\nu} \approx 1.85$ eV at 4.13 eV to 2.10 eV by 4.59 eV, appearing as a distinct, sharp peak at photon energies ≥ 4.20 eV. While the features fall well within the energetic bounds of several dissociation pathways, such as channel 2B, there is no clear correspondence to any channel. Furthermore, it is surprising that the diatomic products would be produced with less internal energy as the photon energy increases. We attempt to resolve this riddle by recalling the possible presence of three-body dissociation from IIBr^- where only the two terminal atoms are detected and the central I atom hits the beam block, giving a mass ratio of 79:127 = 0.622. As noted in Section 4.4, this mass ratio is coincidentally nearly identical to mass channel 2 (127:206 = 0.617), and would be assigned to the same mass channel. Because the mass of the parent anion is assumed in our analysis, three-body dissociation events with only two detected fragments will appear to have a higher mass, leading to $P(E_T)$ distributions artificially shifted to higher kinetic energy release.

The false two-fragment $P(E_T)$ distribution can be corrected to the three-body distribution by scaling by the ratio of masses

$$E_{3body} = \frac{m_{3body}}{m_{2\,frag}} E_{2\,frag} = 0.619 E_{2\,frag} \tag{4.4}$$

where E_{3body} and E_{2frag} are the translational energies of the corrected three-body dissociation and the observed two-fragment E_T, $m_{3body} = m_{Br} + m_I$, and $m_{2frag} = m_{Br} + 2m_I$. Figure 4.3b shows the same distributions as in Figure 4.3a plotted vs. the scaled energy 0.619 ($E_T + E_{h\nu}$). The features in question all line up in this plot at a scaled energy of 1.306 eV, which corresponds to the expected kinetic energy release from channel 3B at 4.59 eV photon energy, as discussed further in the next section.

4.5.3 Three-body dissociation

The three-body photofragment $P(E_T)$ distributions presented in Figure 4.4 are simpler to assign since only atomic fragments are produced, ideally at discrete kinetic energies. At every wavelength, the dominant three-body channel is 3B, dissociation to $\mathrm{Br} + \mathrm{I} + \mathrm{I}^-$. We attribute the high kinetic energy tail to internally excited anions in the molecular beam. Also present in each panel of Figure 4.4 is a feature from the lower energy channel 3A, $\mathrm{Br}^- + \mathrm{I} + \mathrm{I}$. In the $P(E_T)$ distributions obtained with photon energies of 4.28 eV and higher, a small feature from channel 3C is in evidence, corresponding to dissociation into spin-orbit excited $\mathrm{Br}^*({}^2P_{1/2})$ and $\mathrm{I} + \mathrm{I}^-$. There is some evidence for channel 3D, leading to $\mathrm{Br}^- + \mathrm{I} + \mathrm{I}^*$, at 4.59 eV.

The Dalitz plots presented in Figures 4.5 and 4.6 provide additional insight into the three-body dissociation dynamics. The Dalitz plots in Figure 4.5 are constructed from events associated with the high E_T feature assigned to channel 3A in the $P(E_T)$ distributions in Figure 4.4, while those in Figure 4.6 come from the low E_T feature assigned to channel 3B. Dalitz plots for channels 3C and 3D are not considered due to low signal. The three Dalitz plots on the right in both figures come from narrow (0.04 eV) translational energy ranges near the peaks of the features, which should correspond to dissociation from anions with minimal internal energy.

Beginning with the 4.13 eV Dalitz plot in Figure 4.5, there is intensity in the region of one o'clock. This indicates events where one iodine fragment receives little momentum ($f_{\mathrm{I}} < 0.10$) and the other iodine fragment receives the bulk of the momentum balance ($f_{\mathrm{I'}} > 0.45$). Points along the perimeter of a Dalitz plot necessarily correspond to collinear dissociation. The cluster of points near one o'clock is therefore consistent with concerted dissociation from a linear configuration of IIBr^-, in which both bonds break on the time scale of vibrational motion in the anion.[64] The one o'clock feature is present in Figure 4.6 as well,

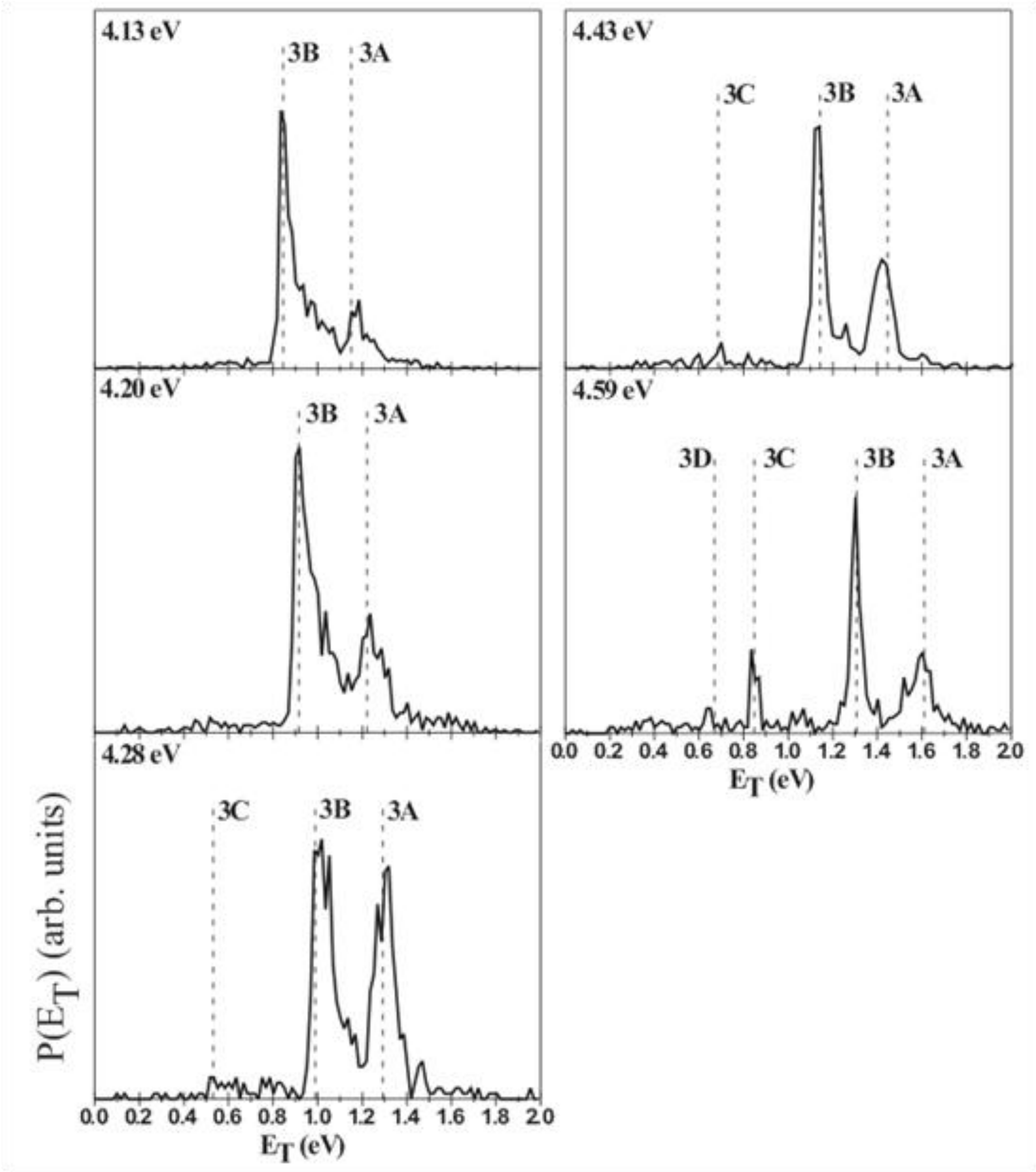

Figure 4.4 Photofragment translational energy distributions for three-body dissociation of I_2Br^- upon excitation by photon energies of 4.13 - 4.59 eV. The expected kinetic energy release for channels 3A - D are indicated by dashed lines.

implying the same dissociation mechanism for both features. Points in the interior of the Dalitz circle are consistent with dissociation from anions with excitation in the bending mode, and they largely disappear when plotting the narrower energy range. Similar characteristics are observed at all of the other dissociation wavelengths and imply the mechanism does not change with additional energy. One difference is that points along the perimeter cluster more closely to the one o'clock

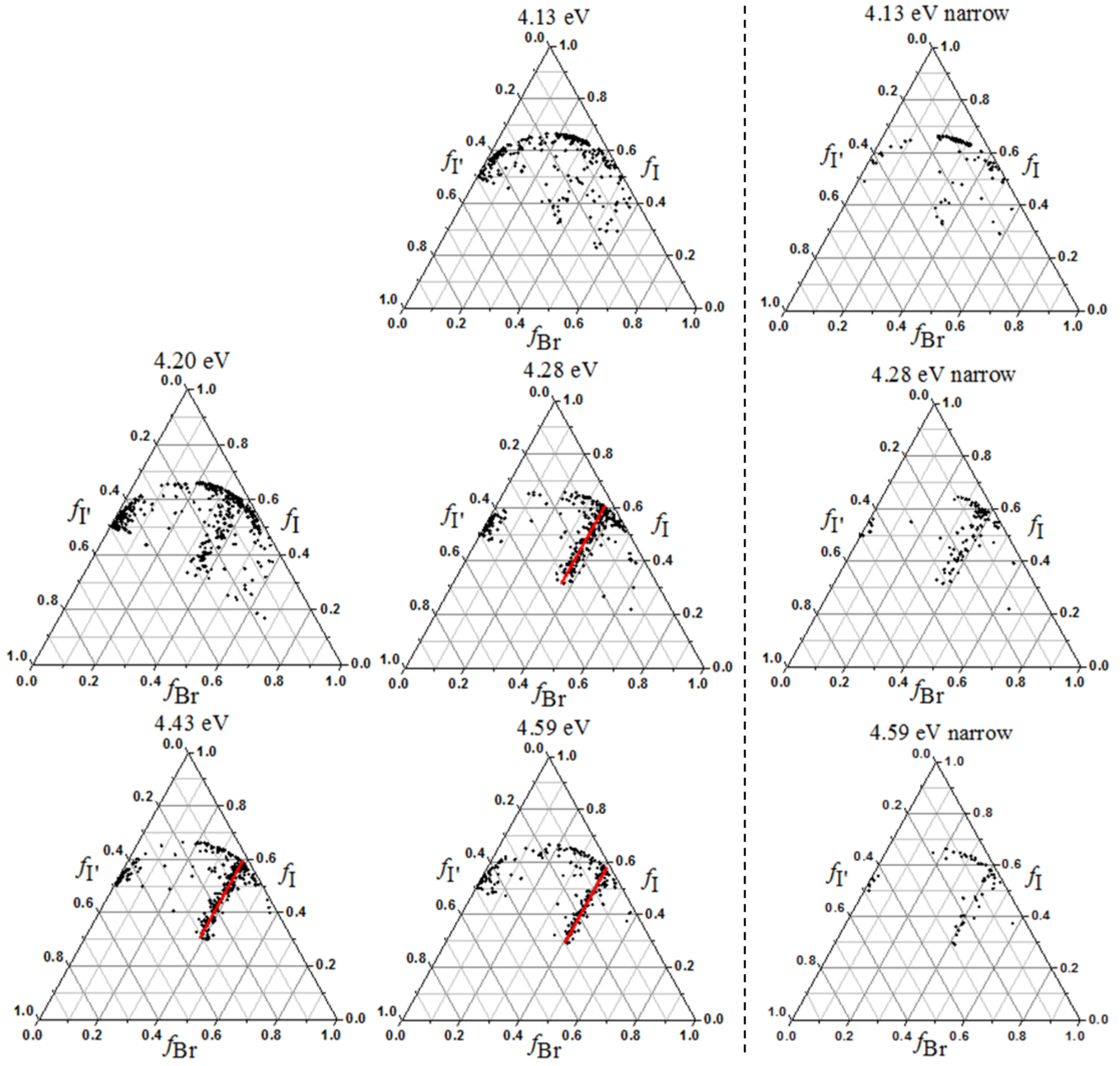

Figure 4.5 Dalitz plots of momentum partitioning among the three fragments in the three-body dissociation of I_2Br^- upon excitation by photon energies of 4.13 - 4.59 eV. Points correspond to the 3A feature in the three-body $P(E_T)$. The red line in the plots for 4.28 - 4.59 eV is result of a simulation for sequential decay (see text). The three plots on the right correspond to narrow energy ranges (0.04 eV) around the peak in the $P(E_T)$ distribution.

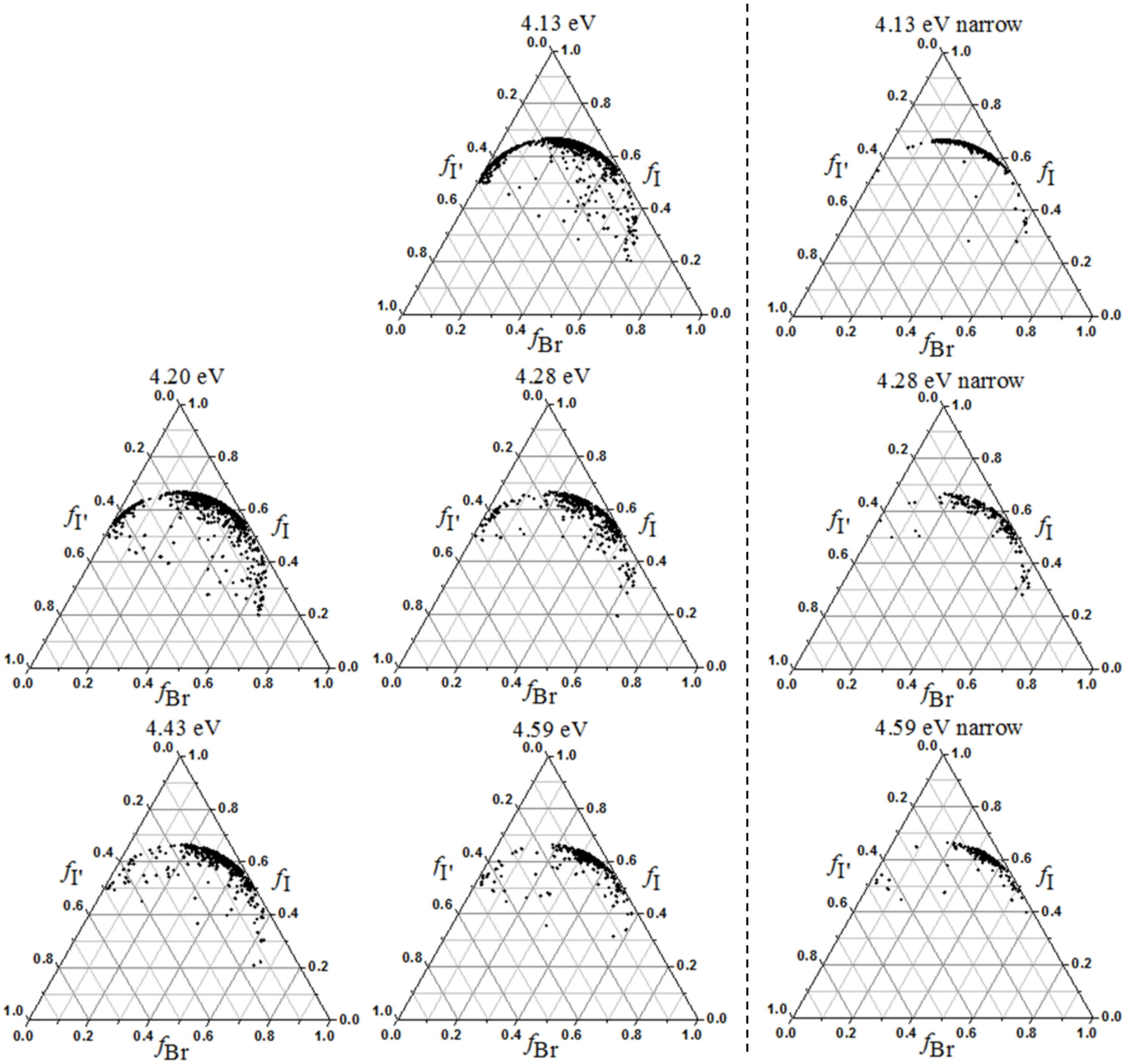
4.13 eV

4.13 eV narrow

4.20 eV

4.28 eV

4.28 eV narrow

4.43 eV

4.59 eV

4.59 eV narrow

Figure 4.6 Dalitz plots of momentum partitioning among the three fragments in the three-body dissociation of I_2Br^- upon excitation by photon energies of 4.13 - 4.59 eV associated with the 3B feature in the three-body *P(E$_T$)*. The three plots on the right correspond to narrow energy range (0.04 eV) around the peak in the *P(E$_T$)* distribution.

region with dissociation from 4.43 and 4.59 eV. This effect is mirrored in the $P(E_T)$ distributions in Figure 4.4, where the lower E_T feature is sharper at these higher photon energies compared to lower photon energies. The likely reason is that the fractional contribution of ion vibrational excitation to translational energy release decreases as the total translational energy goes up (due to increased available energy).

The feature centered near ten o'clock in Figures 4.5 and 4.6 corresponds to events where the bromine fragment receives very little momentum ($f_{\mathrm{Br}} < 0.05$) and the iodine fragments split the momentum balance roughly equally, as would be expected from dissociation of $\mathrm{IBrI^-}$. It is tempting to attribute this signal to higher-lying $\mathrm{IBrI^-}$ isomer produced in our ion source. However, there is no compelling evidence for two-body dissociation from this species; all the I + IBr features in Fig. 4.3 can be assigned to photodissociation of $\mathrm{IIBr^-}$. This feature is largely eliminated in the right three panels of Figs. 4.5 and 4.6, where the Dalitz plots are restricted to a narrow energy range centered at the peak of features 3A and 3B, respectively. This result suggests that the low f_{Br} feature originates from vibrationally excited anions. We thus propose that it originates from bend-excited anions; when these anions are electronically excited, they can isomerize prior to dissociation. Note that the calculations of Landrum *et al.*[20] showed that the 6σ LUMO is lower in energy for $\mathrm{IBrI^-}$ than for $\mathrm{IIBr^-}$, so population of this orbital upon excitation could play a role in isomerization.

Moving on to the Dalitz plot for 4.28 eV in Figure 4.5, a line of points is observed which corresponds to constant bromine momentum partitioning ($f_{\mathrm{Br}} \approx 0.37$) and randomized iodine fragment momenta. A similar feature is hinted at in the 4.20 eV Dalitz plot and is clearly evident at 4.43 and 4.59 eV. This feature is characteristic of a sequential dissociation, where the momentum of one fragment is determined independently of the other two fragment momenta.[65,66]

The kinematics of sequential dissociation can be described by a model adapted from Matsuda *et al*, [65] who used it to describe sequential fragmentation from Coulomb explosion of the benzene trication. Following dissociation of the form $XYZ + h\nu \rightarrow X + YZ \rightarrow X + Y + Z$, we assume the first atom to depart does so in the negative x direction, and that the resulting diatomic molecule can rotate freely subsequent to the initial bond dissociation. The final COM momenta of the atomic fragments resulting from *XYZ* can be described with the following set of vector equations:

$$\mathbf{p}(X) = -\mathbf{p}_1 = (-p_1,\, 0) \tag{4.5a}$$

$$\mathbf{p}(Y) = \frac{m(Y)}{m(YZ)}\mathbf{p}_1 + \mathbf{p}_2 = (\frac{m(Y)}{m(YZ)}\, p_1 + p_2 \cos\phi,\; p_2 \sin\phi) \tag{4.5b}$$

$$\mathbf{p}(Z) = \frac{m(Z)}{m(YZ)}\mathbf{p}_1 + \mathbf{p}_2 = (\frac{m(Z)}{m(YZ)} p_1 - p_2 \cos\phi,\ - p_2 \sin\phi) \tag{4.5c}$$

where m is the mass of the fragment, $\mathbf{p}_1$ and $\mathbf{p}_2$ are the vector momenta imparted to the fragments in the first and second steps, respectively, and ϕ is the angle between momenta $\mathbf{p}_1$ and $\mathbf{p}_2$. The COM translational energy released in the first and second steps of the sequential dissociation, E_1 and E_2, are related to the momenta by the reduced mass of each dissociating system:

$$E_1 = \frac{[m(X) + m(YZ)]p_1^2}{2m(X)m(YZ)} \tag{4.6a}$$

$$E_2 = \frac{[m(Y) + m(Z)]p_2^2}{2m(Y)m(Z)}. \tag{4.6b}$$

Because E_T is well-defined for each three-body decay event, we partition the total E_T between E_1 and E_2 with a single parameter ε, so that $E_1 = \varepsilon E_T$ and $E_2 = (1-\varepsilon)E_T$, following similar analysis by Savee *et al.*[66] The results of plotting momenta over all ϕ in a Dalitz plot and adjusting ε to fit our experimental results are shown in red in Figure 4.5 for 4.28 – 4.59 eV, where the constant f_{Br} feature was clearly present. The resulting values of E_1 and ε for each photon energy are shown in Table 4.3. We find that as the photon energy increases, E_1 increases as a fraction of total E_T. This is consistent with a sequential mechanism where the first dissociation step is immediate, and produces an atomic Br fragment and a metastable I_2 diatomic fragment which dissociates prior to detection ~30 μs after interaction with the photodissociation laser.

Table 4.3 Numbers relevant for sequential dissociation for photon energies of 4.28 - 4.59 eV. E_T is the total energy deposited in translation. ε is a parameter describing the partitioning of E_T between the two dissociation steps (see text). E_1 is translational energy imparted in the first dissociation step. $E_1 + \Delta E_{h\nu}$ adjusts for the difference between photon energies.

hν	E_T	ε	E_1	$E_1 + \Delta E_{h\nu}$
4.28	1.28	0.63	0.81	1.13
4.43	1.43	0.66	0.94	1.10
4.59	1.6	0.69	1.10	1.10

Assuming imperfect efficiency of the secondary dissociation, one would expect to see a correlation between E_1 and some feature in the two-body $P(E_T)$ distribution for mass channel 1. Comparing the $E_1 + \Delta E_{h\nu}$ values given in Table 4.3, all of which are ~1.1 eV, to the $P(E_T)$ distributions in Figure 4.2, we find a clear correspondence to the feature assigned to channel 1E, $\mathrm{Br}^-(^1S)+\mathrm{I}_2(B^3\Pi^+_{0u})$, with values close to $E_T^{\max}$. We thus propose the following sequential dissociation mechanism for IIBr^-: upon absorption (hv ≥ 4.20 eV), IIBr^- is excited to an electronic surface correlating to $\mathrm{Br}^-(^1S)+\mathrm{I}_2(B^3\Pi^+_{0u})$ products; some fraction of the metastable $\mathrm{I}_2(B^3\Pi^+_{0u})$ fragments then undergoes electronic predissociation via repulsive surfaces correlating to ground state I atoms.

4.5.4 Thermodynamic quantities

The dissociation energy of $\mathrm{I}_2\mathrm{Br}^-$ can be directly obtained from the three-body $P(E_T)$ distributions in Fig. 4.4, taking the peak of the sharp 3B feature, $E^{3B}_{T,peak}$, as our reference point. $D_0(\mathrm{I}^- - \mathrm{IBr})$ is then obtained by

$$D_0(\mathrm{I}^- - \mathrm{IBr}) = h\nu - E^{3B}_{T,peak} - D_0(\mathrm{I}-\mathrm{Br}), \qquad (4.7)$$

where $D_0(\mathrm{I}-\mathrm{Br})$ = 1.8181 ± 0.0001 eV, taken from the literature.[67,68] We find $D_0(\mathrm{I}^- - \mathrm{IBr})$ to be 1.469 ± 0.01 eV, in good agreement with our calculated value of D_e = 1.44 eV. Similarly, using the known electron affinities[49] of I and Br, we report $D_0(\mathrm{Br}^- - \mathrm{I}_2)$ = 1.442 ± 0.01 eV, which is comparable to our calculated value of 1.42 eV. These results, both experimental and theoretical, differ by less than 0.2 eV from the bond energies calculated by Ogawa *et al*,[21] who found $D_0(\mathrm{Br}^- - \mathrm{I}_2)$ = $D_0(\mathrm{I}^- - \mathrm{IBr})$ = 1.30 eV and those of Landrum *et al.*,[20] who calculated a bond energy of $D_0(\mathrm{I}^- - \mathrm{IBr})$ = 1.59 eV.

With our bond dissociation energies, the 0 K heat of formation, $\Delta_f H(\mathrm{I}_2\mathrm{Br}^-_{(g)})$ can be determined by Equation 4.8,

$$\Delta_f H(\mathrm{I}_2\mathrm{Br}^-{}_{(g)}) = \Delta_f H(\mathrm{I}_{2(g)}) + \Delta_f H(\mathrm{Br}^-_{(g)}) - D_0(\mathrm{Br}^- - \mathrm{I}_2), \qquad (4.8)$$

where $\Delta_f H(\mathrm{I}_{2(g)})$ = 65.50 ± 0.08 kJ·mol-1,[69] and $\Delta_f H(\mathrm{Br}^-_{(g)})$ = -206.60 ± 0.12 kJ·mol-1 was determined from $\Delta_f H(\mathrm{Br}_{(g)})$ = 117.93 ± 0.12 kJ·mol-1 [69] and its EA.[49] We determine $\Delta_f H(\mathrm{I}_2\mathrm{Br}^-_{(g)})$ to be -2.90 ± 0.01 eV, or -280.2 ± 1 kJ·mol-1.

4.5.5 Branching fractions

Branching fractions were determined for dissociation into two versus three fragments as well as for disposal of the extra electron. These are presented in Table 4.4. Error bars were estimated by approximating the area under the curves for regions where assignments are unclear due to spectral overlap. For two- and three-body channels, the first column gives the fraction of total events decaying into two or three fragments. The columns to the right give the branching fractions according to where the excess electron is disposed. Three-body events constitute about a third of the total number detected, and their production does not show much dependence on wavelength. It should be noted the total fraction assigned to three-body dissociation is a lower limit, as three-fragment events are detected less efficiently than two-fragment events in our detection scheme.

Table 4.4 reveals several interesting trends. The most likely anion produced is I^-, similar to the observations of Mabbs *et al.*[27] following excitation to the lower energy band (3.2 eV). All possible anion products are produced at each photon energy, though I_2^- becomes a more minor channel at the highest photon energies employed.

4. 6 Discussion

These experiments demonstrate the rich photodissociation dynamics of I_2Br^- from the upper absorption band, which involve multiple two- and three-body channels. Since little is known about the excited states of I_2Br^-, comparison with

Table 4.4 Branching fractions for two- and three-body dissociation of I_2Br^- and disposal of the excess electron.

Photon energy (eV)	Two-body					Three-body		
	fraction of total	Br^-	I^-	IBr^-	I_2^-	fraction of total	Br^-	I^-
4.13	0.68	0.20(8)	0.26(2)	0.22(7)	0.32(8)	0.32	0.09(6)	0.91(6)
4.20	0.68	0.21(5)	0.14(2)	0.23(3)	0.42(5)	0.32	0.16(3)	0.84(3)
4.28	0.72	0.21(4)	0.20(2)	0.24(2)	0.35(2)	0.28	0.32(2)	0.68(2)
4.43	0.71	0.21(4)	0.28(2)	0.38(2)	0.13(3)	0.29	0.26(2)	0.74(2)
4.59	0.67	0.22(2)	0.34(3)	0.34(3)	0.10(2)	0.33	0.20(2)	0.80(2)

the better-characterized triiodide anion is quite useful. Photodissociation of I_3^- involves excitation from the ground ${}^1\Sigma_g^+(0_g^+)$ state to the repulsive ${}^1\Sigma_u^+(0_u^+)$ excited state, after which branching into different dissociation pathways occurs by passing through various avoided crossings and conical intersections.[15,70] Our results are consistent with a similar picture for the isovalent I_2Br^- molecule. However, one notable difference is that the value of the anisotropy parameter β differs for the various two-body dissociation channels for I_2Br^-, whereas it was approximately constant and positive (1.4 ± 2) for all channels for I_3^-. This result suggests that more excited electronic states are being accessed for I_2Br^-. We generally do find positive values of β for mass channel 1 and negative values for mass channel 2, although even this generalization is not perfect (i.e., $\beta > 0$ for the feature assigned to channel 2C in Fig. 4.3a).

Upon absorption at 4.13 eV, Table 4.4 shows that dissociation preferentially proceeds along channels producing $I_2^-(X\,{}^2\Sigma_u^+)$ or I^-, with some contribution from channels 1A or 1D, producing Br^-. In each case, the *P(E_T)* distribution includes events at the edge of $E_T^{\min}$, reflecting maximum internal excitation of the diatomic fragment. Upon dissociation into three atoms, the excess electron is most likely to leave with an I atom, especially at hν ≤ 4.20 eV. The high level of vibrational excitation in the photoproducts is consistent with the large differences in bond lengths between the ground state anions and the diatomic products. For example, our calculated value for the ground state anion bond length, $R_{eq}(\mathrm{II-Br^-})$ = 2.748 Å, is significantly longer than that of ground state IBr (2.469 Å)[67,68]. A simple Franck-Condon picture[71] of the photodissociation dynamics would predict high vibrational excitation of the IBr fragment, in agreement with our observations. Similarly, $R_{eq}(\mathrm{BrI-I^-})$ = 2.936 Å differs significantly from the I-I bond length in both ground state I_2^- (3.205 Å)[46] and neutral I_2 (2.666 Å).[72]

These energy distributions are similar to those from the lower absorption band of I_3^-, where the two-body channels blended seamlessly into the corresponding three-body channels,[14] and suggest that two- and three-body dissociation occur via the same dynamical process. Specifically, at 4.13 eV, as $\mathrm{Br}({}^2P_{3/2})+I_2^-(X\,{}^2\Sigma_u^+)$ and $I^-({}^1S)+\mathrm{IBr}$ channels (1B and 2A,B,C) correlate to channel 3B in the limit of maximum internal excitation of the diatomic fragment, the two-body *P(E_T)* distributions all feature sharp fall-offs at $E_T^{\min}$. In this dynamical picture, $IIBr^-$ is excited to a manifold of electronic excited states, and dissociation occurs along a repulsive surface via the stretching coordinate, resulting in three-body dissociation or an atom and a vibrationally excited diatomic when one bond fails to cleave. This mechanism is consistent with the Dalitz plot of channel 3B in Figure 4.6, which indicates that dissociation proceeds primarily by a concerted mechanism where both bonds break before the diatomic product has a chance to rotate, resulting mainly in collinear dissociation events at the perimeter of the inscribed circle.

Excitation at 4.20 eV produces different dynamics in mass channel 2. The two-body pathway producing $\mathrm{I}^-(^1S)+\mathrm{IBr}$ products (from channels 2A, C, or E) has diminished and a feature corresponding to three-body dissociation where only an iodine and a bromine are detected has grown in intensity in Figure 4.3b. Three-body dissociation of IIBr^- where only the terminal atoms are detected must come from events where the central iodine atom has struck the beam block in front of the detector. Given the asymmetry of the molecule, a concerted three-body dissociation would impart nonzero momentum to the central atom, allowing it to pass by the beam block. For a central I fragment to strike the beam block, some events corresponding to very little or zero iodine momentum must occur. Similar events, where all three fragments are detected, should be observable in the Dalitz plots in Figure 4.6. Such events are evident at $f_{I'} = 0$.

At 4.28 eV, $\mathrm{I}(^2\mathrm{P}_{3/2})+\mathrm{IBr}^-(\mathrm{X}\,^2\Sigma^+_{1/2})$ is a dominant channel (2B). As $\mathrm{IBr}^-(X\,^2\Sigma^+_{1/2})$ correlates to Br^- and ground state $\mathrm{I}(^2P_{3/2})$, the feature assigned to channel 2B in the *P(E$_T$)* distribution also extends through $E_T^{\min}$ into the three-body *P(E$_T$)* distribution for channel 3A. This reflects concerted dissociation similar to the case of channel 3B discussed above. Neutral I_2 is also observed, in its ground electronic state as well as in the $(B\,^3\Pi^+_{0u})$ state. As hν is increased from 4.28 to 4.43 and 4.59 eV, signal from $\mathrm{Br}(^2P_{3/2})+\mathrm{I}_2^-(X\,^2\Sigma^+_u)$ (channel 1B) diminishes while signal from channel 1E increases. This increase in intensity correlates with a stronger line of constant f_{Br} in the Dalitz plots in Figure 4.5, consistent with an increasing population of predissociating $\mathrm{I}_2(B\,^3\Pi^+_{0u})$. In contrast to several of the features mentioned above, the *P(E$_T$)* feature resulting from channel 1E peaks near $E_T^{\max}$, indicating low internal energy in $\mathrm{I}_2(B)$. In addition to the growing contribution from channel 1E, excitation by higher energy photons results in the population of several minor channels, reflecting a greater number of electronic excited states being accessed. Channel 2F, producing $\mathrm{I}^-(^1S)$ and $\mathrm{IBr}(B\,^3\Pi^+_0)$ fragments, appears at hν ≥ 4.28 eV; this coincides with the appearance of channel 3C, producing $\mathrm{Br}^*(^2P_{1/2})$.

The three-body photodissociation dynamics of 4.28 – 4.59 eV are of particular interest, specifically the line of constant f_{Br} hinted at in the 4.20 eV Dalitz plot for channel 3A and clearly present at the three highest photon energies. As discussed in Section 4.5.C, this line indicates a sequential three-body decay, where the first bond breaks, leaving a metastable fragment, $\mathrm{I}_2(B\,^3\Pi^+_{0u})$ in this case, destined later to undergo a second dissociation step. $\mathrm{I}_2(B\,^3\Pi^+_{0u})$ is known to electronically predissociate via coupling to the $\mathrm{I}_2(B''\,^1\Pi_{1u})$ repulsive curve, leading to ground state iodine atoms.[73-76] The predissociation occurs on the order of μs,[77] and is dependent on the (v, J) levels populated, with Franck-Condon density (FCD) maxima occurring at v = 5 and v = 25, and a minimum at v = 14. Fluorescence from the *B-X* transition also occurs to some extent at all vibrational levels, with maxima around v < 5 and v = 25 and a global minimum near the dissociation asymptote.[77] The ratio of the rate of predissociation to that of fluorescence has a minimum at v = 14.[75] The average E_I of 1.11 eV (Table 4.3) corresponds to $\mathrm{I}_2(B)$ with v ≈ 6, which is close to the FCD maximum of v = 5. Both radiative decay and predissociation are possible at the low v levels observed in our experiment. The two-body events producing $\mathrm{I}_2(B)$ fragments have likely undergone radiative decay, which occurs on a similar timescale of 0.4 - 7 μs,[77] consistent with our detection ~30 μs after absorption.

It is interesting that no evidence for similar sequential three-body dissociation has been observed in I_3^-, either in our group[13,14] or others.[15,16] While we only tentatively assigned an $\mathrm{I}^-({}^1S)+\mathrm{I}_2(B\,{}^3\Pi_{0u}^+)$ product channel, Nakanishi[15] assigned the channel at nearly the same photon energy (4.28 eV and 4.27 eV, respectively) with a branching fraction of 0.11. Although $\mathrm{Br}^-({}^1S)+\mathrm{I}_2(B\,{}^3\Pi_{0u}^+)$ in the present study is a more significant channel than $\mathrm{I}^-({}^1S)+\mathrm{I}_2(B\,{}^3\Pi_{0u}^+)$ in the I_3^- system, evidence for sequential dissociation is quite distinctive in the Dalitz analysis used by us for both ions. We infer from this that any $\mathrm{I}_2(B\,{}^3\Pi_{0u}^+)$ fragments produced in the photodissociation of I_3^- do not later undergo electronic predissociation. As there is significant overlap in the energetics of the $\mathrm{I}^-({}^1S)+\mathrm{I}_2(B\,{}^3\Pi_{0u}^+)$ channel and $\mathrm{I}^*({}^2P_{1/2})+\mathrm{I}_2^-(X\,{}^2\Sigma_u^+)$, it is difficult to infer the vibrational distribution of $\mathrm{I}_2(B)$ in the two-body $P(E_T)$ distributions. It is possible that any $\mathrm{I}_2(B)$ fragments detected in those experiments were produced in vibrational levels around v = 14 or significantly higher than v = 25 (the second predissociation peak).[77] These $\mathrm{I}_2(B)$ fragments likely undergo fluorescence before detection, as fluorescence at any vibrational level is on the order of a few μs and thus consistent with our detection timeline (> 30 μs in the I_3^- experiment).

4. 7 Conclusions

We have investigated the photodissociation dynamics of IIBr$^-$ using a fast beam photofragment translational spectrometer. The anions were photodissociated at five energies between 4.13 and 4.59 eV. Fragments from both two- and three-body events were collected and analyzed using a time- and position-coincidence imaging detector. At each dissociation wavelength, photofragment mass ratios and translational energy [$P(E_T)$] distributions were measured and three-body Dalitz plots were constructed.

Both two- and three-body dissociation channels were detected at each wavelength employed, with three-body dissociation from $\mathrm{IIBr^-}$ constituting about a third of events detected at each photon energy. Some shifts in $\mathrm{IIBr^-}$ photodissociation dynamics are observed between 4.13 eV and 4.28 - 4.59 eV. While two-body channels producing $\mathrm{I_2^-}(X\,^2\Sigma_u^+)$ and $\mathrm{IBr}(X\,^1\Sigma^+)$ channels dominate at the lowest photon energy, both channels diminish at the higher excitation energies and are eclipsed by $\mathrm{Br^-}(^1S)+\mathrm{I_2}(B\,^3\Pi_{0u}^+)$ and $\mathrm{I}(^2\mathrm{P}_{3/2})+\mathrm{IBr^-}(\mathrm{X}\,^2\Sigma_{1/2}^+)$ pathways. The two-body $\mathrm{I^-}(^1S)$ channel appears to be replaced by three-body dissociation upon higher excitation.

Finally, in the three-body dynamics observed, $\mathrm{I^-}(^1S)+\mathrm{I}(^2P_{3/2})+\mathrm{Br}(^2P_{3/2})$ was the preferred pathway at every wavelength, although $\mathrm{I}(^2P_{3/2})+\mathrm{I}(^2P_{3/2})+\mathrm{Br^-}(^1S)$ was always present. Analysis of momentum disposal in three-body events using Dalitz plots shows both channels occur by concerted bond cleavage, under some influence of bending motions. In addition, the Dalitz plots reveal that $\mathrm{I}(^2P_{3/2})+\mathrm{I}(^2P_{3/2})+\mathrm{Br^-}(^1S)$ also occurs by sequential dissociation via primary generation of $\mathrm{Br^-}(^1S)$ and metastable $\mathrm{I_2}(B\,^3\Pi_{0u}^+)$, which subsequently predissociates via coupling to a repulsive curve correlating to ground state products. Interestingly, there is no evidence for such sequential decay in the photodissociation of $\mathrm{I_3^-}$ in similar wavelength ranges.

Acknowledgments

This research was supported by the Director, Office of Basic Energy Science, Chemical Sciences Division of the U.S. Department of Energy under Contract No. DE-AC02-05CH11231. The authors thank Etienne Garand for his help with the calculations.

References

[1] G. C. Pimentel, J. Chem. Phys. **19**, 446 (1951).

[2] A. Barkatt and M. Ottolenghi, Mol. Photochem. **6**, 253 (1974).

[3] L. I. Grossweiner and M. S. Matheson, J. Phys. Chem. **61**, 1089 (1957).

[4] J. C. Roy, W. H. Hamill, and R. R. Williams, J. Am. Chem. Soc. **77**, 2953 (1955).

[5] P. O'Driscoll, K. Lang, N. Minogue, and J. Sodeau, J. Phys. Chem. A **110**, 4615 (2006).

[6] D. O'Sullivan and J. R. Sodeau, J. Phys. Chem. A, (2010).

[7] G. Boschloo and A. Hagfeldt, Accts. Chem. Res. **42**, 1819 (2009).

[8] U. Banin, A. Waldman, and S. Ruhman, J. Chem. Phys. **96**, 2416 (1992).

[9] E. Gershgoren, E. Gordon, and S. Ruhman, J. Chem. Phys. **106**, 4806 (1997).

[10] M. T. Zanni, B. J. Greenblatt, A. V. Davis, and D. M. Neumark, J. Chem. Phys. **111**, 2991 (1999).

[11] K. Do, T. P. Klein, C. A. Pommerening, and L. S. Sunderlin, J. Am. Soc. Mass Spectrom. **8**, 688 (1997).

[12] T. R. Taylor, K. R. Asmis, M. T. Zanni, and D. M. Neumark, J. Chem. Phys. **110**, 7607 (1999).

[13] H. Choi, R. T. Bise, A. A. Hoops, and D. M. Neumark, J. Chem. Phys. **113**, 2255 (2000).

[14] A. A. Hoops, J. R. Gascooke, A. E. Faulhaber, K. E. Kautzman, and D. M. Neumark, J. Chem. Phys. **120**, 7901 (2004).

[15] R. Nakanishi, N. Saitou, T. Ohno, S. Kowashi, S. Yabushita, and T. Nagata, J. Chem. Phys. **126**, 17 (2007).

[16] L. Zhu, K. Takahashi, M. Saeki, T. Tsukuda, and T. Nagata, Chem. Phys. Lett. **350**, 233 (2001).

[17] A. D. Walsh, J. Chem. Soc., 2266 (1953).

[18] S. D. Peyerimhoff and R. J. Buenker, J. Chem. Phys. **49**, 2473 (1968).

[19] E. Wiebenga and D. Kracht, Inorg. Chem. **8**, 738 (1969).

[20] G. A. Landrum, N. Goldberg, and R. Hoffman, J. Chem. Soc. Dalton Trans., 3605 (1997).

[21] Y. Ogawa, O. Takahashi, and O. Kikuchi, J. Mol. Struct. (Theochem) **429**, 187 (1998).

[22] A. Sanov, T. Sanford, L. J. Butler, J. Vala, R. Kosloff, and W. C. Lineberger, J. Phys. Chem. A **103**, 10244 (1999).

[23] W. Gabes and D. J. Stufkens, Spectrochim. Acta A **A 30**, 1835 (1974).

[24] A. I. Popov and R. F. Swensen, J. Am. Chem. Soc. **77**, 3724 (1955).

[25] A. G. Maki and R. Forneris, Spectrochim. Acta. A **A 23**, 867 (1967).

[26] E. Eyal and A. Treinin, J. Am. Chem. Soc. **86**, 4287 (1964).

[27] R. Mabbs, K. Pichugin, E. Surber, and A. Sanov, J. Chem. Phys. **121**, 265 (2004).

[28] D. L. Osborn, D. J. Leahy, D. R. Cyr, and D. M. Neumark, J. Chem. Phys. **104**, 5026 (1996).

[29] U. Banin, R. Kosloff, and S. Ruhman, Chem. Phys. **183**, 289 (1994).

30 U. Banin and S. Ruhman, J. Chem. Phys. **98**, 4391 (1993).

31 U. Banin and S. Ruhman, J. Chem. Phys. **99**, 9318 (1993).

32 I. Benjamin, U. Banin, and S. Ruhman, J. Chem. Phys. **98**, 8337 (1993).

33 T. Kuhne, R. Kuster, and P. Vohringer, Chem. Phys. **233**, 161 (1998).

34 T. Kuhne and P. Vohringer, J. Chem. Phys. **105**, 10788 (1996).

35 R. H. Dalitz, Philos. Mag. **44**, 1068 (1953).

36 R. E. Continetti, D. R. Cyr, R. B. Metz, and D. M. Neumark, Chem. Phys. Lett. **182**, 406 (1991).

37 A. A. Hoops, J. R. Gascooke, A. E. Faulhaber, K. E. Kautzman, and D. M. Neumark, Chem. Phys. Lett. **374**, 235 (2003).

38 A. A. Hoops, J. R. Gascooke, K. E. Kautzman, A. E. Faulhaber, and D. M. Neumark, J. Chem. Phys. **120**, 8494 (2004).

39 J. M. B. Bakker, J. Phys. E **6**, 785 (1973).

40 J. M. B. Bakker, J. Phys. E **7**, 364 (1974).

41 Z. Amitay and D. Zajfman, Rev. Sci. Instrum. **68**, (1997).

42 R. E. Continetti, D. R. Cyr, D. L. Osborn, D. J. Leahy, and D. M. Neumark, J. Chem. Phys. **99**, 2616 (1993).

43 K. A. Peterson, B. C. Shepler, D. Figgen, and H. Stoll, J. Phys. Chem. A **110**, 13877 (2006).

44 MOLPRO, a package of *ab initio* programs written by H.-J. Werner, P. J.Knowles, F. R. Manby, M. Schlitz *et al.*, version 2009.1.

45 F. Martin, R. Bacis, S. Churassy, and J. Verges, J. Mol. Spectrosc. **116**, 71 (1986).

46 M. T. Zanni, T. R. Taylor, B. J. Greenblatt, B. Soep, and D. M. Neumark, J. Chem. Phys. **107**, 7613 (1997).

47 W. G. Brown, Phys. Rev. **42**, 0355 (1932).

48 L. Sheps, E. M. Miller, and W. C. Lineberger, J. Chem. Phys. **131**, 8 (2009).

49 J. C. Rienstra-Kiracofe, G. S. Tschumper, H. F. Schaefer, S. Nandi, and G. B. Ellison, Chem. Rev. **102**, 231 (2002).

50 D. R. T. Appadoo, R. J. LeRoy, P. F. Bernath, S. Gerstenkorn, P. Luc, J. Verges, J. Sinzelle, J. Chevillard, and Y. Daignaux, J. Chem. Phys. **104**, 903 (1996).

51 P. Luc, J. Mol. Spectrosc. **80**, 41 (1980).

52 D. T. Radzykewycz, C. D. Littlejohn, M. B. Carter, J. O. Clevenger, J. H. Purvis, and J. Tellinghuisen, J. Mol. Spectrosc. **166**, 287 (1994).

53 E. Wrede, S. Laubach, S. Schulenburg, A. Brown, E. R. Wouters, A. J. Orr-Ewing, and M. N. R. Ashfold, J. Chem. Phys. **114**, 2629 (2001).

54 E. Wrede, S. Laubach, S. Schulenburg, A. J. Orr-Ewing, and M. N. R. Ashfold, Chem. Phys. Lett. **326**, 22 (2000).

55 X. N. Zheng, M. C. Heaven, and J. Tellinghuisen, J. Mol. Spectrosc. **164**, 135 (1994).

56 R. N. Zare, Mol. Photochem. **4**, (1972).

57 D. Babikov, E. A. Gislason, M. Sizun, F. Aguillon, V. Sidis, M. Barat, J. C. Brenot, J. A. Fayeton, and Y. J. Picard, J. Chem. Phys. **116**, 4871 (2002).

[58] L. M. Wiese, O. Yenen, B. Thaden, and D. H. Jaecks, Phys. Rev. Lett. **79**, 4982 (1997).

[59] J. G. Dojahn, E. C. M. Chen, and W. E. Wentworth, J. Phys. Chem. **100**, 9649 (1996).

[60] P. E. Maslen, J. M. Papanikolas, J. Faeder, R. Parson, and S. V. Oneil, J. Chem. Phys. **101**, 5731 (1994).

[61] S. B. Sharp and G. I. Gellene, Mol. Phys. **98**, 667 (2000).

[62] I. R. Sims, M. Gruebele, E. D. Potter, and A. H. Zewail, J. Chem. Phys. **97**, 4127 (1992).

[63] Y. T. Lee, J. D. McDonald, P. R. Lebreton, and D. R. Herschbach, J. Chem. Phys. **49**, 2447 (1968).

[64] C. Maul and K. H. Gericke, Int. Rev. Phys. Chem. **16**, 1 (1997).

[65] A. Matsuda, M. Fushitani, R. A. Thomas, V. Zhaunerchyk, and A. Hishikawa, J. Phys. Chem. A **113**, 2254 (2009).

[66] J. D. Savee, J. E. Mann, and R. E. Continetti, J. Phys. Chem. A **113**, 3988 (2009).

[67] D. R. T. Appadoo, P. F. Bernath, and R. J. Leroy, Can. J. Phys. **72**, 1265 (1994).

[68] T. Yukiya, N. Nishimiya, and M. Suzuki, J. Mol. Spectrosc. **214**, 132 (2002).

[69] P. J. Linstrom and W. G. Mallard, *NIST Chemistry WebBook, NIST Standard Reference Database Number 69*. (National Institute of Standards and Technology, Gaithersburg MD, 20899).

[70] A. S. P. Gomes, L. Visscher, H. Bolvin, T. Saue, S. Knecht, T. Fleig, and E. Eliav, J. Chem. Phys. **133**, (2010).

[71] Y. B. Band and K. F. Freed, J. Chem. Phys. **67**, 1462 (1977).

[72] W. F. Howard, Jr. and L. Andrews, J. Raman Spectrosc. **2**, 447 (1974).

[73] L. Brewer and J. Tellinghuisen, J. Chem. Phys. **56**, 3929 (1972).

[74] J. Tellinghuisen, J. Chem. Phys. **57**, 2397 (1972).

[75] J. Vigué, M. Broyer, and J. C. Lehmann, J. Phys. (Paris) **42**, 949 (1981).

[76] E. A. Pazyuk, A. V. Stolyarov, V. I. Pupyshev, N. F. Stepanov, S. Y. Umanskii, and A. A. Buchachenko, Mol. Phys. **99**, 91 (2001).

[77] G. A. Capelle and H. P. Broida, J. Chem. Phys. **58**, 4212 (1973).

Chapter 5

Two- and three-body dissociation dynamics of hot ozone (O_3) at 193 and 157 nm

The photodissociation of ozone (O_3) was investigated using fast beam photofragment translational spectroscopy. Neutral ozone molecules were produced from ozonide anions by photodetachment at 386 nm (1.1 eV above the electron affinity of ozone). The neutrals were then photodissociated by 193 nm (6.42 eV) or 157 nm (7.86 eV) light. The recoiling photofragments were detected in coincidence with a time- and position-sensitive detector. O + O_2 was observed, leading to ground state products as well as higher-lying O(^1D) channels. Three-body dissociation accounted for 3.6% of valid events at 193 nm and 19.2% at 157 nm. All product channels exhibited unexpectedly high kinetic energy release, implying high levels of excitation in the precursor ozonide anions. Analysis of Dalitz plots reveals the three-body dissociation occurs in a concerted mechanism at both wavelengths.

5. 1 Introduction

One is hard-pressed to overstate the importance of ozone in human affairs, especially compared to other trace gases.[1-4] In the stratosphere, absorption of ultraviolet radiation by ozone prevents harmful DNA damage to life forms on the surface. Less benignly, ozone contributes to photochemical smog in the troposphere. While ozone is a greenhouse gas, it is also a strong oxidizer, causing it to remove methane and other hydrocarbons from the atmosphere. Ozone also has technological uses, as an oxidizer in synthetic chemistry and as a disinfectant, and it has the environmental advantage of decomposing into molecular oxygen.

The present study focuses on the photodissociation dynamics of ozone at 193 and 157 nm, which roughly bracket a broad band stretching from about 6 to 8 eV in the gas phase absorption spectrum of ozone. This unnamed band is not as relevant for shielding Earth's inhabitants from UV radiation as the storied Hartley band (4 – 6 eV) because O_2 absorbs efficiently in this region via the Schumann-Runge system.[5-7] Nevertheless, gaps exist in the O_2 absorption around 190 nm, so absorption by ozone at these wavelengths is significant. Photoabsorption cross sections in this region have been determined experimentally, with a maximum of about 0.8 MB over a plateau.[8] Complementary electron energy loss spectra have yielded similar results.[8-10] Calculations by Schinke and coworkers[11] and Palmer and Nelson[12] have shown this band is comprised of a dominant contribution from the third $^1A_1$ state and a smaller contribution from the second $^1B_1$ state (on the red side) and a significant contribution from the fourth $^1A_1$ state (blue side).

Several photodissociation experiments have been performed at 193 nm. Turnipseed *et al.*[13] measured a quantum yield of $\varphi[O(^1D)] = 0.46 \pm 0.29$ and $\varphi[O(^3P)] = 0.57 \pm 0.14$, invoking a minor three-body channel producing $3O(^3P)$ to account for the total quantum yield greater than unity. Later laser-induced fluorescence (LIF) experiments by Takahashi *et al.*[14] and Nishida *et al.*[15] both measured $\varphi[O(^1D)] = 0.48 \pm 0.03$. Stranges *et al.*[16] performed a high-resolution photofragment translational spectroscopy experiment yielding a photofragment translational energy distribution [$P(E_T)$ distribution] featuring a dominant bimodal contribution from $O(^1D)$. Branching ratios were also determined, and further evidence for a minor $3O(^3P)$ channel was presented. Takahashi *et al.*[17] measured $\varphi[O(^1S)] = 2.5 \pm 1.1 \times 10^{-3}$. Brouard *et al.*[18] analyzed the angular momentum polarization of $O(^1D)$ fragments and concluded 193 nm dissociation resulted from excitation to two different electronic states, of either $^1A_1$ or $^1B_1$ symmetry, in agreement with high level *ab initio* calculations discussed above.[11,12]

Significantly less experimental attention has been given to photodissociation at 157 nm, as presented in this work or, indeed, at any wavelengths within the 6 - 8 eV band. Taherian and Slanger photodissociated ozone at 157 nm and measured a total quantum yield of oxygen atoms of $\varphi[O(^1D) + O(^3P)] = 1.90 \pm 0.30$, concluding from the super-unitary quantum yield that dissociation into 3O(^3P) must occur and account for about 45% of dissociation events.[19]

Here, we report results from experiments on ozone photodissociation at 193 and 157 nm, within the band between 6 and 8 eV, using fast beam photofragment translational spectroscopy. While our experiments characterize both two- and three-body dissociation channels, particular emphasis is given to the latter, given our ability to directly detect photofragments in time- and position-coincidence. Table 5.1 gives the spin-allowed fragmentation channels and dissociation energies relevant to this study. D_0(O_2-O) was taken from the O(^1D) photofragment excitation spectrum obtained by Takahashi et al.[20] Other values listed used term energies from Huber and Herzberg[21] and atomic energy levels from Moore.[22] The well depths of the diatomic photofragment for each channel are also included.

5. 2 Experimental

The fast beam photofragment translational spectrometer used in this study has been described previously in detail.[23-25] A pulsed beam of negative ions was accelerated to high laboratory-frame velocity, mass-selected, and photodetached by a laser pulse. The resulting beam of the neutrals of interest was intersected downstream with another laser pulse, resulting in photodissociation. The recoiling photofragments were detected in coincidence by a time- and position-sensitive detector. The time and position data were used to construct photofragment $P(E_T)$ distributions.

Ozone was produced by flowing 10 psi of ~10% O_2 in ~50/50 Ar/He through a commercial ozonator (Ozone Solutions) and expanding the resulting gas mix of O_3 in O_2 into a vacuum chamber through a piezocrystal valve pulsed at 60 Hz. Ozonide (O_3^-) anions were produced by one or both of the following ionization methods: applying a high voltage discharge (~1 kV) across the gas expansion or intersecting

Table 5.1 List of spin-allowed product channels. Dissociation energies and the well depth of the surviving diatomic fragment are given in eV.

Channel	Assignment	D$_0$ (eV)	Well depth (eV)
1	$O_2(X\,^3\Sigma_g^-)+O(^3P)$	1.052	5.115
2	$O_2(a^1\Delta_g)+O(^1D)$	4.00	4.118
3	$O_2(b^1\Sigma_g^+)+O(^1D)$	4.646	3.488
4	$3\,O(^1P)$	6.167	----
5	$O_2(a^1\Delta_g)+O(^1S)$	6.22	4.118
6	$O_2(b^1\Sigma_u^-)+O(^1S)$	6.87	3.488
7	$O(^1D)+2\,O(^3P)$	8.135	----

the expansion with an electron beam (~1 keV). The ions were collimated by a skimmer, accelerated to a beam energy of 9 keV, and separated by mass by a Bakker time-of-flight mass spectrometer.[26,27] The ion packet was intersected by a pulse, $h\nu_1$, from a XeCl excimer-pumped dye laser (Lambda-Physik LPX-200, Lambda-Physik FL 3002). Some of the ions were photodetached by this laser pulse and the remaining ions were deflected out of the beam path, leaving a fast beam of neutral radicals. A laser wavelength of 386 nm (3.2 eV) was used for photodetachment. The EA of ozone is 2.103 eV,[28] but photodissociation of ozonide anion competes with photodetachment for about 1 eV above the EA.[29-31] From the PES, photodetaching at this energy should impart about 0.3 eV into neutral ozone. The photon energy used was chosen with the expectation that photodetachment would be the dominant photodestruction process to occur. Nonetheless, some photodissociation signal was observed at 3.2 eV, resulting in some contamination in the beam by O and O_2.

The neutral ozone packet was intercepted one meter downstream by a pulse, $h\nu_2$, from a second excimer laser (GAM EX-50F) operating at either 193 or 157 nm (6.4 and 7.87 eV). This second pulse dissociated the neutral ozone molecules and the recoiling photofragments reached the coincidence imaging detector 2.15 m downstream while the undissociated parent beam impinged upon a 5 mm diameter beam block positioned immediately in front of the detector.

The coincidence imaging detector is based on the design by Amitay and Zajfman[32] and consists of 75 mm diameter microchannel plates (MCP)s mounted in a Z-stack configuration and coupled to a phosphor screen. The image from the phosphor screen was split by a dichroic beam splitter with the reflected image going to a 4 x 4 multianode photomultiplier tube (PMT) array and the transmitted portion proceeding to an image intensifier positioned before a charge-coupled device (CCD) camera. The arrival times of the photofragments were acquired by the PMT and correlated with position information from the CCD camera. The only events accepted were those where two or three photofragments struck within the same time window and the position information from the CCD camera matched the rough position information provided by the PMT array.

The coincident photofragment arrival time and position data were used to infer the photofragment masses and translational energy release for each dissociation event; from this information, the center-of-mass $P(E_T)$ distribution was constructed for each product channel, including two- and three-body channels. For three-body events, this information was used to construct Dalitz plots that describe the momentum partitioning of the three fragments. Due to the presence of the beam block and the finite geometry of the detector, dissociation from some orientations are more easily detected than others. We account for this by normalizing the raw two-body $P(E_T)$ distributions with a detector acceptance function (DAF). Three-body $P(E_T)$ distributions were not DAF-corrected, which is likely to bias our results in favor of high kinetic energy events.

5. 3 Results

Figure 5.1a shows the mass ratio distributions from experiments performed at a photodetachment wavelength of 386 nm and photodissociation wavelengths of 193 and 157 nm where two bodies were detected in coincidence. Two mass ratios were observed: a dominant 2:1 channel and a smaller 1:1 channel. The 2:1 signal corresponds to observation of the expected O + O_2 mass channel, while the 1:1 signal has two possible sources: three-body dissociation events may occur where the central O atom has collided with the beam block and the outer two O atoms are detected as a two-body event; the other possibility is two-body dissociation of O_2 generated by the 3.2 eV laser pulse by either anion photodissociation or dissociative photodetachment. This unusual presence of O_2 contamination in an otherwise mass-selected beam is a consequence of photodetaching ozonide far above its EA and the competition between dissociation and detachment.[29-31] Signal from the 1:1 mass ratio is observed at both 193 and 157 nm, but is far more prevalent at the higher photon energy. Figure 5.1b shows the three-body mass distributions. At both excitation energies, a single peak is observed at 16 amu, corresponding to the three O atoms detected in coincidence.

The two-body $P(E_T)$ distributions obtained from the O + O_2 product mass channel are presented in Figures 5.2a and 5.2b, for dissociation at 193 and 157 nm, respectively. Vertical dotted lines are drawn depicting the maximum translational energy release ($E_{T,max}$) expected for the product channels labeled, assuming dissociation from ozone in its electronic and vibrational ground state. These lines are drawn for reference, as the ozone is not produced in its vibrational ground state. In Figure 5.2b, events with large kinetic energies ($E_T > 5$ eV) exhibit large error bars following DAF correction, leading to sharp, intense features in this E_T range. Due to the large error, branching ratios within this mass channel are inestimable.

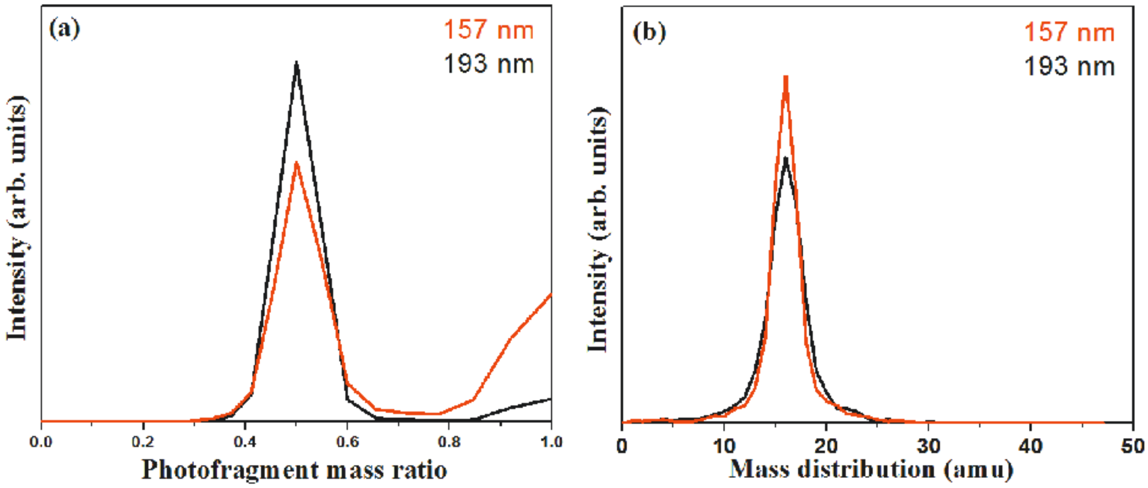

Figure 5.1 Two-body photofragment mass ratio (a) and three-body mass distribution (b) for photodissociation by 193 nm (black) and 157 nm (red).

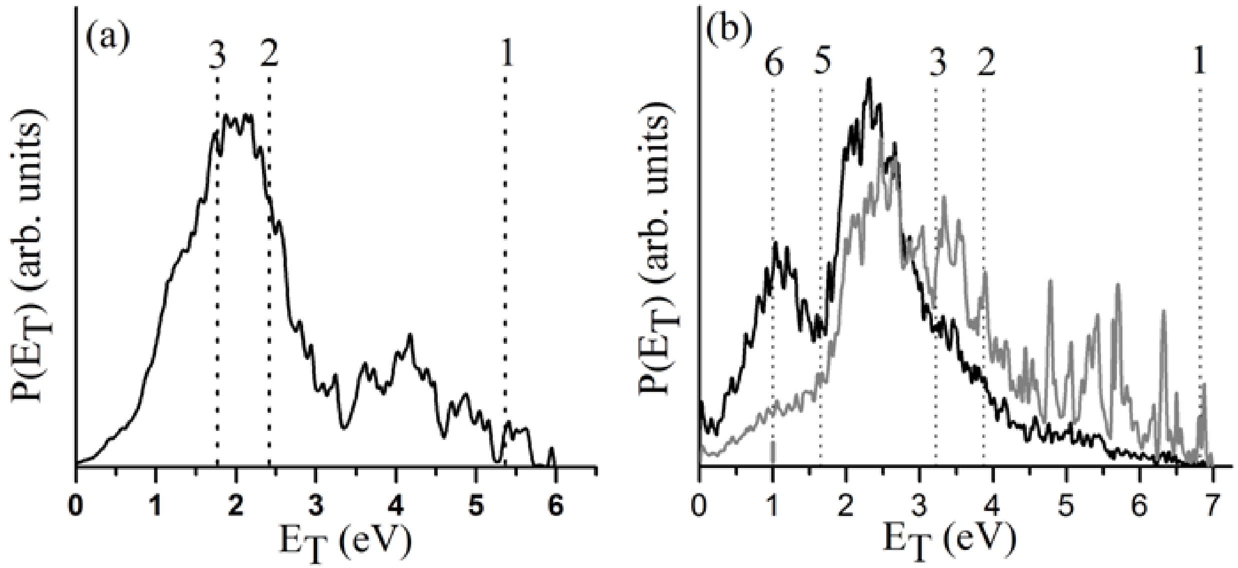

Figure 5.2 Photofragment translational energy distributions for two-body dissociation into O and O_2 at 193 nm (a) and 157 nm (b). Dotted lines mark the maximum translational energy release for product channels given.

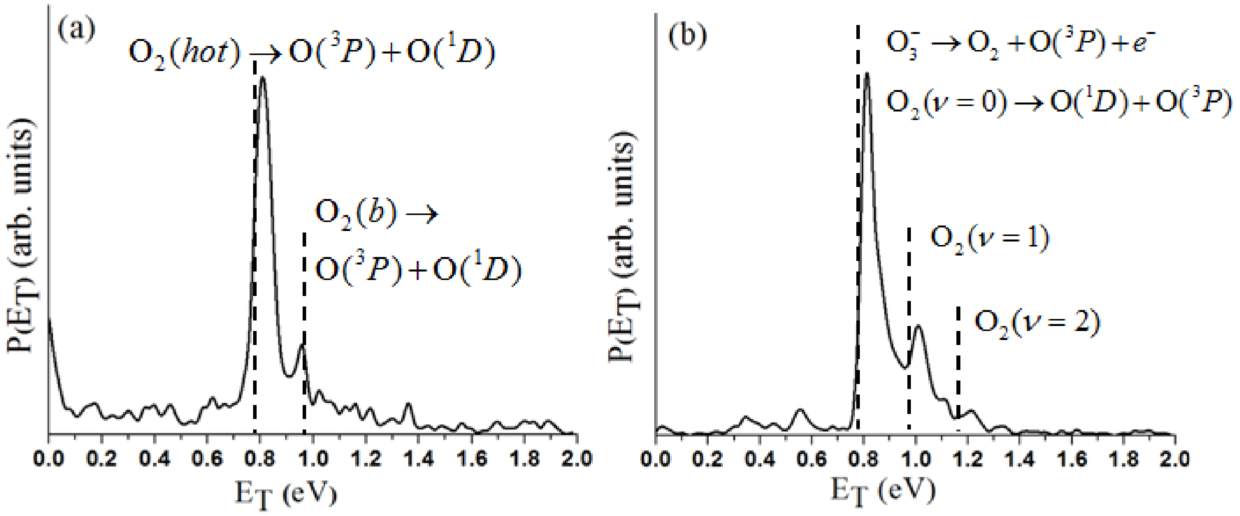

Figure 5.3 Photofragment translational energy distributions for 1:1 mass ratio, two-body dissociation corresponding to $O_2 \rightarrow O+O$ at 193 nm (a) and 157 nm (b). Suggested mechanisms are given for the observed features (see text).

The DAF-corrected *P(E_T)* distribution is shown in grey-scale in Figure 5.2b; the non-DAF-corrected *P(E_T)* distribution is shown in black, and suggests the *P(E_T)* distribution is actually unstructured in this energy range. The sharp features likely result from a small number of detected events being over-amplified by the DAF-correction. Figure 5.3 presents *P(E_T)* distributions constructed from dissociation events with a 1:1 photofragment mass ratio obtained at 193 nm (Fig. 5.3a) and 157 nm (Fig. 5.3b).

P(E_T) distributions for events where three photofragments were detected in coincidence are presented in Figures 5.4a (193 nm) and 5.4b (157 nm). To zoom in

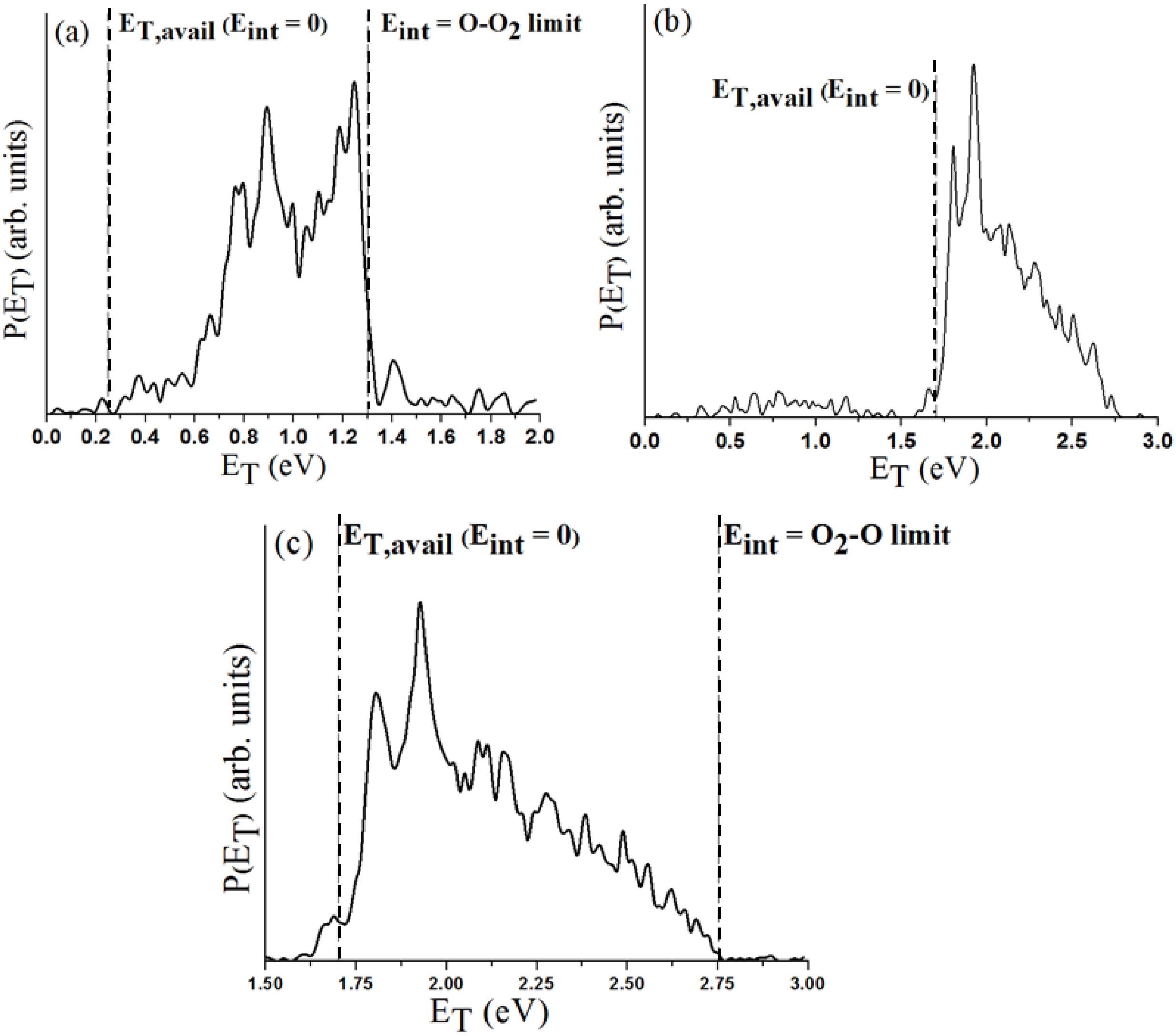

Figure 5.4 Photofragment translational energy distributions for three-body dissociation into 3O(^{3}P) at 193 nm (a) and 157 nm (b). Panel (c) presents the 157 nm from 1.5 to 3 eV. Dashed lines mark the expected translational energy release for ozone with 0 and 1.05 eV internal energy (see text).

on the main feature obtained at 157 nm, Figure 5.4c shows the *P(E_T)* distribution from 1.5 to 3.0 eV. Because ozone is a triatomic molecule, all available energy must be deposited into translation or electronic excitation. In each panel a vertical dashed line labeled "$E_{T,avail}$ (E_{int} = 0)" indicates the discrete E_T where the three-body events should fall based on the energetics given in Table 5.1. As was discussed in Section 5.2, neutral ozone molecules were prepared from the ozonide anions by photodetachment over 1 eV above the electron affinity of ozone; thus the neutrals were produced in a distribution of internal energies. A second vertical dashed line indicates the maximum possible E_T release given the bond energy of the O-O_2 bond (1.052 eV),[20] and is labeled "E_{int} = O-O_2 *limit*".

Dalitz plots[33,34] illustrating the momentum partitioning among fragments resulting from three-body dissociation are presented in Figures 5.5 and 5.6 for 193 and 157 nm, respectively. Each height in the equilateral triangle corresponds to the kinetic energy of one of the fragments, such that a valid three-body event must fall within the triangle to satisfy conservation of energy. A second constraint is that a valid event must fall within a circle inscribed in the triangle to satisfy conservation of linear momentum. On each side of the triangle an axis is drawn corresponding to the fraction of the square of the momentum, $f_i = p_i^2 / \Sigma p_j^2$, of fragment *i*. Because all three fragments detected in this experiment are the same mass and indistinguishable by our detector, the momentum partitioning exhibits six-fold symmetry. All events in Figure 5.5 are thus plotted in one sixth the area of the Dalitz circle. As plotted here, the oxygen atoms are plotted in order of decreasing kinetic energy, O > O' > O". Different panels within Figures 5.5 and 5.6 plot events corresponding to different energy ranges in the *P*(E_T) distributions.

5. 4 Analysis

In each of the *P*(E_T) distributions presented in this study, the maximum photofragment translational energies observed exceed those expected for excitation from internally cool neutral ozone. We ascribe this excess energy to photodetaching ozonide 1.1 eV above the detachment threshold and thus preparing the neutrals in a Franck-Condon distribution of vibrational states. Some evidence presented below suggests the internal energy is not due entirely to photodetachment over threshold; we thus propose that either vibrationally hot or electronically excited ozonide anions are produced in the ionization step. Due to the temperature of the ozone, we cannot make definitive assignments in the two-body *P*(E_T) distributions. In the following, we suggest product channels that are consistent with our observations.

5.4.1 Two-body dissociation

In Figure 5.2a, we present the two-body *P*(E_T) distribution obtained from 193 nm photodissociation. Two broad features peaking away from E_T = 0 are observed. The higher E_T feature begins around 3.3 eV and extends to around 5.6 eV. The entirety of this feature lies beyond the $E_{T,max}$ for channel 2, $O(^1D) + O_2(a^1\Delta_g)$, and is consistent with channel 1, $O(^3P)+O_2(X\,^3\Sigma_g^-)$. This feature extends past the $E_{T,max}$ for channel 1 by about 0.24 eV, indicating dissociation from vibrationally excited ozone. The lower E_T feature, the dominant source of signal at this photon energy, extends to about 3.3 eV, past the $E_{T,max}$ of channel 2 by about 0.88 eV, which is less than the 1.1 eV extra energy available from the photodetachment step. The bulk of the feature falls within the limits of channels 2 and 3, $O(^1D)+O_2(b^1\Sigma_g^-)$, especially if the $E_{T,max}$ of channel 3 is viewed as a lower estimate on account of the additional energy available. The broad feature is likely due to a combination of channels 2 and 3 with $O_2(a)$ and $O_2(b)$ generated in a broad distribution of vibrational states.

Figure 5.2b shows the two-body $P(E_T)$ distributions obtained at 157 nm photodissociation. This distribution can be split into three regimes: a noisy region past about 4.5 eV, a broad feature roughly within $1.6 < E_T < 4.5$ eV, and a shoulder appearing at $E_T < 1.6$ eV. The high E_T events fall within the limit of channel 1 and the majority of them fall well outside the limits of channel 2. These events are most consistent with channel 1. Likewise, most of the broad feature at mid-range E_T fall within the $E_{T,max}$ of channels 2 and 3, and these events are most likely due to those channels. While the feature is noisy, a bimodality can be observed, with one peak occurring at 2.48 eV the other around 3.34 eV. This is consistent with the population of both $O(^1D)$ pathways. The low E_T shoulder is consistent with accessing channels 2 and 3 with vibrationally excited O_2 (*a, b*) products. However, events in this E_T range are also consistent with channels 4, $O(^1S)+O_2(a^1\Delta_g)$ and 5, $O(^1S)+O_2(b^1\Sigma_g^-)$.

Figure 5.3a shows the two-body $P(E_T)$ distribution obtained at 193 nm from photofragments with a 1:1 mass ratio. Two features are evident: a narrow feature peaking at 0.80 eV and a minor feature peaking at 0.96 eV. As will be discussed in detail below, there is little evidence in either the 193 or 157 nm Dalitz plots to suggest dissociation of ozone from a linear configuration in large amounts. Recalling that charged particles are deflected from the beam path subsequent to interception by $h\nu_1$, this suggests signal from two-body, 1:1 mass ratio events comes from dissociation of O_2. It should be noted there is a 1 mm aperture between the photodetachment and photodissociation regions; therefore, any O_2 molecule proceeding to the photodissociation volume must have received nearly zero recoil from $h\nu_1$. For the dominant feature, we propose O_2 is produced by

$$O_3^- \xrightarrow{386\text{ nm}} O^-(^2P)+O_2(X\,^3\Sigma_g^-;\nu=7,J>25)\,, \tag{5.1}$$

after which it is dissociated by the second laser pulse:

$$O_2(X\,^3\Sigma_g^-;hot) \xrightarrow{193\text{ nm}} O(^3P)+O(^1D)\,, \tag{5.2}$$

where excitation by 193 nm has prompted the $B^3\Sigma_u^- \leftarrow X\,^3\Sigma_g^-$ transition, known as the Schumann-Runge continuum (SRC).[35-39] The energy available for translation following excitation by $h\nu_1$ is about 0.06 eV, consistent with high E_T discrimination by the aperture. A dotted line in Figure 5.3a indicates the E_T assuming dissociation of O_2 (v = 7, J = 25). The slighter feature peaking at 0.96 eV is consistent with the formation of O_2 in the $\mathrm{O_2}(b^3\Sigma_g^+)$ state, followed by dissociation via SRC. The second dotted line in Figure 5.3a indicates the E_T following dissociation from $\mathrm{O_2}(b)$.

While preparation of O_2 in such an internally hot state seems initially implausible, a few physical considerations corroborate this assignment. First, evidence discussed above in the analysis of the two-body $P(E_T)$ distributions of ozone suggest $\mathrm{O_3^-}$ is already vibrationally excited. Second, there is a considerable change in bond length between $\mathrm{O_3^-}$ (r_e = 1.36Å)[28] and O_2 (r_e = 1.21Å);[21] the compression of the bond should lead to the formation of the diatomic in vibrationally excited states. Finally, we expect high rotational levels to be populated in the O_2 fragment as the bent structure of $\mathrm{O_3^-}$ (θ = 111.8°)[28] is likely to impart significant torque in the dissociation.

The 157 nm $P(E_T)$ distribution in Figure 5.3b has two main features: a dominant one at 0.81 eV and a smaller one at 1.01 eV. Here we propose low E_T O_2 is produced by dissociative photodetachment of $\mathrm{O_3^-}$:

$$\mathrm{O_3^-} \xrightarrow{386\text{ nm}} \mathrm{O}(^3P) + \mathrm{O_2}(X\,^3\Sigma_g^-) + e^-, \tag{5.3}$$

followed by dissociation of the O_2 fragment

$$\mathrm{O_2}(X\,^3\Sigma_g^-; \nu = 0,1,2) \xrightarrow{157\text{ nm}} \mathrm{O}(^3P) + \mathrm{O}(^1D), \tag{5.4}$$

where O_2 is prepared in its first few vibrational quanta, indicated by dotted lines in Figure 5.3b. $E_{T,avail}$ following the first step is about 0.06 eV, most of which is expected to accrue to the departing electron, leaving the O_2 fragment with very little recoil. The $h\nu_2$ pulse once again excites ground state O_2 to the SRC.

5.4.2 Three-body dissociation

The $P(E_T)$ distribution for 193 nm photodissociation of ozone is presented in Figure 5.4a. There is little intensity in the vicinity corresponding to dissociation from ozone with $E_{int} = 0$. The $P(E_T)$ distribution peaks near the limit of E_T = 2.75 eV (corresponding to the dissociation asymptote of neutral ozone), indicating ozone is prepared with a large degree of vibrational excitation from the photodetachment step. While there appears to be bimodal structure in the $P(E_T)$ distribution, with peaks in intensity at E_T = 0.89 and 1.24 eV, there little reason to expect such structure. Furthermore, the features in the distribution do not appear to correspond to the vibrational spacing of neutral ozone, suggesting the irregularities owe more to noise than to spectroscopy. This is consistent with the small number of data assigned to this mass channel, which was roughly half the number assigned to the 1:1 mass channel.

In Figure 5.4b, the $P(E_T)$ distribution for 157 nm peaks much closer to the $E_{int} = 0$ limit, represented by the first dotted line from the left, than is the case for 193 nm. There is a broad, low intensity feature evident around 0.25 eV. We attribute this to $O(^1D) + 2O(^3P)$, which opens at an excitation energy of 8.14 eV, and is accessible in this experiment given the ~1 eV excess energy present in neutral ozone. In Figure 5.4c, focusing on the region of most intensity, the spacing of the

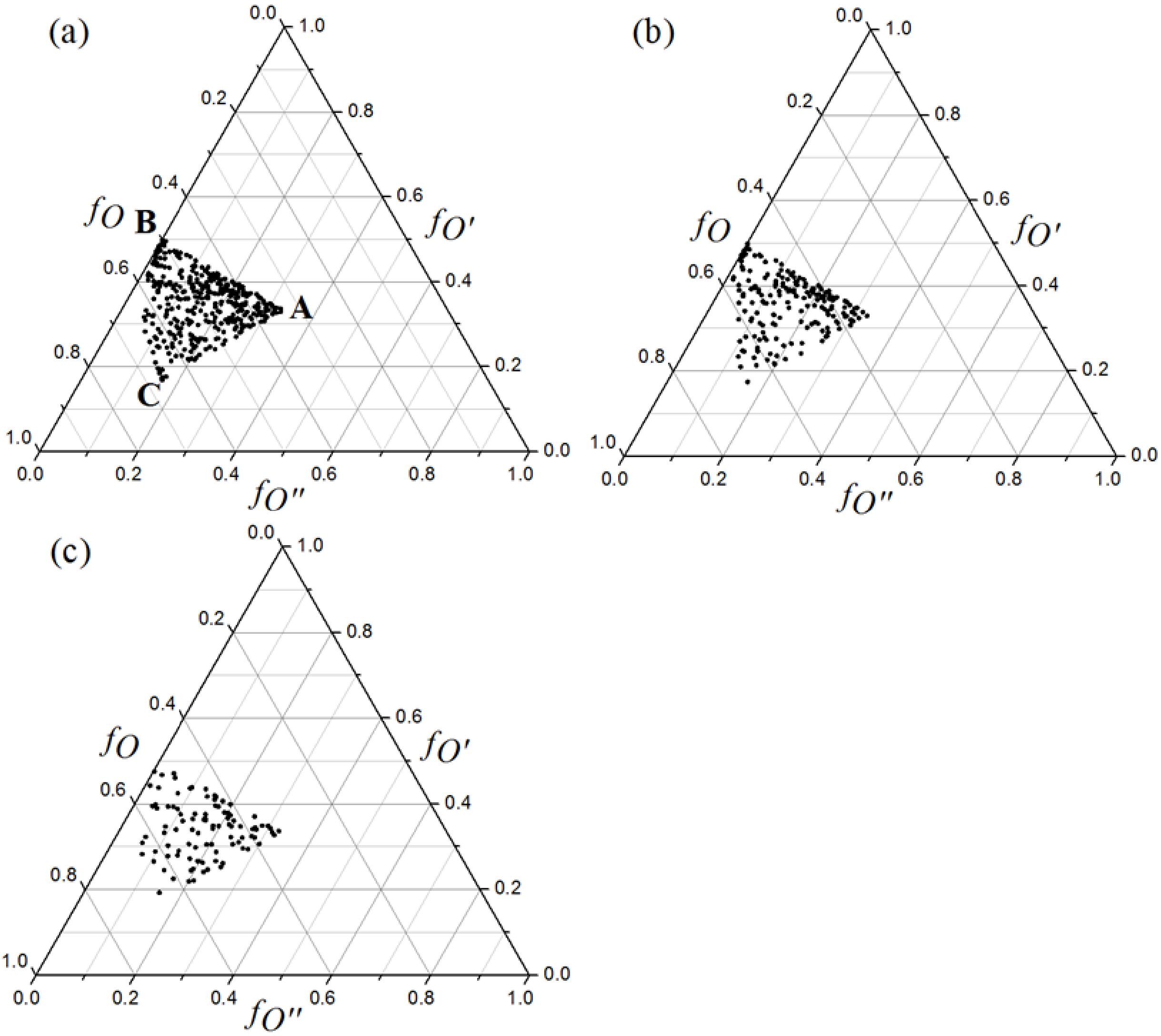

Figure 5.5 Dalitz plots for the dissociation of ozone at 193 nm. Panel (a) presents the full data set. **A**, **B**, and **C** denote limiting kinematic cases (see text). Panel (b) corresponds to $0 < E_T < 0.95$ eV. Panel (c) corresponds to $1.05 < E_T < 2$ eV.

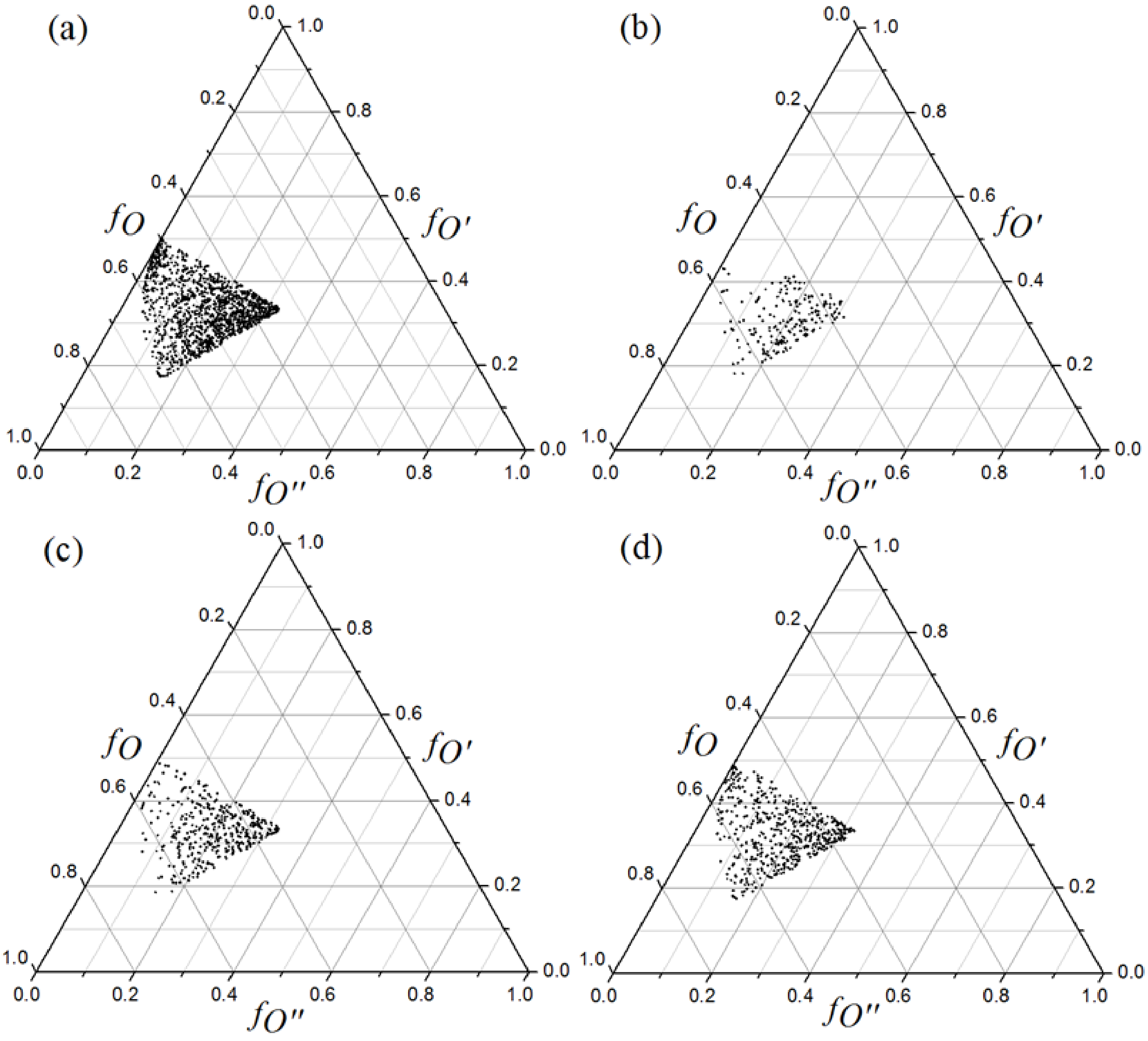

Figure 5.6 Dalitz plots for the dissociation of ozone at 157 nm. Panel (a) presents the full data set. Panels (b) - (d) correspond, respectively, to $1.74 < E_T < 1.88$ eV, $1.88 < E_T < 2.10$ eV, and $2.10 < E_T < 2.80$ eV.

first three features, about 0.12 eV, is close to the vibrational spacing of neutral ozone, 0.14 eV. The distribution extends to the O-O_2 bond energy limit, indicating ozone is dissociated from all levels of internal excitation.

The Dalitz plot corresponding to the full 193 nm $P(E_T)$ distribution (ranging from 0 to 2 eV) is shown in Figure 5.5a, with all data represented in the one sixth wedge as discussed above. Intensity is greatest in the center of the Dalitz plot, marked **A**, which corresponds to all three fragments receiving equal momentum, 120° away from each other. This is expected for three-body dissociation of ozone, which has an equilibrium bond angle of 116.7°.[40,41] Some intensity is evident in every region of the wedge of the Dalitz plot, suggesting ozone samples a variety of geometries in the excited states on which dissociation occurs. These geometries can be discussed in terms of their extremes: points along the line from **A** to **B** represent symmetric dissociation from progressively more linear configurations, with points at **B** corresponding to linear dissociation with the middle O atom receiving no recoil; points along the arc from **B** to **C** represent progressively asymmetric dissociation from a linear geometry, with **C** corresponding to one O atom receiving the maximum of 2/3 the total E_T released and the other two atoms splitting the remainder evenly; points along the line from **C** to **A** represent dissociation events of increasing symmetry and decreasing linearity.

In Figures 5.5b and 5.5c, Dalitz plots are presented, respectively, for $0 < E_T < 0.95$ eV and $1.05 < E_T < 2$ eV. This is in order to determine if the bimodality in the $P(E_T)$ distribution in Figure 5.5a is apparent in the three-body kinematics. While the data are sparse, there appears to be greater density in Figure 5.5b in the region between points **A** and **B**, consistent with dissociation along the symmetric stretch coordinate, under some influence from bending excitation. The difference between the two Dalitz plots is likely a straightforward consequence of photoexcitation from a hotter ground state molecule in the case of Figure 5.5c, where different levels of vibrational excitation in the ground electronic state lead to different geometries in the electronic excited states responsible for dissociation.

Figure 5.6a shows the Dalitz plot for the 157 nm $P(E_T)$ distribution between 1.5 and 3 eV. As in the case of 193 nm discussed above, the region of most intensity is the center of the Dalitz plot, indicating concerted, symmetric dissociation from a geometry similar to that of ground state ozone. The Dalitz plots are split by total E_T into three sections in Figures 5.6b-d, with 5.6b and 5.6c corresponding to the first two peaks in the $P(E_T)$ distribution, respectively, and 5.6d corresponding to the high E_T tail stretching to $E_T = 2.75$ eV. Each plot has significant intensity in the central region, similar to Figure 5.6a. As the total E_T increases, from 5.6b to 5.6d, the Dalitz plots extend further to the perimeter of the Dalitz circle, indicating dissociation influenced by bending and asymmetric stretches. In each case, there is more relative intensity along the **A-C** line than was observed in Figure 5.5, suggesting the asymmetric stretch is more active in the photodissociation at 157 nm.

5.4.3 Branching fractions

The branching fractions for the two- and three-body dissociation channels for the two photon energies employed are presented in Table 5.2. Because three-body events are detected with less efficiency than two-body events in our detection scheme, the fraction of three-body events we quote represents a lower bound on the true value. On the other hand, the large errors observed at high E_T in the 157 nm two-body $P(E_T)$ distribution suggest the O + O_2 ground state channel also suffers from lower detection efficiency. Note the values listed in Table 5.2 do not include any contribution from the 1:1 mass channel (constituting about 9% of events detected at 193 nm and 19% at 157 nm), as we have assigned these events to dissociation from O_2 contaminant produced in the photodetachment step.

5. 5 Discussion

5.5.1 Comparison with previous experiments

The *P(E$_T$)* distribution for 193 nm photodissociation presented in Figure 5.2a is at considerable variance with the work of Stranges *et al.*[16] Their *P(E$_T$)* distribution, obtained by high resolution photofragment translational spectroscopy, indicated $<E_T>$ = 3.08 eV for dissociation into $\mathrm{O}(^3P)+\mathrm{O}_2(X\,^3\Sigma_g^-)$, over 1 eV less kinetic energy release than our value, $<E_T>$ = 4.22 ± 0.02 eV. Likewise, their $<E_T>$ for channel 2, 1.52 eV, was less than our value of 1.95 ± 0.02 eV. As another comparison, their features assigned to channels 1 and 2 fall well short of $E_{T,max}$, by about 0.51 and 0.34 eV, respectively. In contrast, our two features assigned to channels 1 and 2 exceed the expected $E_{T,max}$, by about 0.33 and 0.94 eV, respectively. Differences in this direction are expected, given the much cooler ozone produced in the Stranges study.

Turning to three-body dissociation, we observe a branching fraction of 0.036 for the $3\mathrm{O}(^3P)$ channel, in slight disagreement with the 0.020 ± 0.002 determined by Stranges *et al*,[16] though our low three-body signal at 193 nm prevents a confident estimate of the branching fraction. The synchronous concerted dissociation along the symmetric stretch coordinate inferred from the Dalitz plot analysis in Section 5.5B agrees well with the assignment given by Stranges by forward convolution fit of time-of-flight distributions.

At 157 nm, signal-to-noise in our *P(E$_T$)* distribution beyond about 5.5 eV was too low to facilitate a meaningful estimation of $<E_T>$. This could be due to inefficient detection of the fast O fragments in channel 1. Fortunately, the dominant feature diminishes around 4.7 eV. $<E_T>$ for this feature was determined to be 2.73 ± 0.02 eV. We assign this feature to a combination of channels 2 and 3 because of our inability to resolve the two channels. Thus, it is unclear how well our results compare with those of Taherian and Slanger,[19] who concluded the only source of

Table 5.2 Branching fractions between two- and three-body channels. Values from the literature are also given.

λ_{diss}	Two-body	Three-body	Three-body (other studies)
193 nm	0.964	0.036	0.02 (Ref. 16)
157 nm	0.808	0.192	0.45 (Ref. 19)

$O(^1D)$ at this wavelength is channel 3. Our $<E_T>$ peaks significantly away from $E_{T,max}$, indicating vibrationally excited $O_2(b)$ fragments. While Taherian reported vibrational excitation in the $O_2(b)$ fragment up to v = 6, the most populated vibrational levels were v = 1 and 2, less than our observations suggest.

Our branching fraction of 0.192 is less than half that of Taherian's reported value of 0.45. This disagreement is in the opposite direction of our disagreement with Stranges, where our estimate suffers from poor statistics. The Dalitz plots associated with low E_T events (and thus most directly comparable to the cooler ozone in Taherian's experiment)[19] presented in Figure 5.6 (b and c) have significant intensity in the region between points **A** and **C**, indicating asymmetry in the three-body dissociation geometry, with one O atom departing with more momentum than the other two atoms. This is consistent with a concerted, asynchronous decay mechanism similar to the one assumed by Taherian and Slanger.[19] A final point worth addressing is the implication of the hot state of ozone in these experiments for our branching fraction. We expect the presence of additional internal energy in ozone to lead to more three-body dissociation. While our three-body branching fraction represents a lower bound (Section 5.4.C), the high temperature of ozone in our experiment sharpens the contrast of our 19% branching fraction to the 45% value determined by Taherian and Slanger.[19]

5.5.2 Ozonide synthesis

The variance in the $P(E_T)$ distributions observed in this study and that of Stranges *et al.*[16] is due to a large difference in internal temperature in neutral ozone. Two effects are at work here; (1) additional energy is present due to photodetaching above the EA, and (2) evidence from our three-body $P(E_T)$ distributions indicates additional energy is present in the anion precursor. Because of the latter effect, it is worthwhile to compare our synthesis procedure to others discussed in the literature. In addition to the ozone preparation discussed in section 5.2, we varied gas mixes and ionization methods. O_2 concentrations were varied between 1 - 100% and the noble gases used were Ar, He, Ne, 50/50 Ar/He, and 50/50 Ne/He. No dependence of kinetic energy release on the gas mix was observed in either two- or three-body $P(E_T)$ distributions. The stagnation pressure prior to expansion into the vacuum chamber was always kept below 14 psi to avoid damaging the ozonator. Nor was any dependence on the two ionization methods observed. In contrast, Stranges *et al.*[16] used a commercial ozonator and stored ozone on silica gel at -74 °C and later obtained a mixture of 4% ozone in He by warming the silica gel. It is important to note that Stranges *et al.*[16] photodissociated neutral ozone directly, without a prior photodetachment step from the anion as in this work.

Discovery of unexpected surpluses of energy is common in the ozonide experimental literature. Arnold *et al.*[28] produced ozonide by intersecting an electron beam with a pure O_2 gas expansion. The resulting photoelectron spectra were congested by hot bands resulting from excitations of the v_3 asymmetric stretch.

More efficient cooling was achieved by passing a He/Ne mixture (10/90) over ozone adsorbed onto silica gel at -78 °C; this method was used in the published spectrum. On the other hand, in photodissociation experiments on ozonide performed by Garner *et al*,[42] a similar procedure of expanding neat O_2 across an electron beam led to cooler ions, while flowing a noble gas mix over cold, ozonated silica led to hotter ions, as evidenced by 0.35 eV of additional kinetic energy in the $P(E_T)$ distribution. In an earlier photodissociation study, Hiller and Vestal[29] produced ozonide by electron bombardment in a pure O_2 environment and concluded $D_0(\text{O-O}_2) < 1.39$ eV, over 0.3 eV less than the value of 1.69 eV obtained from the well-characterized O_3 bond energy[20] and the electron affinities of O_3[28] and O,[43] once again suggestive of high energy ozonide.

Cui and Morokuma[44] performed high level *ab initio* calculations on the lowest several electronic states of ozonide and rationalized the experimental work by suggesting that the $\text{O}_3^-(^2B_2)$ excited state is formed in the ionization sources. This state lies about 1.4 eV above the ground state, $\text{O}_3^-(^2B_1)$, but the curves cross near $\theta = 90°$, below which $\text{O}_3^-(^2B_2)$ is the lowest energy state. Returning to the present work, the possible population of the $^2B_2$ state may provide a rationale for the extensive internal excitation implied by our $P(E_T)$ distributions. Photodetachment from $\text{O}_3^-(^2B_2)$ in its equilibrium geometry ($\theta = 90°$) at hv = 3.2 eV should produce O_3 neutrals with $E_{int} = 2.5$ eV. In the ground electronic state of neutral ozone, $\theta = 90°$ corresponds to just over 2 eV of internal energy.[11] Thus, if $\text{O}_3^-(^2B_2)$ is produced in the ionization source, we expect photodetachment to produce neutral ozone with excitation in the bending mode.

In order to determine how much of the excitation of neutral ozone can be attributed to above-threshold photodetachment of ozonide versus production of excited ozonide in the ionization source, an experiment was performed with $hv_1 = 2.70$ eV (460 nm). At this wavelength, photodetachment from cold ozonide could result in up to 0.60 eV of internal energy in neutral ozone and $E_{T,avail} = 2.3$ eV for channel 4 following 157 nm photodissociation. The three-body $P(E_T)$ distribution resulting from this experiment is shown in Figure 5.7 in black. For comparison, the distribution obtained from 386 nm photodetachment is overlaid in blue. Photodetachment was less efficient at 460 nm and resulted in a noisier $P(E_T)$ distribution. However, it is evident that at 460 nm, the $P(E_T)$ distribution extends all the way to the O-O_2 limit of $E_T = 2.75$, the same as the 386 nm experiment. The energy balance in these experiments is given by

$$E_T = E_{\text{int}}^{\text{O}_3} + h\nu_2 - D_0^{\text{O-O}_2} - D_0^{\text{O-O}} - E_{\text{int}}^{\text{O}}, \qquad (5.5)$$

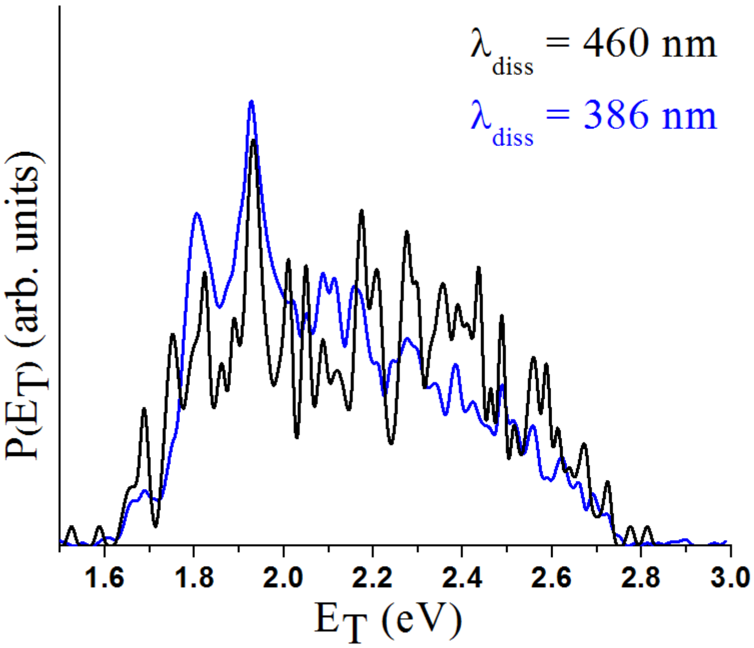

Figure 5.7 Comparison of 157 nm *P(E$_T$)* distributions following photodetachment by 460 nm (black) and 386 nm (blue).

where $E_{\mathrm{int}}^{\mathrm{O_3}}$ is the internal energy of neutral ozone, $D_0^{\mathrm{O\text{-}O_2}}$ and $D_0^{\mathrm{O\text{-}O}}$ are the bond dissociation energies of ozone and molecular oxygen, respectively, and $E_{\mathrm{int}}^{\mathrm{O}}$ is the internal energy of the O atom products and is equal to zero. $E_{\mathrm{int}}^{\mathrm{O_3}}$ is determined by

$$E_{\mathrm{int}}^{\mathrm{O_3}} = E_{\mathrm{int}}^{-} + h\nu_1 - EA - EKE\,, \tag{5.6}$$

where E_{int}^{-} is the internal energy of ozonide anion and *EKE* is the kinetic energy of the detached electron. At the limit of *EKE* = 0, the maximum available energy for translation at 157 nm is 2.81 eV following detachment by 386 nm and 2.29 eV following detachment by 460 nm. The observed maximum *E$_T$* of 2.75 implies $E_{\mathrm{int}}^{-} \geq$ 0.46 eV. Production of $\mathrm{O_3^-}(^2B_1)$ in the ionization source means we should see detachment well below the EA. At the time of writing these preliminary results, this experiment has not been performed, but observation of photodetachment well below the EA would constitute further evidence for electronically excited ozonide.

Combining equations 5.5 and 5.6, one obtains

$$E_T = E_{\mathrm{int}}^{-} + h\nu_1 + h\nu_2 - EA - D_0^{\mathrm{O\text{-}O_2}} - D_0^{\mathrm{O\text{-}O}} - EKE\,. \tag{5.7}$$

Since the photon energies and dissociation energies are constants, Eqn. 5.7 has the form of the photoelectron spectroscopy (PES) energy balance shifted by those constants. The *P(E$_T$)* distribution should therefore resemble the PES spectrum. It should be noted that some differences are expected, given the large internal energy of our ions. In Figure 5.8, we overlay the 157 nm $P(E_T)$ distribution (in red) with the PES spectrum simulation from the work of Arnold *et al.* (in black).[28] The sharp peak in the PES spectrum at the $E_{int} = 0$ dotted line corresponds to the 0-0 transition, and the three other tallest other features in the spectrum correspond to the symmetric stretch progression. Our $P(E_T)$ distribution more closely matches the less intense progression between the taller features. This corresponds to the symmetric stretch progression with one quantum in the bending mode, $v_2 = 1$. This suggests neutral ozone in our beam is vibrationally excited in both the symmetric and bending stretches. Evidence given above in section 5.4.B (Fig. 5.6d) suggests the high E_T fraction also have an excited asymmetric stretch, which was not observed in the PES spectrum of Arnold *et al.*[28] The activity of the bending mode evident in our experiment is consistent with the presence of $O_3^-(^2B_2)$ in our ionization source, as argued above.

5.5.3 157 nm three-body dissociation

The primary motivation of this study was to analyze the kinematics of three-body ozone photodissociation at 157 nm, which has only been inferred previously by fluorescence detection of O(^3P) atoms in a cell. This channel was directly observed by photofragment imaging. Dalitz plot analysis reveals a concerted dissociation mechanism. At all E_T, dissociation is most likely to occur at an angle less than 180°,

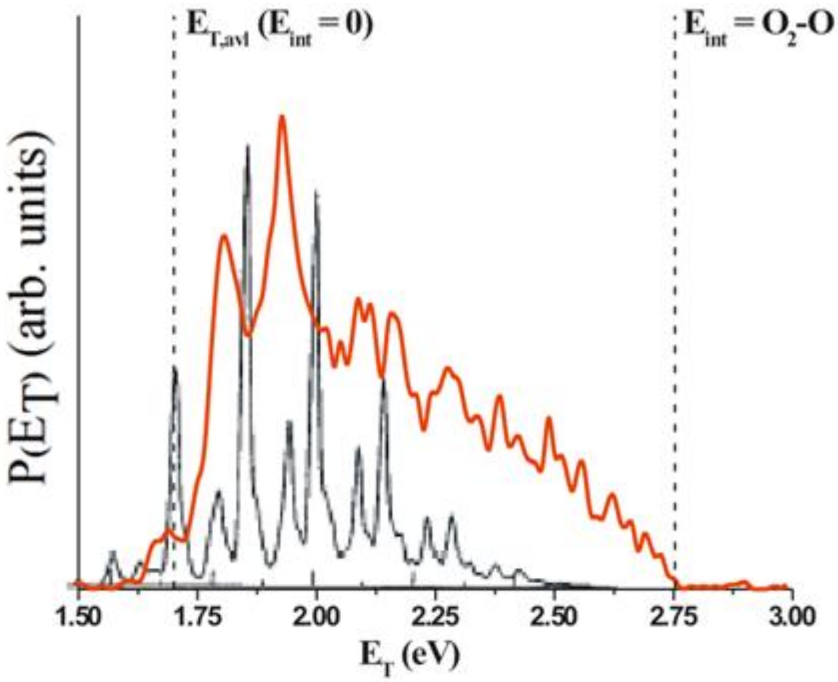

Figure 5.8 Comparison of the 157 nm $P(E_T)$ distribution (red) with the ozonide photoelectron spectrum simulation from Ref. 28.

though at higher E_T some events correspond to dissociation from a linear or nearly linear configuration. These events may result from higher excitation of the bending mode, where the bonds are more likely to cleave at a more obtuse bond angle. It is worth comparing the present results to the dynamics observed after dissociative recombination (DR) of the ozone cation at 0 eV collision energy.[45,46] In the DR study, Dalitz plots revealed a strong preference for synchronous concerted dissociation from a linear geometry for the 3O(^3P) channel. Different dynamics are not unexpected for DR, however, as the available energy for this process is 6.27 eV (much greater than the ~2 eV available here), and different electronic states are likely involved.

Three-body dissociation at 157 nm differs from that at 193 nm. In the latter, dissociation is more likely to occur at symmetric geometries. It is unsurprising that the three-body kinematics differs between the two wavelengths, as 193 nm photolysis involves excitation of the 5^1A_1 and 4^1B_1 states, while 157 nm involves the 5^1A_1, 6^1A_1, and 8^1B_2 states, according to calculations by Schinke *et al.*[11] Although it should be noted our experiments involve excitation potentially far from the Franck-Condon point, possibly altering the transition dipole moments significantly. It is somewhat surprising that the three-body $P(E_T)$ distributions are qualitatively different. For excited state dissociation, one would expect the $P(E_T)$ distributions to appear identical apart from the shift in photon energy. A possible explanation for this may be that the different excited states responsible for dissociation at different photon energies have greatest Franck-Condon overlap at different vibrational energies in the electronic ground state.

Conclusions

We have studied the two- and three-body dynamics of ozone at 193 and 157 nm using fast beam photofragment translational spectroscopy. The anions were photodetached over 1 eV above threshold at 386 nm in order to maximize detachment efficiency. They were photodissociated at 193 and 157 nm and photofragments from both two- and three-body events were detected and analyzed using a time- and position-coincidence imaging detector. These data were used to construct $P(E_T)$ distributions and, for three-body events, Dalitz plots. This study represents the first direct observation of three-body dissociation of ozone at 157 nm.

Two-body $P(E_T)$ distributions at both wavelengths suggests the dominant two-body process produces O(^1D), though we could not distinguish between the $O_2(a)$ and $O_2(b)$ channels. Three-body dissociation was observed at both wavelengths, constituting 3.6% and 19.2% of events at 193 and 157 nm, respectively. Analysis of Dalitz plots reveals the three-body dissociation occurs by a concerted mechanism, usually from a roughly equilateral geometry. Three-body dissociation at 157 nm involves excitation of the asymmetric stretch, and some fraction of high E_T events dissociate from a symmetric, linear geometry.

At both dissociation energies, $P(E_T)$ distributions extended to higher kinetic energies than expected for cold ozone, and at least 0.46 eV of internal energy is present in the ozonide anion produced in our ionization source. This presents several questions and opportunities for future experiments. Careful preparation of cold ozonide, either by silica gel adsorption or noble gas atom tagging, is paramount for determining the dissociation dynamics of non-excited ozone. A simple photoelectron spectroscopy experiment around the detachment energy (~0.7 eV) of $O_3^-({}^2B_1)$ could confirm the presence of that species in the ion beam. Finally, a purposeful experimental investigation of the electronic excited states and the dissociation dynamics of ozonide, extending the work of Garner *et al.*,[42] is long overdue.

References

[1] H. S. Johnston, Annu. Rev. Phys. Chem. **43**, 1 (1992).

[2] N. J. Mason and S. K. Pathak, Contemp. Phys. **38**, 289 (1997).

[3] S. Solomon, Rev. Geophys. **37**, 275 (1999).

[4] J. I. Steinfeld, S. M. Adlergolden, and J. W. Gallagher, J. Phys. Chem. Ref. Data **16**, 911 (1987).

[5] B. R. Lewis, S. T. Gibson, and P. M. Dooley, J. Chem. Phys. **100**, 7012 (1994).

[6] B. R. Lewis, S. T. Gibson, F. T. Hawes, and L. W. Torop, Phys. Chem. Earth, Part C, Sol. Terr. Planet Sci. **26**, 519 (2001).

[7] K. Yoshino, D. E. Freeman, and W. H. Parkinson, J. Phys. Chem. Ref. Data **13**, 207 (1984).

[8] N. J. Mason, J. M. Gingell, J. A. Davies, H. Zhao, I. C. Walker, and M. R. F. Siggel, J. Phys. B-At. Mol. Opt. Phys. **29**, 3075 (1996).

[9] M. Allan, K. R. Asmis, D. B. Popovic, M. Stepanovic, N. J. Mason, and J. A. Davies, J. Phys. B-At. Mol. Opt. Phys. **29**, 4727 (1996).

[10] M. Allan, N. J. Mason, and J. A. Davies, J. Chem. Phys. **105**, 5665 (1996).

[11] R. Schinke and S. Y. Grebenshchikov, Chem. Phys. **347**, 279 (2008).

[12] M. H. Palmer and A. D. Nelson, Mol. Phys. **100**, 3601 (2002).

[13] A. A. Turnipseed, G. L. Vaghjiani, T. Gierczak, J. E. Thompson, and A. R. Ravishankara, J. Chem. Phys. **95**, 3244 (1991).

[14] K. Takahashi, N. Taniguchi, Y. Matsumi, and M. Kawasaki, Chem. Phys. **231**, 171 (1998).

[15] S. Nishida, F. Taketani, K. Takahashi, and Y. Matsumi, J. Phys. Chem. A **108**, 2710 (2004).

[16] D. Stranges, X. M. Yang, J. D. Chesko, and A. G. Suits, J. Chem. Phys. **102**, 6067 (1995).

[17] K. Takahashi, T. Nakayama, and Y. Matsumi, J. Phys. Chem. A **107**, 9368 (2003).

[18] M. Brouard, R. Cireasa, A. P. Clark, G. C. Groenenboom, G. Hancock, S. J. Horrocks, F. Quadrini, G. A. D. Ritchie, and C. Vallance, J. Chem. Phys. **125**, (2006).

[19] M. R. Taherian and T. G. Slanger, J. Chem. Phys. **83**, 6246 (1985).

[20] K. Takahashi, M. Kishigami, N. Taniguchi, Y. Matsumi, and M. Kawasaki, J. Chem. Phys. **106**, 6390 (1997).

[21] K. P. a. H. Huber, G., *Molecular Spectra and Molecular Structure, IV. Constants of Diatomic Molecules*. (Van Nostrand, Reinhold, New York, 1979).

[22] C. E. Moore, *Atomic Energy Levels*. (1971).

[23] R. E. Continetti, D. R. Cyr, R. B. Metz, and D. M. Neumark, Chem. Phys. Lett. **182**, 406 (1991).

[24] A. A. Hoops, J. R. Gascooke, A. E. Faulhaber, K. E. Kautzman, and D. M. Neumark, Chem. Phys. Lett. **374**, 235 (2003).

[25] A. A. Hoops, J. R. Gascooke, K. E. Kautzman, A. E. Faulhaber, and D. M. Neumark, J. Chem. Phys. **120**, 8494 (2004).

[26] J. M. B. Bakker, J. Phys. E **6**, 785 (1973).

[27] J. M. B. Bakker, J. Phys. E **7**, 364 (1974).
[28] D. W. Arnold, C. S. Xu, E. H. Kim, and D. M. Neumark, J. Chem. Phys. **101**, 912 (1994).
[29] J. F. Hiller and M. L. Vestal, J. Chem. Phys. **74**, 6096 (1981).
[30] S. E. Novick, P. C. Engelking, P. L. Jones, J. H. Futrell, and W. C. Lineberger, J. Chem. Phys. **70**, 2652 (1979).
[31] J. R. Peterson, J. Geophys. Res-Space Phys. **81**, 1433 (1976).
[32] Z. Amitay and D. Zajfman, Rev. Sci. Instrum. **68**, (1997).
[33] D. Babikov, E. A. Gislason, M. Sizun, F. Aguillon, V. Sidis, M. Barat, J. C. Brenot, J. A. Fayeton, and Y. J. Picard, J. Chem. Phys. **116**, 4871 (2002).
[34] R. H. Dalitz, Philos. Mag. **44**, 1068 (1953).
[35] N. Balakrishnan, M. J. Jamieson, A. Dalgarno, Y. Li, and R. J. Buenker, J. Chem. Phys. **112**, 1255 (2000).
[36] A. Eppink, D. H. Parker, M. H. M. Janssen, B. Buijsse, and W. J. van der Zande, J. Chem. Phys. **108**, 1305 (1998).
[37] Y. L. Huang and R. J. Gordon, J. Chem. Phys. **94**, 2640 (1991).
[38] Y. Matsumi and M. Kawasaki, J. Chem. Phys. **93**, 2481 (1990).
[39] S. M. Wu, D. Chestakov, G. C. Groenenboom, W. J. van der Zande, D. H. Parker, G. R. Wu, X. M. Yang, and C. Vallance, Mol. Phys. **108**, 1145 (2010).
[40] R. H. Hughes, J. Chem. Phys. **24**, 131 (1956).
[41] T. Tanaka and Y. Morino, J. Mol. Spectrosc. **33**, 538 (1970).
[42] M. C. Garner, C. R. Sherwood, K. A. Hanold, and R. E. Continetti, Chem. Phys. Lett. **248**, 20 (1996).
[43] D. M. Neumark, K. R. Lykke, T. Andersen, and W. C. Lineberger, Phys. Rev. A **32**, 1890 (1985).
[44] Q. Cui and K. Morokuma, J. Chem. Phys. **108**, 7684 (1998).
[45] V. Zhaunerchyk, W. D. Geppert, M. Larsson, R. D. Thomas, E. Bahati, M. E. Bannister, M. R. Fogle, C. R. Vane, and F. Osterdahl, Phys. Rev. Lett. **98**, (2007).
[46] V. Zhaunerchyk, W. D. Geppert, F. Osterdahl, M. Larsson, R. D. Thomas, E. Bahati, M. E. Bannister, M. R. Fogle, and C. R. Vane, Phys. Rev. A **77**, (2008).